High Harmonic Generation for the XUV seeding experiment at FLASH

Dissertation
zur Erlangung des Doktorgrades
des Fachbereichs Physik
der Universität Hamburg

vorgelegt von

MANUEL MITTENZWEY

Hamburg
2011

Gutachter der Dissertation:	Prof. Dr. Markus Drescher Prof. Dr. Florian Grüner
Gutachter der Disputation :	Prof. Dr. Markus Drescher Dr. Jens Osterhoff
Datum der Disputatuion:	18.11.2011
Vorsitzender des Prüfungsausschusses:	Prof. Dr. Caren Hagner
Vorsitzender des Promotionsausschusses:	Prof. Dr. Peter Hauschildt

Abstract

The Free electron LASer in Hamburg (FLASH), operating in the Self-Amplified Spontaneous Emission (SASE) mode, is currently the most intense femtosecond light source in the eXtreme-UltraViolet (XUV) regime. However, the statistical nature of SASE leads to intensity fluctuations of the Free Electron Laser (FEL) pulses. Moreover, the electron acceleration process introduces arrival-time fluctuations of the electron bunch at the undulator entrance, which leads to a temporal jitter with respect to the synchronization system. This jitter limits the resolution of corresponding pump-probe experiments. In order to reduce these pulse-to-pulse fluctuations, a seeding section for the electron bunch has been installed in 2009/2010. Here, XUV seed pulses from a High-Harmonic Generation (HHG) source are overlapped in space and time with the electron bunches in new variable-gap undulators installed upstream the existing SASE undulator. Behind the undulator section, the seeded FEL radiation will be deflected by a mirror into an experimental container for beam characterization. A fraction of the optical laser, used as the driving laser for HHG, is also transported into the experimental container, thus, temporal diagnostics like cross-correlations between the synchronized seeded FEL and optical pulses are possible. Emphasis of this work is the construction and characterization of the HHG source.

Referat

Der Freie-Elektronen LASer in Hamburg (FLASH) arbeit zur Zeit in einem Modus, der die spontane Undulatorstrahlung selbst verstärkt (SASE). Die resultierende Strahlung liegt im extrem ultra-violetten (XUV) Spektralbereich und ist die stärkste Lichtquelle in diesem Wellenlängenbereich überhaupt. Das Verstärkungsprinzip SASE ist eine Methode, die das Anfangsrauschen verstärkt und dadurch intrinsisch statistischen Fluktuationen in der Intensität und im Spektrum unterliegt. Zusätzlich werden durch den Beschleunigungsprozess der Elektronen Ankunftzeitfluktuationen relativ zu einem Synchronisationslaser am Undulatoreingang eingeführt, die sich durch Ankunftzeitfluktuationen der resultierenden Lichtpulse bemerkbar machen. Diese Schuss zu Schuss Fluktuationen reduzieren die zeitliche Auflösung von so genannten Pump-Probe Experimenten. Um diese Fluktuationen zu reduzieren, wurde 2009/2010 eine seeding-Sektion in FLASH (sFLASH) implemeniert. Hierbei werden Lichtpulse einer Hohe-Harmonischen Quelle (HHG) in Raum und Zeit mit den Elektronenpaketen überlagert und anschließend in den sFLASH Undulatoren verstärkt. Nach der Undulatorstrecke wird die verstärkte Strahlung aus dem FLASH-Tunnel in einen Experimentiercontainer reflektiert. Zusätzlich wird ein Teil des für die HHG Quelle benötigten Fundamentallasers direkt in den Experimentiercontainer geführt, so dass zeitaufgelöste Kreuzkorrelationsexperimente mit dem Fundamental- und der verstärkten XUV- Laserstrahlung durchgeführt werden können. Schwerpunkt dieser Arbeit ist der Aufbau und die Charakterisierung der HHG Quelle.

Selbstständigkeitserklärung

Diese Arbeit ist von mir selbstständig verfasst worden und ich habe keine anderen als die angegebenen Quellen und Hilfsmittel verwendet.

Manuel Mittenzwey, September 2011

Contents

List of Figures

List of Tables

Introduction

1

The free-electron laser in Hamburg (FLASH) is a user facility providing highly brilliant ultrashort eXtreme UltraViolet (XUV) radiation to users. The established operating mode SASE (Self-Amplified Spontaneous Emission) shows shot-to-shot fluctuations in the spectrum, the pulse profile, and the arrival time of the radiation. In contrast, high harmonic radiation is comparably stable, but with pulse energies orders of magnitude lower than SASE. Seeding FLASH (sFLASH) with a high harmonic of an external laser is a method to combine the advantages of high harmonic generation (HHG) and FELs in order to improve the performance of the facility. In a first stage of sFLASH, the 21^{st} harmonic of a titanium-sapphire (Ti:Sa) laser is used for seeding. Between 2009 and 2010 the user operation of FLASH was stopped to implement the new 50 m long sFLASH section. Here, the electron bunches are overlapped with the XUV high harmonic radiation in order to initiate the amplification process. The amplified radiation enables then the possibility for time-dependent experiments without the lack of erratic fluctuations in the time and spectral domain and without arrival time fluctuations between the XUV radiation and the external laser. This chapter introduces the main features of HHG and the common Free-Electron Laser (FEL) operation mode SASE. It further describes the idea how to combine the advantages of each technique. Finally, the structure of this thesis is presented.

1.1 High harmonic generation

HHG is a method to generate XUV and x-ray radiation. Therefore, a femtosecond laser pulse is focused into a noble gas target. The corresponding laser field bends the atomic potential of the noble gas atoms. This deformation leads to an increased possibility of the valence electrons to tunnel through the atomic barrier. The subsequent motion is then determined by the laser field. The electrons are accelerated by the laser field and have a small possibility to recombine with their parent ion. The gained energy is then emitted in terms of XUV or x-ray photons [Winterfeldt et al., 2008; Chang and Corkum, 2010].

HHG is a coherent process where a fraction of the driving laser is converted into odd multiples of the fundamental frequency. The conversion efficiency (CE) of this process limits the pulse energy of the harmonics to the nanojoule or sub-mircojoule regime. In the time domain the high harmonic radiation consists of a burst of attosecond pulses [Papadogiannis et al., 1999; Drescher et al., 2001; Hentschel et al., 2001; Agostini, 2004] and enables real-time observation of atomic-scale electron dynamics [Drescher et al., 2002; Corkum and Krausz, 2007]. The driving laser and the XUV radiation are synchronized intrinsically. Thus, the temporal resolution of pump-probe experiments with these pulses is only

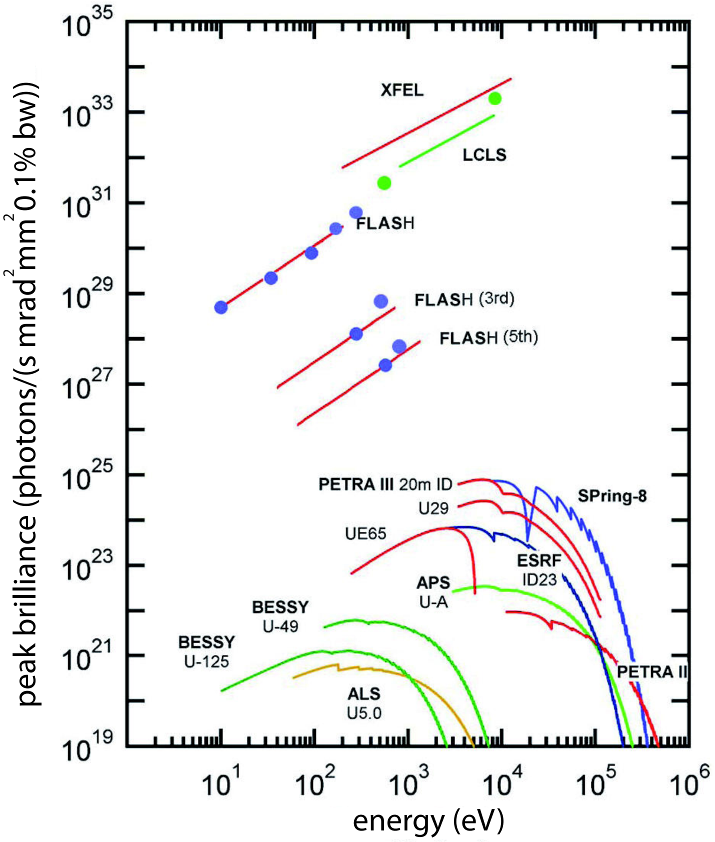

Figure 1.1: Peak brilliance of different light sources. Courtesy of S. Schreiber, DESY.

limited by their pulse duration. Due to the spectral and temporal stability high harmonics are the tool of choice for monitoring atomic-scale dynamics [T.Pfeifer, 2006]. Pump-probe experiments [Uphues et al., 2008; Allison, 2010] and diffractive imaging [Ravasio et al., 2009; Sandberg et al., 2007] for instance are some applications of HHG.

1.2 Self-amplified spontaneous emission

The most common operation mode of an FEL is Self-Amplified Spontaneous Emission (SASE), producing highly-brilliant radiation down to the XUV and x-ray regime. In contrast to synchrotrons the light pulses of an FEL have a much higher brilliance (figure 1.1) and are coherent. The pulse duration is in the femtosecond regime and is much shorter than the picosecond pulses delivered by synchrotrons. The pulse energy exceeds those of HHG by up to five orders of magnitude.

The radiation is suited for coherent x-ray diffraction imaging [Chapman et al., 2006; Bogan et al., 2008], inline holography [Rosenhahn et al., 2009], Fourier- transform- holography [Boutet et al., 2008; Mancuso et al., 2010; Marchesini et al., 2008], coherent x-ray resonant magnetic scattering [Gutt et al., 2010] and time-resolved pump-probe experiments [Krikunova et al., 2011; Chapman et al., 2007; Barty et al., 2008].

Unfortunately, the generation of the light pulses is based on a statistical process, leading to erratic fluctuations of the pulse energy and the spectral and temporal domain [Ackermann et al., 2007]. Moreover, the electron acceleration process introduces arrival time fluctuations of the electron bunch at the undulator entrance, which leads to a temporal jitter with respect to external laser pulses. Thus, the resolution of time-dependent pump-probe experiments is reduced [Drescher et al., 2010; Maltezopoulos et al., 2008; Azima et al., 2007; Radcliffe et al., 2007].

1.3 HHG vs. SASE

Both, HHG and SASE are techniques to generate XUV radiation for time-resolved experiments. HHG is able to provide coherent radiation in the nanojoule regime. In contrast the pulse energy of FLASH is up to 300 µJ [Schreiber, 2011b]. Due to the stochastic nature of SASE the radiation differs in its spectrum and intensity on a shot-to-shot basis. These jitter sources are absent in HHG.

In HHG the radiation consists of odd multiples of the driving laser frequency. The lowest produced wavelength depends on the fundamental wavelength and the target which usually is a noble gas. It is further possible to shift and/ or broaden the spectrum slightly at the expense of the pulse energy. In an FEL the wavelength depends on the electron energy and on the K-parameter of the used undulators and can be changed continuously. FLASH for instance can produce radiation with $4.1\ \text{nm} < \lambda < 47\ \text{nm}$ [Schreiber et al., 2011; Tiedtke et al., 2009].

The pulse length of the FEL radiation depends on the electron bunch and it is possible to change the pulse length of FLASH between $10\ \text{fs} < \Delta t < 200\ \text{fs}$ (rms) [Schreiber, 2011b]. In contrast, the pulse length of the HHG related radiation is determined by the pulse length of the driving laser. Furthermore, the driving laser pulse length has a large impact on the CE. Thus, the pulse length of the harmonics is more or less fixed. On the other hand, the arrival time jitter of the radiation is only determined by the jitter of the driving laser. In contrast to an FEL, where the acceleration process introduces arrival time fluctuations in the order of $FWHM \approx 80$ fs (Full Width at Half Maximum) [Schreiber, 2011b]. Thus, the temporal jitter of an FEL is much larger compared to HHG.

1.4 Seeded FELs

Seeding an FEL is an alternative technique to SASE, where the lasing process is initiated by an external laser and not from spontaneous emission. The external laser introduces a density modulation of the electron bunch leading to coherent radiation. In this case, only a fraction of the electron bunch is being modulated, thus the pulse length of the corresponding radiation depends on the seed pulse length. In addition, the amplification process takes place only within the pulse length. Hence, the arrival time fluctuations of the electron bunch has no impact on the corresponding radiation as long as the arrival-time jitter is smaller than the width of the electron bunch.

The wavelength of the radiation is determined by the seed, thus, it is an odd multiple of the HHG driving laser. The pulse energy of a seeded FEL should be comparable to SASE radiation in the microjoule regime [Miltchev et al., 2008].

In summary, a seeded FEL combines the advantages of the stability of HHG and the high power of SASE. Therefore, one is able to improve the time resolution of corresponding experiments and to enhance the energy resolution of wavelength-dependent experiments. So far FLASH is operated in the SASE mode. This thesis describes the joint venture between the University of Hamburg and DESY, where the FLASH facility is upgraded to a seeded FEL (sFLASH). It is meant to get further insights of the peculiarities of a seeded operation mode and is a first step towards a seeded user facility (FLASH II).

1.5 Thesis structure

This thesis is separated into five chapters. The following chapter describes the fundamental physical concepts of HHG and FEL theory necessary to understand this thesis. In chapter 3 the experimental environment, i.e. FLASH, sFLASH, and the constructed harmonic source are described. Chapter 4 is the main part of this thesis and describes the characterization of the harmonic source and the achievements of the seeding experiment at FLASH. Chapter 5 concludes and presents an outlook of sFLASH. Finally, the appendix contains among technical details a manual how to set up the harmonic source.

Fundamentals

2

This chapter is addressed to the fundamentals of this thesis. Primarily the theoretical concept of HHG and FEL theory will be presented.

2.1 Description of laser pulses

The behavior of laser pulses is based on optics and has been investigated thoroughly in the past. A comprehensive description can be found in [Saleh and Teich, 1991; Hecht and Zajac, 1997; Frank L. Pedrotti, 1987; L.Bergmann et al., 2004]. This chapter only accounts for the fundamentals and summarizes the necessary issues to understand the following chapters.

2.1.1 Geometrical optics

The simplest way to describe the behavior of light is in terms of geometrical optics. The theory is based on a few postulates as described for instance in [Saleh and Teich, 1991]. It is assumed that light travels in form of rays in a medium which is described by the refractive index. The path of the rays is determined by Fermat's principle: *"Light rays travel along the path of least time"*. Based on these three principles the propagation of light rays is determined.

For rays having a small angle ϑ to the optical axis of an optical element, their behavior is described by the paraxial approximation: $\sin(\vartheta) \approx \vartheta$. One consequence is the image equation for a thin lens or a spherical mirror:

$$\frac{1}{b} + \frac{1}{g} = \frac{1}{f}\,, \tag{2.1}$$

where g is the distance from the object to the lens, b is the distance from the lens to the image, and f is the focal length of the lens. The equation can be employed to calculate the position of an image depending on the distance of the object to the focusing optic. The paraxial approximation lacks on the fact that aberrations as for instance astigmatism cannot be described. Astigmatism is induced, whenever the light rays have a large angle ϑ to the optical axis of the focusing element. In this case, two line foci appear instead of one point focus. The line foci in the sagittal and meridional plane are separated in space:

$$\begin{aligned} f_m &= f \cdot \sin(\vartheta) \\ f_s &= f \cdot \tfrac{1}{\sin(\vartheta)}, \end{aligned} \tag{2.2}$$

where f_m, and f_s are the effective focal lengths of the meridional and sagittal plane, respectively.

In general, geometrical optics is an idealized model and implies that $\lambda \to 0$. It is not possible to describe effects like interference or diffraction. To account for the wave nature of light the electromagnetic field theory has to be used. Some major results will be presented within the next section.

2.1.2 Gauss optics

Light can be described with the Maxwell equations and it is possible to deduce simple statements by employing some assumptions. Firstly, the wave equation

$$\nabla^2 \vec{E} = \frac{1}{c^2} \frac{\partial^2 \vec{E}}{\partial t^2}, \tag{2.3}$$

with $\vec{E}$ the electric field, c the speed of light, and t the time is a direct consequence of the Maxwell equations. For an electromagnetic wave

$$\vec{E}(\vec{r}, t) = \mathcal{E}(\vec{r}) \mathcal{T}(t)$$

equation 2.3 can be separated in space and time and can be rewritten as:

$$\begin{aligned} \left(\nabla^2 + k^2\right) \mathcal{E}(\vec{r}) &= 0, && (2.4) \\ \left(\tfrac{d^2}{dt^2} + \omega^2\right) \mathcal{T}(t) &= 0, && (2.5) \\ \text{with} \quad \omega &= kc, \\ \text{and} \quad k &= \tfrac{2\pi}{\lambda}, \end{aligned}$$

where ω is the angular frequency, k is the wave vector, and λ is the wavelength. Equation 2.4 is known as the Helmholtz equation. Assuming an electromagnetic wave traveling along the z-direction with a slowly varying envelope (paraxial approximation), one solution of equation 2.4 corresponds to a Gaussian beam [Jackson, 1999] with

$$\begin{aligned} w(z) &= w_0 \sqrt{1 + \left[\frac{z}{z_R}\right]^2} && (2.6) \\ R(z) &= z \left[1 + \left(\frac{z_R}{z}\right)^2\right] && (2.7) \\ \zeta(z) &= \tan^{-1}\left(\frac{z}{z_R}\right) && (2.8) \\ w_0 &= \sqrt{\frac{\lambda z_R}{\pi}}, && (2.9) \end{aligned}$$

where $w(z)$ is the beam width depending on the spatial coordinate z and z_R the Rayleigh length. $R(z)$ corresponds to the wavefront radius of curvature, $\zeta(z)$ represents the phase

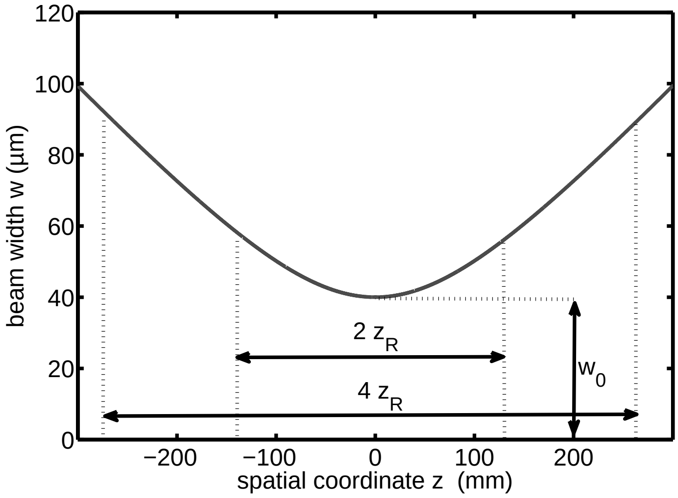

Figure 2.1: Calculated beam width for a Gaussian beam with $\lambda = 38.1$ nm, $w_0 = 40$ µm, and $z_R = 132$ mm.

retardation of the beam relative to a uniform plane wave, and w_0 is the minimal beam width at its waist depending on the wavelength λ and on the Rayleigh length z_R. In figure 2.1 the calculated beam width $w(z)$ is shown for a Gaussian beam with $\lambda = 38.1$ nm and $w_0 = 40$ µm. In this case the beam width w at position z is defined in terms of the intensity: the Gaussian beam has its peak intensity on axis for every position z. The beam radius w, however, is defined as the radial distance to the optical axis at which the intensity is reduced to $1/e^2$ of its peak intensity. Also the Rayleigh length depends on the beam waist and refers to the distance z at which the focal spot area is twice as big as at its waist $w(z = 0) = w_0$, i.e. the beam radius is $\sqrt{2}w_0$. The intensity at that position is

$$I(z = \pm z_R) = 0.5 \cdot I(z = 0).$$

Depending on the context different definitions of the beam waist are used. As explained before w corresponds to the radius, where the intensity decreases by a factor of $1/e^2$. In contrast, the FWHM value of a beam is defined as the diameter of the beam at which the intensity drops down by a factor of two. The rms width σ of a beam is defined as the mean of the photon-distribution. In case of a Gaussian beam the rms-width (root mean square) is half as big as the w-radius ($w = 2\sigma$). The different definitions of the Gaussian beam widths are connected as follows:

$$\mathrm{FWHM} = 1.177w = 2.35\sigma$$

Besides, figure 2.1 indicates that the beam width increases linearly in the near field. For $z \gg z_R$ equation 2.6 can be rewritten as

$$\begin{aligned} w(z) &= \frac{w_0}{z_R} \cdot z \\ w(z) &= \tan(\vartheta) \cdot z \end{aligned} \tag{2.10}$$

The divergence, i.e. half opening angle of the cone can be expressed by combining equation 2.9 and 2.10.

$$\begin{aligned} \vartheta &= \frac{w_0}{z_R} = \frac{\lambda}{\pi w_0}, \qquad (2.11) \\ \text{with} &\qquad \tan(\vartheta) \approx \vartheta. \end{aligned}$$

The phase retardation $\zeta(z)$ of a Gaussian beam (equation 2.8) changes its sign at the position of the waist [Gouy, 1890]. This effect is known as the Guoy phase-shift $\Delta\zeta = \pi$ between the near field on each side of the focus.

Strictly speaking, the above equations are only valid for a Gaussian TEM_0 in x- and y-direction, respectively. [Siegman, 1993] introduced the beam quality factor M^2 to extend the above equations. The beam quality- or beam propagation- factor is defined as *“the times diffraction limited (TDL) value for an arbitrary real beam compared to a* TEM_0 *Gaussian beam"*. It is further shown that the above equation have to be modified in a way that $\lambda \to M^2\lambda$, where $M^2 \geq 1$ in order to describe modes deviating from TEM_0 mode in x- and y- direction. During this work the modified beam width, as well as the modified Rayleigh length is being used. The equations 2.6 and 2.9 can be rewritten as

$$W(z) = W_0\sqrt{1 + \left(\frac{z}{z_R}\right)^2} \qquad (2.12)$$

$$\text{with} \qquad z_R = \frac{\pi W_0^2}{M^2\lambda}, \qquad (2.13)$$

where W_0 is the modified beam waist. During this work laser pulses are assumed to be Gaussian in the spatial and spectral domain, unless it is explicitly noted to be different. A detailed deduction of Gaussian beam properties can be found in [Siegman, 1986]. Laser related fundamentals are further discussed in [Svelto, 1982; Rulliere, 1998].

2.2 XUV optics

The XUV regime is in the range of $10\ \mathrm{nm} \leq \lambda \leq 120\ \mathrm{nm}$. Unfortunately, there are no existing materials having a high reflectivity within this regime. Most of the radiation is being absorbed within a penetration depth of less than $1\ \mu\mathrm{m}$, leading to typical reflectivity of $R \leq 10^{-4}$ at normal incidence [Jaeglé, 2006]. A solution to overcome this peculiarity are grazing incidence mirrors, as well as normal incidence multilayer mirrors. Grazing incidence mirrors have a large bandwidth compared to multilayer mirrors. As explained in chapter 2.1.1 a focusing optic employed at a grazing incidence angle leads to an astigmatism, which is usually not wanted. Thus, grazing incidence mirrors are commonly used for simple (non-imaging) reflections. In contrast, multilayer mirrors can be employed at angles around zero degree. Those mirrors consist of a periodic thin layer structure on top of the substrate, leading to constructive interference of the reflected XUV radiation. The achieved bandwidth is small compared to the grazing incidence mirrors, but the focused beam does not suffer from astigmatism. A more detailed description of XUV optics can be found in [Jaeglé, 2006; Attwood, 2000]. [Lawrence Berkeley National Laboratory, 2011] provides a web-interface to calculate the reflectivity and transmission of various materials. A report on diffraction gratings in the XUV regime which are used in this thesis has been given by [Schroedter, 2009] and basic grating theory can be found in [Palmer and Loewen, 2005].

2.3 High Harmonic Generation

HHG is a coherent nonlinear interaction of light and matter [Shen, 1984; Menzel, 2001]: if a high intensity laser is focused into a gas target, the atoms emit light pulses of odd multiples of the incident frequency [W.F.Drake, 2006; Jaeglé, 2006]. The first observation of optical harmonics (second harmonic generation) has been described in 1961 [Franken et al., 1961] one year after the invention of the laser [Maiman, 1960]. First experiments on low-order harmonic generation in gas have been published in [New and Ward, 1967; Ward and New, 1969], whereas the first high-order harmonics have been observed in the late 1980s [McPherson et al., 1987; M.Ferray et al., 1988]. Early published results are reviewed in [Huillier et al., 1991; Gavrila, 1992]. More recent reviews can be found in [Winterfeldt et al., 2008; Brabec and Krausz, 2000]. In table 2.1 a selection of harmonics generated with an 800 nm Ti:Sa laser are shown, where H21 will draw an increased attention during the following work.

Table 2.1: Selected harmonic orders in different units.

harmonic order	λ (nm)	E_{photon} (eV)
H01	800	1.55
H09	88.9	13.95
H11	72.7	17.05
H13	61.5	20.15
H19	42.1	29.45
H21	38.1	32.55
H23	34.8	35.65
H61	13.1	94.54

2.3.1 Three-step model

A simple empiric model has been developed to describe the process of HHG [Corkum, 1993; Kulander et al., 1993]. It is widely known as the simple man's model, the three-step model, or in the 1990s as the "two-step quasi-classical approach" [L'Huillier et al., 1993]. The model describes how the bound electrons of the gas atoms tunnel through its atomic barrier. In the second step the electrons move classically and may return to the nucleus. Those electrons that recombine to the ground state emit harmonics as illustrated in figure 2.2. Today the model is separated into three steps and is described as follows:

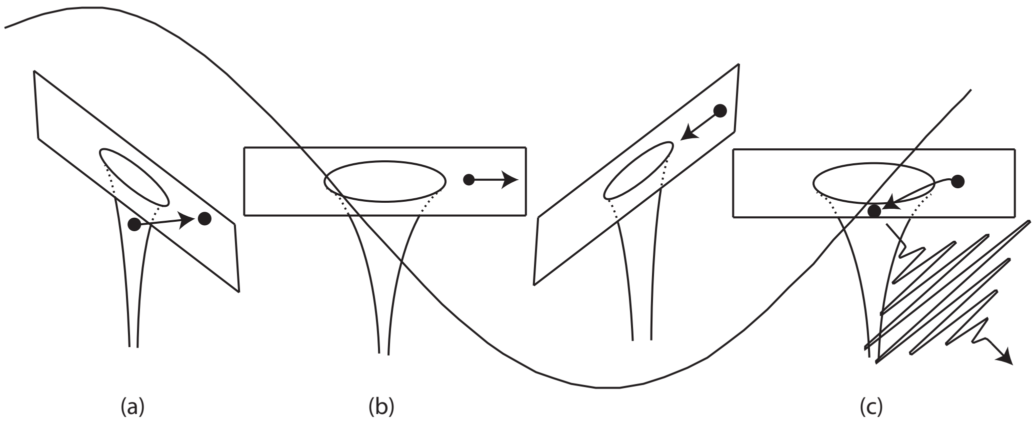

Figure 2.2: Schematic representation of the three-step model: (a) represents the tunnel ionization, (b) the acceleration in the continuum, and (c) the recombination.

First step: ionization

Whenever a laser is focused down to intensities in the order of 10^{15} W/cm^2 the amplitude of the corresponding electric field approaches 10^9 V/cm. These field strengths exceed that of an atomic Coulomb field, leading to a deformation of its atomic potential. Hence, this deformation increases the possibility for a bound electron to tunnel through its atomic barrier. Tunnel ionization has firstly been described for hydrogen [Keldysh, 1665] and was extended to a generalized theory for arbitrary atoms [Ammosov et al., 1986].

In summary, the theory introduces the Keldysh parameter [Miyazaki and Takada, 1995]:

$$\gamma = \sqrt{\frac{I_p}{2U_p}},$$

where I_p is the ionization potential of the gas and U_p is the ponderomotive potential. The ponderomotive potential corresponds to the averaged energy of the electron's quiver motion in an electromagnetic field and is directly proportional to the wavelength square of the driving laser. It is defined as

$$U_p = \frac{e^2}{2m_e\epsilon_0 c\omega^2} I \propto I\lambda^2,$$

where e is the elementary particle charge, m_e the electron mass, ϵ_0 the vacuum permittivity, c the speed of light, ω the angular frequency, I the laser intensity, and λ is the wavelength of the laser. However, for $\gamma > 1$ the ionization takes place in terms of multi-photon ionization [Lin, 2006] and for $\gamma < 1$ through tunneling. Multi-photon ionization is a simultaneous absorption of several photons, leading to the ionization of the atom [Mainfray and Manus, 1991].

The number of electrons N_e can be deduced as in [Miyazaki and Takada, 1995] and is described by the rate equation

$$dN_e(t) = N(t)W(t, E)dt,$$

where $N(t)$ is the time dependent neutral atom density and $W(t, E)$ the tunnel ionization rate. The ionization rate depends on the field strength E and leads to an electron density [Ammosov et al., 1986]

$$N_e(t) = N_0 \left[1 - \exp\left(-\int_{-\infty}^{t} W(t, E)dt\right)\right],$$

where N_0 is the neutral atom density at $t = 0$.

Besides, ionization of the gaseous medium changes the diffractive index and may lead to self-focusing of the driving laser which itself has influence on the HHG process. HHG in a rapid ionizing medium has been described thoroughly in [Rae et al., 1994; Rae and Burnett, 1993a,b]. However, laser fields in the order of the atomic Coulomb field of $10^8 - 10^9$ V/cm, necessary to drive the HHG process, are known as strong fields where the classical perturbation theory is not valid [Brabec, 2008].

Second step: propagation

As soon as the electron is ionized it is treated as a free-electron and its subsequent trajectory is determined by the laser field. Depending on the phase of the laser field at the time of the ionization the electrons gain different energies before the electric field changes its algebraic sign. The sign change causes the electron to decelerate and then to accelerate back to the parent ion. The averaged kinetic energy an electron can gain in an oscillatory laser field is [Gallagher, 1988; Krause et al., 1992]:

$$\left\langle \frac{1}{2} m_e v^2 \right\rangle = U_p \left(1 + 2\cos^2(\omega t_0)\right),$$

where v is the velocity and t_0 is the ionization time. This equation indicates that the energy an electron can gain is between U_p and $3U_p$. Classical simulations of the propagation have been published in [Corkum, 1993] and reveal a slight modification of the previously deduced result. It is shown that the maximal energy an electron can gain is $3.17U_p$. It is also shown that an electron, which gained the energy of $3.17U_p$ has tunneled at $\omega t_0 = 17°$or $197°$ of the driving laser. Thus, the maximal energy an electron can gain occurs twice a laser cycle. Here it is perspicuous that for an elliptical polarization of the driving laser the electron never returns to the parent ion. Thus, the CE of HHG is strongly dependent on the ellipticity of the driving laser polarization [Budil et al., 1993; Dietrich et al., 1994; Schulze et al., 1998].

Third step: recombination

Some of the free-electrons may recombine with their parent ion and emit a photon with a maximal energy of

$$E_{max} = 3.17U_p + I_p, \tag{2.14}$$

where I_p is the ionization potential of the corresponding gas atoms. Equation 2.14 is known as the cutoff law and describes the cutoff behavior of the harmonic spectrum

[L'Huillier et al., 1993]. The smallest possible wavelength in the harmonic spectrum depends on

- the wavelength of the driving laser,
- the intensity of the driving laser,
- and the ionization potential of the gaseous medium.

The larger the wavelength, intensity, and ionization potential, the smaller gets the wavelength of the highest harmonic order.

In summary, the three-step model is a quasi-classical model which describes the HHG process within three distinct steps. A self-contained fully quantum mechanical description of the HHG process is given in [Lewenstein et al., 1994] and will be described in the following section.

2.3.2 Quantum mechanical description

The quantum mechanical description of the HHG process is based on the single active electron (SAE) approximation [Kulander and Rescigno, 1991] and is known as the strong field approximation (SFA) or as the Lewenstein model [Lewenstein et al., 1994]. In the SAE approximation it is assumed that the bound state wave function evolves into a continuum wave packet. One part of the wave packet will never return, whereat another part will return to the ionic core. Here different possibilities a probable. Either the electron scatters off, or changes the direction to gain energy, or overlaps with the bound state, which leads to a time dependent dipole moment and photo emission. The system can be described with the corresponding time-dependent Schrödinger (TDSE) equation

$$i\hbar\frac{\partial}{\partial t}|\Psi(\vec{r},t)\rangle = \left[-\frac{\hbar^2}{2m_e}\hat{\nabla}^2 + \hat{V}(\vec{r}) - \vec{E}(t)\hat{x}\right]|\Psi(\vec{r},t)\rangle, \tag{2.15}$$

where $\hat{V}(\vec{r})$ is the atomic potential operator, $\vec{E}(t)$ is the time-dependent laser field, and $\hat{x}$ is the dipole operator. However, the solution of equation 2.15 is a superposition of bound, oscillating, and outgoing wave packets. In order to solve the TDSE the following approximations have to be made:

- the system evolution depends only on the ground state $|0\rangle$. All other states do not contribute and can be neglected.
- depletion of the ground state can be neglected.
- the electron in the continuum moves as a free-electron in an electric field, thus the atomic potential has no effect and can be neglected.
- the laser field is assumed to be linearly polarized $\vec{E}(t) = (E(t)\cos(\omega t), 0, 0)$

The Fourier transform of the induced dipole moment

$$ex(t) = \langle\Psi(x,t)|ex|\Psi(x,t)\rangle \tag{2.16}$$

leads directly to the harmonic spectrum.

The ansatz

$$|\Psi(x,t)\rangle = e^{iI_p t/\hbar}\left(a(t)|0\rangle + \int d^3\vec{q}\; b(\vec{q},t)|\vec{q}\rangle\right), \tag{2.17}$$

where $a(t)$ is the ground state amplitude and $b(\vec{q},t)$ is the amplitude of the continuum states, leads to the solution of the TDSE. Because the depletion of the ground state is neglected, the amplitude of the ground state is set to $a(t) \approx 0$, $\dot{a}(t) \approx 0$. Equation 2.16 can be evaluated by further changing the variables to the canonical momentum $\vec{p} = \vec{q} + e\vec{A}(t)/c$:

$$\begin{aligned} ex(t) &= i\int_0^t d\tau \left(\frac{2m_e\hbar\pi}{\nu + i\tau}\right)^{3/2} \\ &\quad \times\; d_x^*(\vec{p}_s - e\vec{A}(t)/c)\cdot \quad e^{-iS(\vec{p}_s,t,\tau)} \\ &\quad \times\; E(t-\tau)\cos(\omega(t-\tau))d_x(\vec{p}_s - e\vec{A}(t-\tau)/c) \quad + \text{c.c.} \end{aligned} \tag{2.18}$$

$$\text{with} \qquad \vec{p}_s = \vec{p}_s(t,\tau) = \int_{t-\tau}^{t} dt'\; e\vec{A}(t')/c\tau$$

$$\text{and} \qquad S(\vec{p}_s,t,\tau) = \int_\tau^t dt'' \left(\frac{(\vec{p}_s - e\vec{A}(t'')/c^2)^2}{2m_e} + I_p\right),$$

where $d_x(\vec{q}) = \langle\vec{q}|ex|0\rangle$ is the component of the dipole matrix element parallel to the polarization for bound-free transitions, d_x^* its complex conjugate, $S(\vec{p}_s,t,\tau)$ is the quasi-classical action, $\vec{p}_s$ the momentum at the stationary point of the quasi-classical momentum, and $\tau = t - t'$ is the time the electron is travelling in the continuum. Equation 2.18 can be interpreted in terms of the simple man's model: the bottom line contains the matrix element for the transition between the bound state and the continuum, $S(\mathbf{p}_s,t,\tau)$ corresponds to the propagation operator in the continuum, and d_x^* corresponds to the transition from the continuum back into a bound state.

A Fourier transformation of equation 2.18 calculates the harmonic spectrum. It can further be shown [Salieres et al., 2001] that the kth Fourier component corresponds to a sum over the quantum orbits

$$ex_k = \sum_n a_n \exp(-iS(\mathbf{p}_n, t_n, t_\tau)),$$

i.e. the kth harmonic depends on interfering contributions of different trajectories (Feynman's path integral). Finally, it should be pointed out that this model is also able to reproduce the cutoff law of the simple man's model [Lewenstein et al., 1994]. Equation 2.14 has to be modified:

$$E_{max} = 3.17U_p + I_p \cdot F(U_p/I_p), \tag{2.19}$$

where the factor $F(U_p/I_p)$ is a correction term due to quantum tunneling and quantum diffusion. $F(U_p/I_p)$ is equal to 1.3 for $I_p \ll U_p$ and decreases to 1 as I_p grows.

HHG is a periodic process which occurs every half laser cycle. Moreover, one can observe that two electron trajectories ionized at different phases of the laser field will result in identical momenta at the time of re-collision [Lewenstein et al., 1995; Balcou et al., 1999; Milošević and Becker, 2002; Liu et al., 2009]. These two trajectories are known as the short and the long trajectory corresponding to the time the electron is traveling through the continuum. Since the process takes place every half period of the laser cycle $T/2$ the Fourier transform is a discrete function with a separation corresponding to $1/(T/2) = 2f$. That is why the spectrum consists only of odd multiple of the frequency of the driving laser [Winterfeldt et al., 2008]. This symmetry can be avoided by adding the second harmonic of the driving laser to the HHG process [Mauritsson et al., 2006].

2.3.3 Phase matching

So far only a single atom has been considered. However, HHG is a multi-particle process and the collective effects have to be taken into account. For efficient HHG the phase-conditions of the atoms have to be set that the corresponding radiation adds constructively. The wave-vector mismatch of the q^{th} harmonic order can be written as

$$\Delta k = qk(\omega_f) - k(q\omega_f), \tag{2.20}$$

where k represents the wave-vector, q is the harmonic order, and ω_f is the frequency of the driving laser. Equation 2.20 and the following is mainly taken from [T.Pfeifer, 2006]. The wave-vector $k = k(\omega)$ depends on its frequency. It can be written as

$$k(\omega) = k_{vac}(\omega) + k_{disp}(\omega) + k_{plasma}(\omega) + k_{geom}(\omega), \tag{2.21}$$

where $k_{vac}(\omega) = 2\pi\omega/c$ is the wave-vector in free space, $k_{disp}(\omega)$ is the contribution due to dispersion in a neutral medium, $k_{plasma}(\omega)$ is due to dispersion in a plasma, and $k_{geom}(\omega)$ is due to geometric dispersion. Constructive interference occurs, if the phase-mismatch vanishes:

$$\Delta k = 0.$$

The phase-mismatch in free space

$$\Delta k_{vac} = q\frac{\omega_f}{c} - \frac{q\omega_f}{c} = 0 \tag{2.22}$$

is zero, thus, only the dispersion due to neutral atoms, plasma, and geometrical effects have to be considered. As the the refractive index of a medium depends on the wavelength the phase-mismatch due to dispersion in a neutral medium can be expressed as

$$\Delta k_{disp}(\omega_f) = (n(\omega_f) - n(q\omega_f))\frac{q\omega_f}{c}, \tag{2.23}$$

where n is the refractive index. This contribution to the phase-mismatch depends only on the difference of the refractive indices. In case of the 800 nm driving laser the refractive index is larger than one and smaller than one for the XUV radiation, thus, the wave-vector mismatch is a positive value.

As explained in the previous section only a fraction of the ionized electrons recombine and emit harmonic radiation. The majority of the electrons remain ionized and lead to a change of the refractive index:

$$\begin{aligned} n_{\text{plasma}}(\omega) &= \sqrt{1-\left(\frac{\omega_p}{\omega}\right)^2} \\ \text{with} \qquad \omega_p &= \sqrt{\frac{e^2 N_e}{\epsilon_0 m_e}}, \end{aligned}$$

where ω_p is the plasma frequency. The corresponding plasma contribution to the phase-mismatch can be calculated:

$$\Delta k_{\text{plasma}}(\omega) = q k_{\text{plasma}}(\omega_f) - k_{\text{plasma}}(q\omega_f) = \frac{\omega_p^2(1-q^2)}{2qc\omega_f} \tag{2.24}$$

and is

$$\Delta k_{\text{plasma}}(\omega) < 0$$

for $q > 1$.

The last contribution in equation 2.21 depends on the focusing properties of the driving laser. As explained in chapter 2.1.2 the focused Gaussian beam contains an additional phase contribution along the z-direction which is known as the Guoy phase (equation 2.8). The wave-vector can be approximated for $z << z_R$ to

$$k_{\text{geom}}(z) = \frac{d\zeta(z)}{dz} \approx \frac{1}{z_R}.$$

Thus, the phase-mismatch is:

$$\Delta k_{\text{geom}} = q k_{\text{geom}}(\omega_f) - k_{\text{geom}}(q\omega_f) = \frac{q-1}{z_R}. \tag{2.25}$$

The total phase-mismatch can be calculated by combining equation 2.20 - 2.25:

$$\Delta k_{\text{tot}} = \underbrace{(n(\omega_f) - n(q\omega_f))\frac{q\omega_f}{c}}_{>0} + \underbrace{\frac{\omega_p^2(1-q^2)}{2qc\omega_f}}_{<0} + \underbrace{\frac{q-1}{z_R}}_{>0}. \tag{2.26}$$

In order to achieve constructive interference the phase-mismatch introduced by free electrons have to cancel out the mismatch due to dispersion and geometrical considerations. During this work only loose focusing geometries are used and therefore the geometrical part of the phase-mismatch can be neglected. Thus, the phase-mismatch is only due to free-electrons and dispersion in the neutral medium, i.e. argon. Note that HHG in hollow waveguides introduces an additional term, which is addressed to waveguide dispersion [Durfee et al., 1999]. This term is absent during this work an cannot be used to optimize the phase-matching conditions.

2.3.4 Properties of the harmonics

In figure 2.3 a typical HHG spectrum is plotted schematically. The spectrum can be divided in three sections: the perturbative regime of the lower harmonics which can be treated with the lowest-order perturbation theory [Gavrila, 1992], the mid-harmonics which form a plateau, and the highest harmonics in the cutoff. The high-order harmonics of the plateau and the cutoff regime are described in terms of the SFA, which is not valid for lower orders. Here the atomic potential has an influence on the electron's movement, thus the approximations made in the SFA are not fulfilled anymore (chapter 2.3.2).

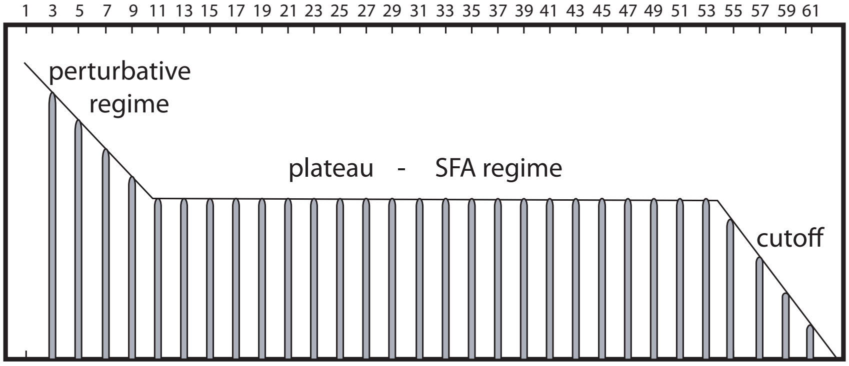

Figure 2.3: Schematic representation of a typical HHG spectrum (odd orders shown on top).

As explained before, the harmonics are separated by $2\omega_f$, where ω_f is the frequency of the driving laser. The spectral bandwidth of each harmonic depends on the intensity of the driving laser [He et al., 2009] and is larger, if the long electron trajectory is favored, thus for higher laser intensities. Moreover, destructive interference between the long and the short trajectory may occur at high intensities [Xu et al., 2008; Brunetti et al., 2008; Zaïr et al., 2008]. It is further possible to slightly shift the harmonics towards lower wavelengths. As explained in chapter 2.3.1 the probability to ionize an atom depends on the intensity of the driving laser. Thus, for high intensities the number of free-electrons increases and the refractive index changes (section 2.3.3). This variation of the refractive index leads to a spectral blueshift of the driving laser and therefore to a blueshift of the harmonics [Wahlström et al., 1993]. Detailed calculations can be found in [L'Huillier et al., 1992; Rae and Burnett, 1993a; Rae et al., 1994; Kan et al., 1995].

The harmonics form a train of attosecond pulses in the time domain [Paul et al., 2001; Antoine et al., 1996]. In order to measure the attosecond pulse structure of the harmonics, the phase difference between two consecutive harmonics is measured. This measurement is based on a cross-correlation technique based on a two photon transition. The technique RABITT (Reconstruction of Attosecond harmonic Beating By Interference of Two-photon Transitions) uses the fact that the driving laser frequency is exactly half of the frequency spacing between two consecutive harmonics. If one focuses the harmonics and the driving laser into a gas, the spectrum consists of peaks corresponding to the harmonic orders. If in addition the driving laser overlaps in space and time, sidebands appear which depend on the relative phase of the consecutive harmonics and the time-delay of the driving laser. In this way, the phase difference can be deduced. In combination with the harmonic amplitude the temporal profile can be reconstructed [Hentschel et al., 2001; Paul et al., 2001; Kienberger et al., 2002]. Moreover, the time-dependent frequency can be measured and depends linearly on the harmonic order and on the chirp of the driving laser [Mauritsson et al., 2004; Norin et al., 2002].

The coherence time has to be considered separately for the long and for the short trajectory. The short trajectory has a phase that does not vary much with intensity, thus the emitted radiation has a long coherence time and is well collimated [Lewenstein et al., 1995]. In contrast the phase of the long trajectory changes rapidly with the laser intensity [Gaarde et al., 1999], therefore, a shorter coherence time and a more divergent emission appears [Salières et al., 1995]. The spatial coherence has been investigated by a series of a two-slit experiments. It has been shown that for moderate laser intensities the harmonics have a high degree of spatial coherence. For high intensities the spatial coherence is reduced, due to the time-dependent index of refraction [Ditmire et al., 1996; Bartels et al., 2002].

2.4 Free Electron Laser

In 1971 the principle of an FEL has been proposed by [Madey, 1971]. After the first observation of magnetic bremsstrahlung at 10.6 μm [Elias et al., 1976] the first FEL oscillator [Deacon et al., 1977] went into operation. Today, almost 35 years later, a variety of different FEL facilities have been constructed in order to provide high-brightness, coherent, ultrashort, and short wavelength radiation to the scientific community. For example LCLS [Emma, 2009; Boutet and Williams, 2010], XFEL at Spring-8 [Shintake, 2010; Hara et al., 2010] and the European XFEL [Schneidmiller and Yurkov, 2010] are able to produce FEL-radiation with a wavelength in the order of 0.1 nm, while other facilities like FLASH (chapter 3.1), SCSS at SPring-8 [Shintake, 2010], FERMI at Elettra [Allaria et al., 2010], and the SwissFEL [Garvey, 2010; Patterson et al., 2010] are operating in the VUV and the soft X-ray regime.

In contrast to the synchrotron light sources, the FELs generate photon pulses with a much higher degree of coherence and a pulse length down to the femtosecond range. The HHG sources, on the other hand, are also capable to emit ultra-short coherent XUV-pulses, but with an energy in the nanojoules regime, while FELs typically deliver micro- or millijoule pulses. FLASH for instance is able to deliver pulses up to 300 μJ [Treusch and Feldhaus, 2010], whereas LCLS has observed a pulse energy of 3 mJ [LCLS, 2011].

Due to the phase and amplitude jitter of the accelerating electric field, the electron bunches arrive at different times at the undulator entrance compared to an external laser (arrival-time jitter). In the SASE operation mode, the FEL amplifies the spontaneous radiation produced in the beginning of the undulator section. The stochastic nature of the SASE start-up process leads to spectral and intensity fluctuations of the light pulses on a shot-to-shot basis (spectral and intensity jitter). Furthermore, the pulse shape and the pulse length differs from shot to shot.

This chapter is on the one hand directed to the fundamentals associated with the origins of shot-to-shot fluctuations, and on the other hand to alternative operation modes of an FEL. Details on FEL related processes can be found in [Schreiber, 2010; Schmüser et al., 2008; Huang and Kim, 2007; Saldin et al., 1999b].

2.4.1 Electron source and acceleration

The electrons are generated by a laser driven photocathode and are subsequently accelerated in a RF cavity generating electron bunches with a length in the picosecond regime. The technical solution as well as a detailed characterization is given in [Stephan et al., 2010; Fraser et al., 1986]. However, the light pulses of the driving laser have a temporal shot-to-shot jitter relative to the synchronization system which is transferred to the electron bunches. Additionally, the electrons experience temporal fluctuations of the RF phase leading to a further arrival time jitter of the electron bunches relative to the synchronization system.

In order to produce ultra-relativistic electron bunches with a high peak current the electrons are accelerated downstream the superconducting RF accelerating modules and are longitudinally compressed using the bunch compressors realized as four dipole magnetic chicanes. As in case of the RF gun, depending on their longitudinal position the electrons experience a different RF phase during the acceleration in the RF-modules. This has a twofold effect - it induces a head-tail energy variation along the bunch and it also changes the mean energy and correspondingly the bunch arrival time. Especially the first accelerating module where the bunches are accelerated to almost the speed of light has a direct influence on the arrival time relative to the synchronization system. In the bunch compressor, depending on the momentum the electrons travel different pathways: the tail electrons with a lower momentum travel a shorter and the head electrons with a higher momentum travel a longer way. This leads to a longitudinal compression of the electron bunch.

Therefore, the arrival time fluctuations of the electron bunches are mainly introduced by the first acceleration module as well as the bunch compressor. The timing fluctuation caused by the electron gun is partly compensated by the bunch compressor. A detailed description of the acceleration process can be found in [Wiedemann, 2007]. The corresponding arrival time fluctuation of the electron bunches as well as techniques to reduce those erratic fluctuations is described in [Löhl, 2009].

2.4.2 Undulator radiation

The undulator is a periodic magnetic structure consisting of dipole magnets with alternating polarity as illustrated in figure 2.4. The following does only summarize the key aspects of undulators. Details can be found in [Hofmann, 2004] and [Duke, 2000]. Depending on the peak of the magnetic field B_0 and the undulator period λ_u the undulator

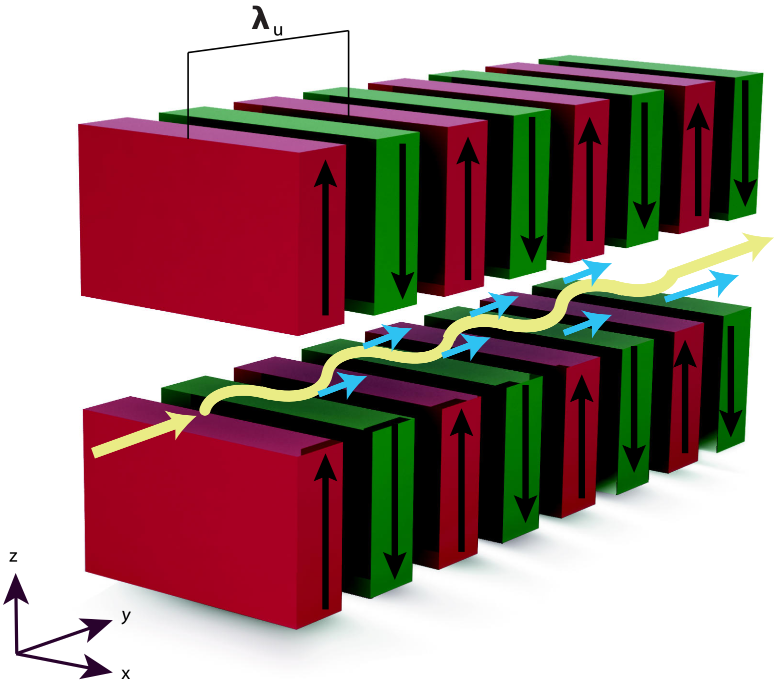

Figure 2.4: Schematic representation of an undulator: yellow is the sine-like trajectory of the electron and blue is the emitted radiation.

can be characterized with the undulator parameter

$$K = \frac{eB_0\lambda_u}{2\pi m_e c}. \tag{2.27}$$

An electron which travels through the undulator is due to the Lorentz force moving on a sine-like trajectory and emits synchrotron radiation. The radiation emitted at different positions in the undulator interferes and is concentrated in a narrow cone with an opening angle of $1/\gamma$, where $\gamma = \frac{E}{m_e c^2}$ is the Lorentzian factor. The fundamental wavelength of the undulator

$$\lambda_{ph} = \frac{\lambda_u}{2\gamma^2}\left(1 + \frac{K^2}{2} + \gamma^2\theta^2\right) \tag{2.28}$$

depends on the the undulator period λ_u, the energy of the electron, the undulator parameter, and the emission angle θ with respect to the beam axis. The on axis wavelength ($\theta = 0$) can be changed by tuning the electron energy or the magnetic field of the undulator. The electrons emit radiation independent of each other, thus, the radiation is incoherent for wavelengths smaller than the bunch length and its power is proportional to the number of electrons. The polarization of the radiation is perpendicular to the magnetic field and the spectral width is inversely proportional to the number of undulator periods.

2.4.3 High-gain free-electron laser

In the high-gain FELs, the initial current density in the electron bunch is periodically modulated at the radiation wavelength, thus creating the so-called microbunches. This microbunch structure leads to coherent radiation. As explained in section 2.4.2 the electrons move on a sine-like trajectory. Assumed they are superimposed with an electromagnetic wave they can gain or loose energy depending on the phase of the electron oscillation relative to the phase of the electromagnetic field. The energy transfer can be described with the following equation:

$$
\begin{aligned}
\tfrac{dW}{dt} &= \vec{v} \cdot \vec{F} \\
&= -e v_x(t) E_x(t), \\
&\propto \cos((k_l + k_u)z - \omega_l t + \psi_0) + \cos((k_l - k_u)z - \omega_l t + \psi_0) && (2.29) \\
&= \cos(\psi) + \cos(\chi) && (2.30)
\end{aligned}
$$

where dW is the transferred energy, t the time, $\vec{F}$ the Lorentzian force, $\vec{v}$ the velocity of the electron (see figure 2.4) and E_x is the magnitude of the electric field in x direction. k_l and k_u are the wave number of the light wave and the undulator, respectively, z the position in the undulator, ω_l the angular frequency of the light wave, and ψ in equation 2.30 is known as the ponderomotive phase. It has been shown [Schmüser et al., 2008] that a continuous energy transfer from the electron to the light wave along the undulator is present, if the ponderomotive phase is constant. Furthermore, the condition for a sustained energy transfer to the electromagnetic wave yields the same light wavelength as the on axis wavelength of an undulator (equation 2.28 on axis, i.e. $\theta = 0$). The phase of the electromagnetic wave is then shifted by π every half cycle of the oscillatory movement of the electrons. The energy transfer from the electrons to the light leads to a reduction of the electron momentum. The smaller the electron momentum, the smaller is the radius of the trajectory ($p = eB_0r$). This leads to a current density modulation of the electron bunch. [Schmüser et al., 2008] showed also that this process is self-sustained and leads to a substructure of the electron bunch. This substructure are longitudinal microbunches with a distance of λ_{ph} to each other. The electrons in a microbunch emit coherent light and its power is proportional to N_e^2. A detailed description of the self-modulation process is published in [Kondratenko and Saldin, 1980].

However, the principle to generate coherent radiation works only if the electron bunch gets density modulated, which is usually realized with an electromagnetic wave. Assumed a seed is present, the phase space motion of the electrons within an electromagnetic field can be described by the pendulum equations, i.e the time derivative of an electron's ponderomotive phase and the change of the relative energy deviation. In addition, the inhomogeneous wave equation for the electric field of the light wave and the evolution of a microbunch structure coupled with longitudinal space charge forces can be described mathematically. These equations can be solved analytically only for some simple cases e.g. assuming a homogeneous charge density and very long electron bunches as well as neglecting the betatron oscillations and the diffraction of the EM-wave. However in most of the cases of practical interest numerical simulations have to be used. For the simulation different tools like GENISIS [Reiche, 1999], GINGER [Fawley, 2004], and FAST [Saldin et al., 1999a] are available. In figure 2.5 a GENISIS simulation of the microbunching process performed by Sven Reiche is shown.

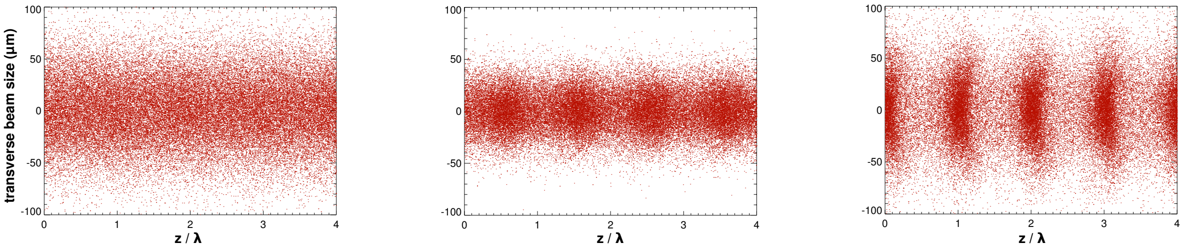

(a)

(b)

(c)

Figure 2.5: GENISIS simulation of the microbunching process. The plots show the development of the microbunch structure with respect to the transverse and longitudinal coordinates in the bunch. The distance of the microbunches is equal to the radiated wavelength. 2.5(a): initial distribution of the electron bunch. 2.5(b): developing microbunch structure. 2.5(c): fully developed microbunch structure at the end of the undulator. (Courtesy of Sven Reiche, PSI)

In order to solve the pendulum equations analytically the following approximations have to be made: the dependence of the bunch charge density as well as the electromagnetic field on the transverse plane is neglected (one-dimensional model). The electron bunch is assumed to be very long, i.e. the effects of the tail and head of the bunch can be neglected. Further, the charge distribution is assumed to be homogeneous and the modulation of the current density is assumed to be small. These assumptions lead to the so-called third-order equation and can be solved analytically.

It is further possible to deduce a number of properties, describing the FEL process. The typical emitted FEL radiation as a function of the undulator length is shown in figure 2.6. During the first few meters the electron bunch has an initial current density. As soon as the electron bunch becomes modulated and the microbunch structure develops the emitted FEL pulse energy increases exponentially. The power of the light wave can be described with the following equation:

$$\begin{aligned} P(z) &\propto \exp(z/L_g) \\ &\text{with} \qquad L_g \propto \left(\tfrac{\lambda_u}{K^2}\right)^{1/3}, \end{aligned}$$

where $P(z)$ is the power of the light wave and L_g is the gain length which increases for lower wavelengths [Schmüser et al., 2008]. After approximately 12 m the microbunch structure is fully developed and saturation sets in. No further amplification of the emitted radiation is possible.

2.4.4 FEL operation modes

In the previous section the FEL-amplification of an electromagnetic wave has been discussed in general. Depending on the origin of the radiation one can distinguish several

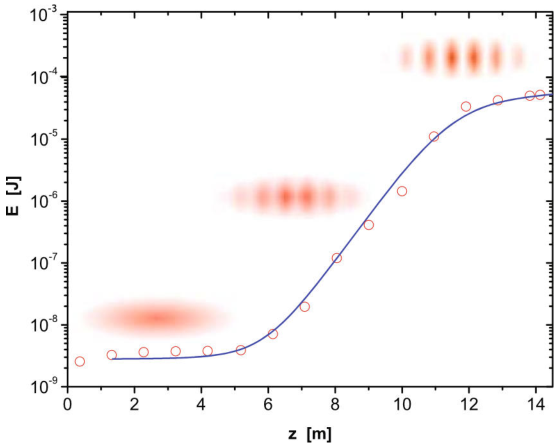

Figure 2.6: The exponential growth of the FEL pulse energy as a function of the length traveled in the undulator. After a few gain lengths the exponential growth and the microbunching starts. The circles correspond to measurements of the TESLA Test Facility [Ayvazyan et al., 2002]. The progressing microbunching is indicated schematically. The graphic is taken from [Schmüser et al., 2008] with kind permission of Springer Science and Business Media.

FEL-operation modes, which will be discussed in this chapter.

Self-amplified spontaneous emission (SASE)

The most common operation mode of an FEL is SASE, which has been observed for the first time in the XUV regime at the TESLA test facility in Hamburg at DESY [Andruszkow et al., 2000]. This operation mode does not need an external laser seed, it rather uses the spontaneous undulator radiation as a seed to initiate the amplification process: the electron bunch consists of randomly distributed electrons. This distribution leads to a white noise spectrum within the first part of the undulator. The spectral component which is within the FEL bandwidth will act as the seed for the following amplification process. However, SASE is based on a stochastic process, which leads to fluctuating properties of the FEL radiation on a shot-to-shot basis. The spectrum and the pulse profile is subject to erratic fluctuations. Moreover, the pulse energy and the pulse length varies from shot to shot. Nevertheless, it is possible to describe the resulting radiation in a statistical way. In [Saldin et al., 1998] a detailed study of statistical properties of the radiation from a SASE FEL is given.

Seeding schemes

Different seeding schemes have been proposed, in order to reduce these erratic fluctuations of the FEL radiation. The following is primarily addressed to direct seeding with an external laser although a brief summary of other seeding schemes is given. A general overview has been published in [Galayda et al., 2010; Shaftan et al., 2004].

Direct seeding with an external laser

Seeding an FEL with an external laser has been prosed in [Garzella et al., 2004]. The idea is to initiate the amplification process of a high-gain FEL with an external seed, in order to suppress the erratic fluctuations of the SASE radiation. As explained in chapter 2.3 HHG is a feasible method to generate VUV to XUV radiation with a high degree of temporal and spatial coherence and is therefore an eligible candidate.

Different simulations have been published [Miltchev et al., 2008; McNeil et al., 2007a] showing that seeding with an external laser leads to FEL radiation with improved temporal coherence and spectral brightness. The shot-to-shot stability may clearly be enhanced and the pulse width is determined by the pulse width of the seed. The simulations show further that the amplification process "washes out" the attosecond pulse-train structure of the harmonics and selectively amplifies a specific harmonic, which is determined by the FEL bandwidth. It is necessary to ensure that the seed overlaps with the electron bunch in space, time, wavelength, and polarization in order to initiate the seeding process before the SASE signal develops. Therefore, the seed energy threshold depends on the wavelength [Togashi et al., 2011] and is assumed to be in the nanojoule range for photon energies smaller than 100 eV. Moreover, the amplification process takes place within the pulse length of the seed, hence the arrival time jitter of the electrons caused by the acceleration process has no influence on the yielded FEL radiation as long as the temporal jitter does not exceed the electron bunch length.

So far different seeding experiments have been performed. The first observation of a seeded FEL has been reported at the Deep Ultra-Violet FEL, where the third harmonic from crystals $\lambda_{\text{seed}} = 266$ nm led to a large amplification [DiMauro et al., 2003]. In Japan the SPring-8 Compact SASE Source (SCSS) test accelerator has been seeded with a high-harmonic. Here successful seeding has been reported for $\lambda_{\text{seed}} = 160$ nm and $\lambda_{\text{seed}} = 61.2$ nm [Lambert et al., 2008; Togashi et al., 2011]. At SPARC a seeding experiment is ongoing, where first results have been achieved at $\lambda_{\text{seed}} = 260$ nm [Giannessi et al., 2008; Tcherbakoff et al., 2006] and Max Lab is preparing a seeding experiment as published in [Čutić et al., 2010; Thorin et al., 2007].

It has been shown [Lambert et al., 2008; Togashi et al., 2011] that the intensity of the seeded FEL radiation is enhanced compared to the SASE operation mode, although the ratio between the SASE and seeding associated signal drops down for smaller wavelengths. In addition it has been shown that the spiky structure of the spectrum in case of SASE is drastically reduced by seeding the FEL.

Alternative seeding schemes

High-gain harmonic generation (HGHG) is a different scheme of seeding an FEL [Doyuran et al., 2004; Yu et al., 2000; McNeil et al., 2007b]. In this case, a seed laser modulates the electron bunch in a first undulator (modulator). A following dispersive section transfers the energy modulation into a density modulation and a second undulator (radiator) radiates higher harmonics of the seed laser. In a second step the radiation passes a monochromator and afterwards modulates an unmodulated part of the electron bunch in a second modulator. The electron bunch travels then through another dispersive section and another radiator, which is tuned to higher harmonics. In [Yu et al., 2003; Wang et al., 2006; Čutić et al., 2011] first results have been published. This scheme can also be used to establish a temporal overlap between the electron bunch and the seed laser as published in [Tarkeshian et al., 2010].

Recently, "echo-enabled harmonic generation" has been proposed [Stupakov, 2010; Xiang et al., 2010]. Here a long wavelength laser modulates the electron bunch to a short wavelength microbunching: the electron bunch is modulated by a laser with a wave number k_1 in a first modulator. It travels then trough a dispersive section and is subsequently modulated by a second laser with k_2 in a second modulator. After passing a second dispersive section the echo signal occurs at the wave number $k_E = nk_1 + mk_2$, where n and m are integer numbers [Xiang et al., 2010].

Experimental environment 3

The experimental environment of the sFLASH experiment will be presented within this chapter. At the beginning a rough overview of the FLASH facility is given followed by a closer look on the sFLASH related sections. In a detailed manner the HHG source and its dedicated diagnostics are being presented.

3.1 seeded Free electron LASer in Hamburg (sFLASH)

sFLASH is an experiment at the FLASH facility at DESY, Hamburg. It is a joint venture between the University of Hamburg and DESY (Helmholtz-Gemeinschaft) to further increase the performance of FLASH [1]. After a brief description of the latest status the goal of this experiment is being presented.

Figure 3.1: Free electron LASer Hamburg at DESY (courtesy of S. Schreiber, [DESY, 2011]).

---

[1] The project is supported by BMBF under contract No. 05 ES7GU1.

3.1.1 FLASH facility

Figure 3.1 shows a photograph of the FLASH facility at DESY, Hamburg. FLASH is a free electron laser facility in Hamburg providing highly brilliant VUV, XUV, and soft x-rays to users [Tiedtke et al., 2009; Schneider, 2010].

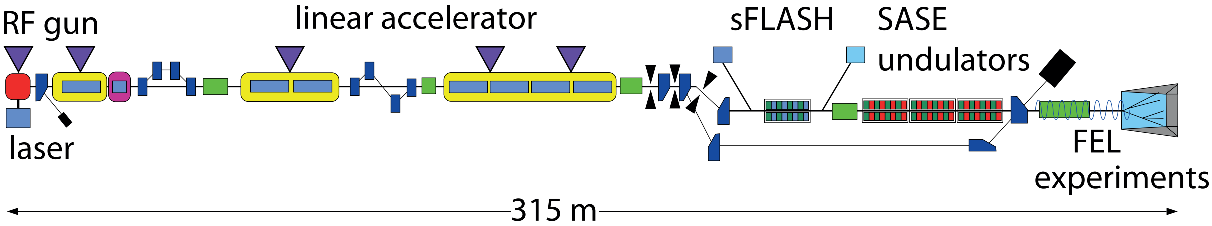

Figure 3.2: Schematic representation of FLASH (courtesy of S. Schreiber, [DESY, 2011])

In figure 3.2 a schematic representation of the FLASH facility is given: the electrons are produced with a laser driven electron gun (1.3 GHz copper cavity, 3.9 MW RF power, Cs_2Te photo cathode, 262 nm [Schreiber, 2011a]) and are subsequently accelerated within the superconducting acceleration modules (seven accelerating modules each with eight 9-cell superconducting cavities operated at 1.3 GHz, [Schneider, 2010; Schreiber, 2011a]) up to a final particle energy of 1.25 GeV [DESY, 2010]. FLASH is operated with a 10 Hz repetition rate of macro-bunches. Each macro-bunch (bunch-train) can consist of up to 800 mirco-bunches. The separation of the electron bunches within a train can be set to $(1, 2, 10, 100)$ µs [Tiedtke et al., 2009]. After the electrons are accelerated they travel through the undulator section (six undulator modules with a fixed gap of 12 mm, permanent NdFeB magnets, peak field $B = 0.48$ T, $K = 1.23$, period $\lambda_u = 27.3$ mm, gain length $L_{gain} = (2.5 \pm 0.3)$ m at 13 nm) in order to produce highly brilliant radiation. The electrons are dumped and the radiation is sent to the FLASH hall for user experiments. So far, the operation mode of FLASH is SASE and the current available fundamental wavelength ranges from 47 nm down to 4.1 nm [Schreiber et al., 2010]. The light pulses are characterized with pulse lengths down to 30 femtoseconds [Frühling et al., 2009; Mitzner et al., 2009] and a peak brilliance of $10^{29} - 10^{30}$ photons s^{-1} $mrad^{-2}$ mm^{-2} 0.1% $bandwidth^{-1}$ [Treusch and Feldhaus, 2010]. At saturation the FEL pulses consist of a decisive transverse TEM_{00} mode and several tens of longitudinal modes [Saldin et al., 1999b, 2010, 2008a,b]. In table 3.1 a summary of the pulse properties at FLASH is given, where the quoted values either correspond to measurements of the pulse-to-pulse statistics or to calculations based on the spectral width. Due to the statistical nature of SASE, intensity fluctuations of the FEL pulses occur. The spectral and the temporal pulse profiles are subject to erratic fluctuations [Ackermann et al., 2007]. Moreover, the electron acceleration process introduces arrival time fluctuations of the electron bunch at the undulator entrance [Löhl, 2009; Schulz et al., 2008], which leads to a temporal jitter with respect to external laser pulses (table 3.1). The origin of this jitter is mainly due to the first acceleration module as well as the bunch compressors (chapter 2.4) and limits the resolution of corresponding pump-probe experiments [Drescher et al., 2010; Maltezopoulos

Table 3.1: Performance of FLASH

property	value	comment/ citation
wavelength	$(47 - 4.1)$ nm	fundamental mode [Tiedtke et al., 2009] [Schreiber et al., 2010]
average pulse energy	$(10 - 300)$ µJ	[Treusch and Feldhaus, 2010] [Schreiber, 2011b]
bandwidth $\Delta\lambda_{ph}/\lambda_{ph}$ (FWHM)	$(0.7 - 1)\%$	[Treusch and Feldhaus, 2010]
pulse duration in general (FWHM)	$(70 - 10)$ fs	derived from statistics/ spectra [Treusch and Feldhaus, 2010]
	$(200 - 10)$fs	use of 3^{rd} harmonic module [Schreiber, 2011b]
measured pulse duration (FWHM)	(29 ± 5) fs	at 23.9 nm [Mitzner et al., 2009]
	(35 ± 7) fs	at 13.5 nm [Frühling et al., 2009]
temporal coherence length (FWHM)	12 fs	at 23.9 nm [Mitzner et al., 2008]
	8.1 fs	at 33.2 nm [Schlotter et al., 2010]
peak power	$1 - 5$ GW	[Treusch and Feldhaus, 2010]
peak spectral brilliance	$10^{29} - 10^{30}$	photons s^{-1} $mrad^{-2}$ mm^{-2} 0.1% $bandwidth^{-1}$ [Robinson et al., 2010]
intensity jitter (rms)	18%	[Ackermann et al., 2007]
timing jitter (rms)	≈ 80 fs	[Schreiber, 2011b]

et al., 2008; Azima et al., 2007]. These shot-to-shot fluctuations can be measured with a x-ray / laser cross-correlator and reduce the temporal resolution to the pulse duration of the optical laser [Krikunova et al., 2009].

The timing jitter of the electron bunch is reduced by enabling beam based feedback systems [Koprek et al., 2010]. In addition, an optical synchronization system is employed [Schulz, 2011], as well as an LLRF (Low Level Radio Frequency) upgrade of the Linac, which is able to reduce the arrival time jitter to ≤ 80 fs [Schreiber, 2011b]. In contrast the spectral and intensity fluctuations are due to the statistical nature of SASE and cannot be reduced any further. As explained in chapter 2.4.4 seeding an FEL is a promising way to overcome all stated limitations.

3.1.2 sFLASH

During a shutdown from September 2009 to February 2010 the sFLASH section has been installed. Here in addition to the existing facility variable gap undulators, as well as dedicated diagnostics and two experimental containers have been built up in order to seed FLASH with an external laser. To this end, XUV seed pulses from a HHG source will be overlapped in space and time with the electron bunches. In this case the amplification process takes place within the seed pulse length leading to a radiation without temporal jitter, lower intensity- and spectral fluctuations, and full control over the pulse length (chapter 2.4.4). This seeding scheme will be explained in detail within this chapter and is illustrated in figure 3.3.

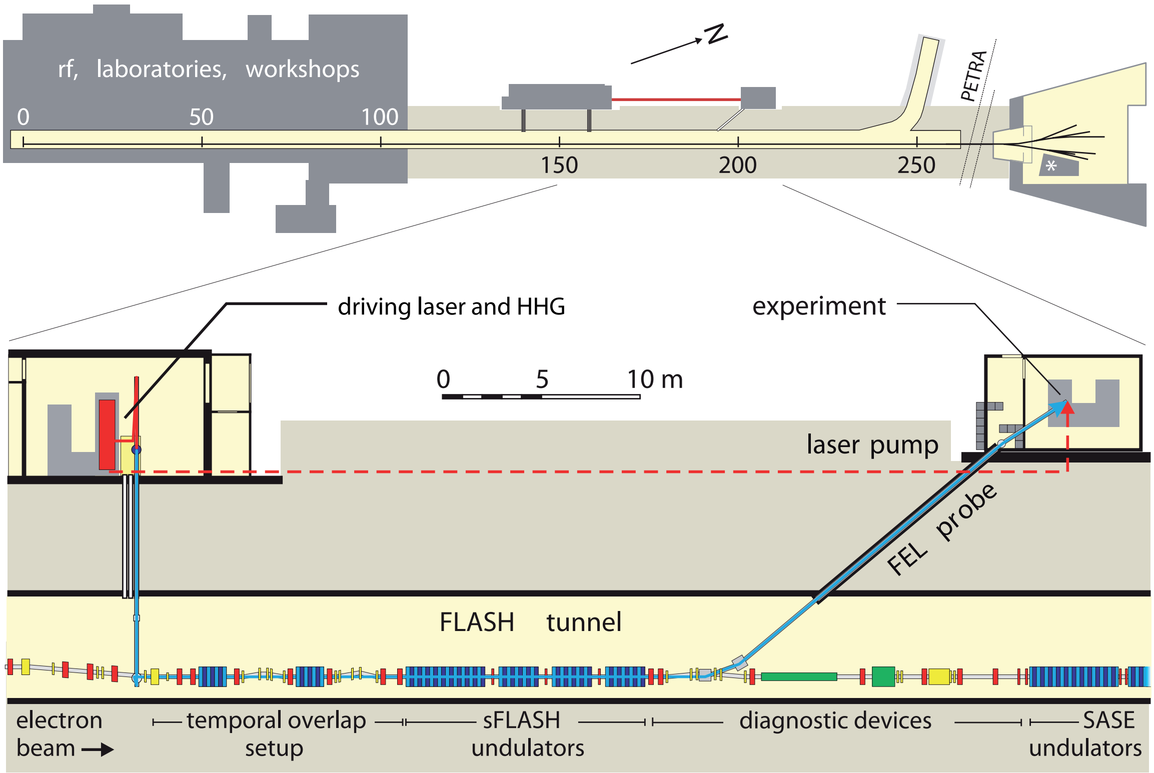

Figure 3.3: Schematic sketch of the sFLASH experiment. (Courtesy of S.Khan, DELTA, Technische Universität Dortmund)

The illustration shows the whole FLASH facility within the upper part, where the electrons are generated at position 0 m and travel in direction of the FLASH experimental hall on the right hand side. The lower part of the picture corresponds to a more detailed representation of the sFLASH section between position 150 m and 200 m. Here the laser-lab for HHG, the sFLASH part of the FLASH tunnel, and the experimental container are shown schematically. In addition two photon beamlines are drawn in red and blue. The blue line corresponds to the seed and the seeded XUV radiation. In a first stage the 21st harmonic of an 800 nm driving laser is used to seed FLASH. In parallel a seeding option of the 61^{st} harmonic (13 nm) has been prepared. The red line corresponds to a fraction of the 800 nm driving laser, which is transfered to the experimental hutch of the sFLASH section [Rehders, 2011] for first timing experiments.

The following will describe the sFLASH related sections, i.e. the laser system, the harmonic source, the injection beamline, the undulator section, the sFLASH diagnostics, and the experimental hutch. The laser system, the harmonic source, and the corresponding characterization is the main part of this phd thesis. Also contributions to the development of XUV diagnostics within the injection beamline have been performed and are described in chapter 3.2 and chapter 4. The injection beamline in general, i.e. the transport of the XUV seed to the electron vacuum is described in [Bödewadt, 2011]. The FEL associated works, i.e. the characterization of the undulators [Tischer et al., 2010; Delsim-Hashemi et al., 2009], the six dimensional overlap of the XUV seed and the electron bunches [Bödewadt, 2011; Tarkeshian, 2011], simulations regarding the seeding process [Bödewadt, 2011; Tarkeshian, 2011; Miltchev et al., 2008], and the diagnostics for the seeded FEL radiation [Curbis et al., 2010, 2009] are mainly described in [Bödewadt, 2011; Tarkeshian, 2011].

Laser laboratory

The HHG section is located at position 150 m adjacent to the FLASH tunnel. Here the driving laser and its diagnostics are set up. Furthermore, the generation and characterization of high-order harmonics is being performed. Because the HHG source and its diagnostics is the main part of this thesis, a thorough description of the system is given separately in chapter 3.2 and chapter 4.

Injection beamline

The in-coupling section transfers the seed to the electron vacuum. After approximately eight meters an UHV chamber with a 13.9° grazing incidence mirror has been installed to deflect the XUV radiation to the level of the electron beam as shown in figure 3.4. In addition a XUV photodiode has been set up in order to measure absolute photon energies of the XUV radiation. In this case the radiation has not yet passed any XUV optic, hence no uncertainties regarding the reflectivity of the mirrors is transfered to the deduction of the XUV pulse energy. However, in order to overlap the electron bunch with an increased XUV seed flux, the XUV radiation needs to be focused into the undulator section (chapter 2.4.4). For this reason a second chamber has been installed. Here the XUV radiation is focused in terms of a normal incidence XUV multilayer in combination with three 14.1° grazing incidence mirrors which maximize the total reflectivity. The multilayer mirrors are mounted on a remote controlled wheel in order to choose a focal length and a coating for the different wavelengths. The wheel is equipped with ScSi and MoSi normal incidence multilayer mirrors with a focal length of $f = (6.25, 7.00, 8.50)$ m. Besides, also all the grazing incidence mirrors can be changed remote controlled to either B_4C or MoB_4C in order to steer the 21^{st} or the 61^{st} harmonic, respectively. A detailed description of the injection beamline can be found in [Bödewadt et al., 2010; Bödewadt, 2011].

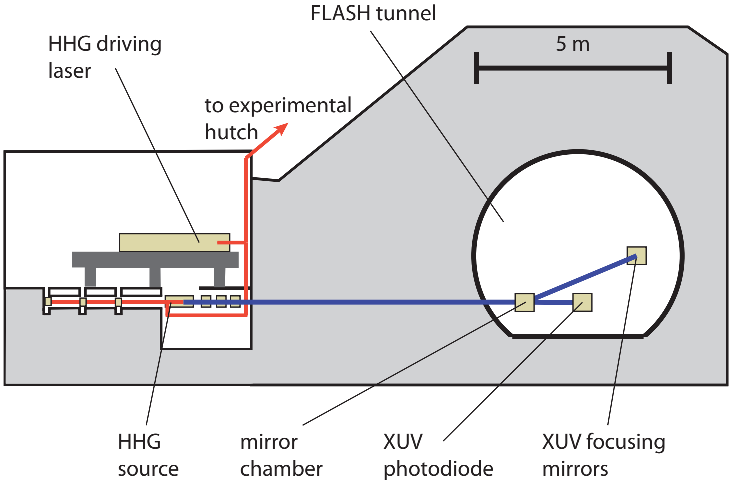

Figure 3.4: Cross section of the FLASH tunnel and the adjacent laser laboratory. The HHG source is located in a pit under the floor of the laboratory. The NIR driving laser is drawn in red and the XUV seed in blue.

Undulator section

The undulator section consists of three 2 m (PETRA III type, 31.4 mm period, $B = 1$ T) and one 4 m long (PETRA II type, 33 mm period, $B = 1.07$ T) variable gap undulator [Delsim-Hashemi et al., 2009], where the vacuum chamber within the undulators is based on XFEL developments [Altarelli et al., 2006; Tischer et al., 2010]. The 700 mm long intersections between the undulators contain a quadrupole magnet, a phase shifter, and diagnostic devices to achieve a transverse overlap, which is mandatory for the amplification process [Miltchev et al., 2008]. In addition two ORS (Optical Replica Synthesizer) undulators [Khan et al., 2008] are within the sFLASH section, which can be used to realize a temporal overlap of the seed and the electron bunch [Tarkeshian et al., 2010].

Overlap and diagnostics

Seeding requires a stable six dimensional overlap $\{x, y, x', y', t, \lambda\}$ between the seed and the electron bunch as explained in chapter 2.4.4. To achieve and to control the seeding process a number of diagnostic devices have been set up inside the accelerator tunnel. For the transverse overlap eight beam position monitors [Baboi et al., 2007], eight optical transition radiation screens [Bödewadt et al., 2010; Honkavaara et al., 2003], and four wire scanner [Hass et al., 2011] are in use. The temporal overlap is achieved by measuring simultaneously the undulator radiation and the residual 800 nm driving laser [Tarkeshian et al., 2010]. A coarse overlap in the nanoseconds regime is achieved with a photo multiplier or a photo diode. Then a streak camera is used to adjust the timing on a picosecond timescale (0.6 ps). For a more accurate overlap the existing ORS undulator system can be used [Khan et al., 2008]. Here the residual 800 nm driving laser is focused into the first undulator (modulator) and produces an energy modulation of the electron bunch. The second undulator (radiator), which is tuned to the fundamental or second harmonic of the driving laser emits coherent radiation as soon as the temporal overlap is achieved. In addition the oscillator of the driving laser is locked to the optical synchronization system using a two-color optical cross-correlator [Schulz et al., 2008]. Moreover, a feedback system to stabilize the temporal drift of the laser amplifier has been developed [Rehders, 2011]. Once the temporal overlap is established, the feedback system is enabled to retain the temporal overlap regardless of the temporal drift of the amplifier. A detailed description of the temporal overlap can be found in [Tarkeshian et al., 2010]. For the overlap of the wavelength, i.e. matching of the undulator radiation to the wavelength of the seed, a spectrometer has been installed in the FLASH tunnel. The gaps of the undulators are successively tuned until the spontaneous radiation equals the wavelength of the seed [Curbis et al., 2010]. In order to measure and to evaluate the seeding signal an intensity monitor with three MCPs (Multi-Channel Plate) and a gold mesh is available [Curbis et al., 2009]. The concept is adopted from [Bittner et al., 2007] and works as follows: the FEL radiation is scattered at the gold mesh and the three calibrated MCPs measure the corresponding signal. The device is capable to measure six to seven orders of magnitude in photon flux, thus it is possible to sample the gain curve of the seeding process.

Experimental hutch and external beamline

At last, an experimental container has been built up next to the FLASH tunnel at position 200 m in figure 3.3. On the one hand a photon beamline from the tunnel to the container has been set up, in order to further characterize the seeded radiation. A XUV autocorrelator for instance could be installed to characterize the timing structure of the XUV pulse. On the other hand a fraction of the driving laser is separated within the laser lab and is sent directly to the experimental container. This enables the possibility to perform two-color pump-probe experiments with laser pulses originating from the same source. Hence, the timing jitter is absent which can be measured with an XUV / NIR cross-correlaor [Maltezopoulos et al., 2008].

Parallel operation

sFLASH is supposed to work in parallel to the SASE operation without constraining the users in the experimental hall. Since the SASE undulators, which are located after the sFLASH section have a fixed gap, the radiating wavelength depends only on the energy of the electrons. In contrast, the wavelength of the sFLASH undulators can be adjusted by tuning the electron energy and the gap. In [Miltchev et al., 2009] a simulation is presented, showing that for a seed of $\lambda_{\text{seed}} = 38$ nm sFLASH is able to run in parallel to SASE as long as $10\text{ nm} \leq \lambda_{\text{SASE}} \leq 46$ nm. 70% of the requested wavelengths in 2010/2011 match the requirements, hence in principle a parasitic seeding mode is possible [DESY, 2011].

3.2 High Harmonic Generation

This chapter is addressed to the HHG setup. The laser system as well as the HHG source and its diagnostics will be explained in detail. Especially the boundary conditions, which limit the freedom of construction are elucidated.

3.2.1 The laser system

For HHG an intense laser pulse is needed. This section summarizes the laser system used for sFLASH. In figure 3.5 a schematic sketch of the laser system is shown. It consists of a laser oscillator [Menzel, 2001; Rulliere, 1998] and an amplifier, which is based on chirped pulse amplification (CPA) [Strickland and Mourou, 1985; Svelto, 1982]. The laser oscillator itself consists of a CW Coherent Verdi (532 nm), pumping a passive self focusing mode-locked oscillator [Chen and Wang, 1991; Brabec et al., 1992] (FEMTOSOURCE compact oscillator, 80 MHz, 4.2 nJ) [Spielmann et al., 1994]. It produces a single TEM00 mode with a bandwidth of 56 nm at a central wavelength of 800 nm. In order to compensate drifts of the oscillator, a phase lock loop (PLL) is employed to adjust the cavity, i.e. the time of circulation. Here pulse to pulse drifts are being recognized to actuate the PLL and to circumvent those drifts [Kroupa, 2003; Best, 2003]. The following CPA system

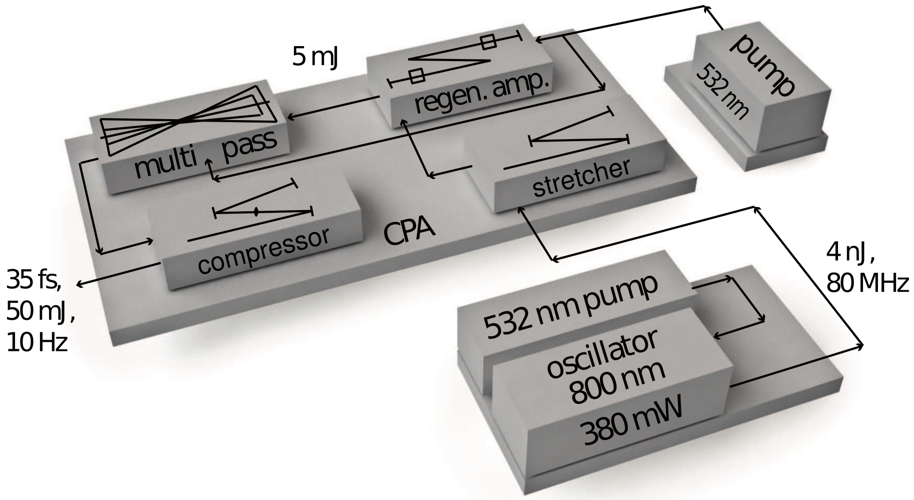

Figure 3.5: Schematic sketch of the laser system, which consist of a laser oscillator and a chirped pulse amplifier.

(Hidra, Coherent) first stretches the laser pulses to approximately 400 ps with reflecting gratings [Palmer and Loewen, 2005] and then amplifies them with a regenerative- [Murray and Lowdermilk, 1980] and a multipass amplifier [Lowdermilk and Murray, 1980]. In both cases a titanium sapphire Ti^{3+}:Al_2O_3 crystal is pumped with a Nd:YAG laser (InnoLas Spitlight 600) operating at a central wavelength of 532 nm, a pulse energy of 800 mJ, and 7 ns pulse length. The regenerative amplifier is characterized with a bandwidth of 45 nm and has an output of 5 mJ at a specified central wavelength of 790 nm. The employed Pockel cells release ten pulses per second, which are subsequently amplified within five roundtrips through the multipass amplifier to approximately 48 mJ at a central wavelength of approximately 810 nm. At last those pulses need to be re-compressed in order to achieve high intensities for HHG.

For the re-compression a standard reflecting grating compressor and an additional transmissive grating compressor are used. Due to the fact, that high energy ultra short laser pulses do interact with air and this nonlinear interaction [Shen, 1984] destroys the temporal profile of those laser pulses an additional transmissive UHV grating compressor has been designed. To this end, the reflective compressor is used to pre-compress the laser pulses to a few hundred femtoseconds. Additionally, the laser beam is expanded with a telescope and is then transported approximately 7 m in air to the HHG vacuum system. Eventually, the laser pulses are compressed by the transmissive grating compressor to final 33 fs. A transportation of the pre-compressed laser without expanding the beam waist also introduced filamentation [Kasparian and Wolf, 2008] and inhibited efficient HHG. An alternative to the realized two compressor setup would be to set up the reflective grating compressor within the vacuum system. Due to the lack of space (following chapter) this option would reduce the flexibility of further developments, hence it has not been followed so far. The transmissive grating compressor is without prior pre-compression not able to reduce the pulse length down to 33 fs, thus the only option is the two compressor setup.

As already mentioned a fraction of about 5% of the uncompressed laser is send through an external beamline to the sFLASH related experimental hutch. Here a third compressor reduces the pulse width of the 800 nm driving laser to approximately 33 fs [Rehders, 2011]. In combination with the seeded FEL radiation time dependent experiments, as for instance two-color pump-probe experiments are possible without the lack of a timing jitter.

3.2.2 High harmonic generation source

This section is directed to the HHG seeding source, which is designed and constructed in the framework of this thesis. Due to radiation concerns associated to the direct connection between FLASH and the HHG source, the source has been set up in an approximately 2 m x 1.5 m x 1.1 m pit below the floor of the laser lab which leads to severe boundary conditions for the nominal size of the source. It will be shown that this limited degree of freedom leads to limitations of the harmonic source. In figure 3.6 a CAD model of the HHG source and the pit is shown. In addition to the pit one horizontal and three vertical holes have been drilled to extend the possible focus geometries for HHG. Those boreholes have a diameter of 250 mm and are abbreviated as trunks within the following

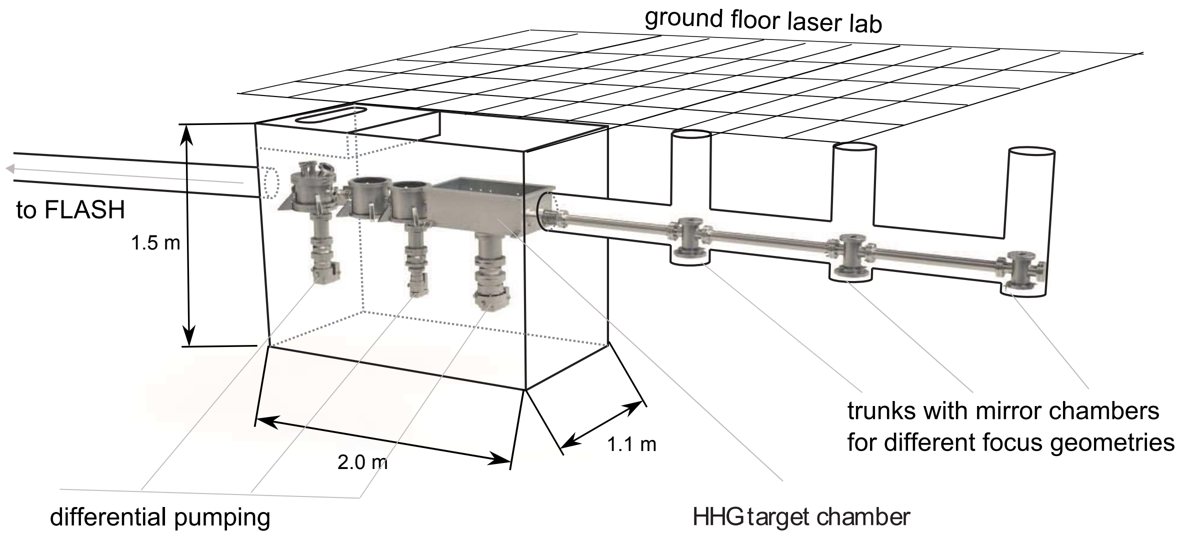

Figure 3.6: CAD model of the HHG source in the pit. The pit is drawn schematically and is located underneath the ground floor of the HHG laser lab. Three turbo pumps are mounted below the vacuum chambers. The three trunks contain a mirror chamber to realize different focus geometries for HHG. A picture of the pit is shown in the appendix (figure D.1).

work. The distance of the first trunk to the pit, as well as the distance between two trunks are chosen to be one meter, in order to realize different loose focusing geometries of $f = (1.5, 2.5, 3.0, 3.5, 5.0,$ and $7.0)$ m for HHG.

In addition to the inconvenient pit, a HHG source needs to be set up in vacuum, because XUV radiation is absorbed in air [Jaeglé, 2006]. Furthermore, the seeding source is connected to the electron vacuum, which has high requirements. As a consequence, the HHG source for sFLASH has higher vacuum requirements compared to ordinary HHG sources. In order to ensure stable vacuum conditions the gas load of the harmonic target has to be reduced as much as possible. On the other hand differential pumping has to be employed. To guarantee a pressure of 10^{-8} mbar at the entrance of the injection beamline while the HHG target chamber is operated with a pressure up to 10^{-3} mbar a simulation of the vacuum system has been programmed. The program itself calculates the pressure at the beginning of the injection beamline for a pressure of 10^{-3} mbar within the HHG target chamber and is based on basic vacuum physics [Jousten, 2006]. The variables within this code are the pumping power of each differential pumping stage and the diameter of the apertures in between the pumping stages. It turned out that for a 500 l/s turbo pump underneath the target chamber, a 300 l/s and 70 l/s turbo pump underneath the second and third pumping stage, respectively can ensure a pressure of 10^{-8} mbar at the entrance of the injection beamline for corresponding iris diameters of $d_1 = 2$ mm between the first and second, $d_2 = 5$ mm between the second and third differential pumping stage, and $d_3 = 10$ mm between the last differential pumping stage and the injection beamline. The simulation accounts for reduced effective pumping, due to the socket and breadboard between the pump and the chambers. It further covers argon and neon as the noble gas of choice for HHG. It does not account for any sorption or leakage, but this is negligible in practise. A second consequence of the fact that a HHG source has to be set up in vacuum, although it is just a technical issue: all opto-mechanics are necessarily remote controlled. Note, the pressure within the HHG target chamber is not equivalent to the HHG target pressure, nor to the HHG backing pressure of the gas valve.

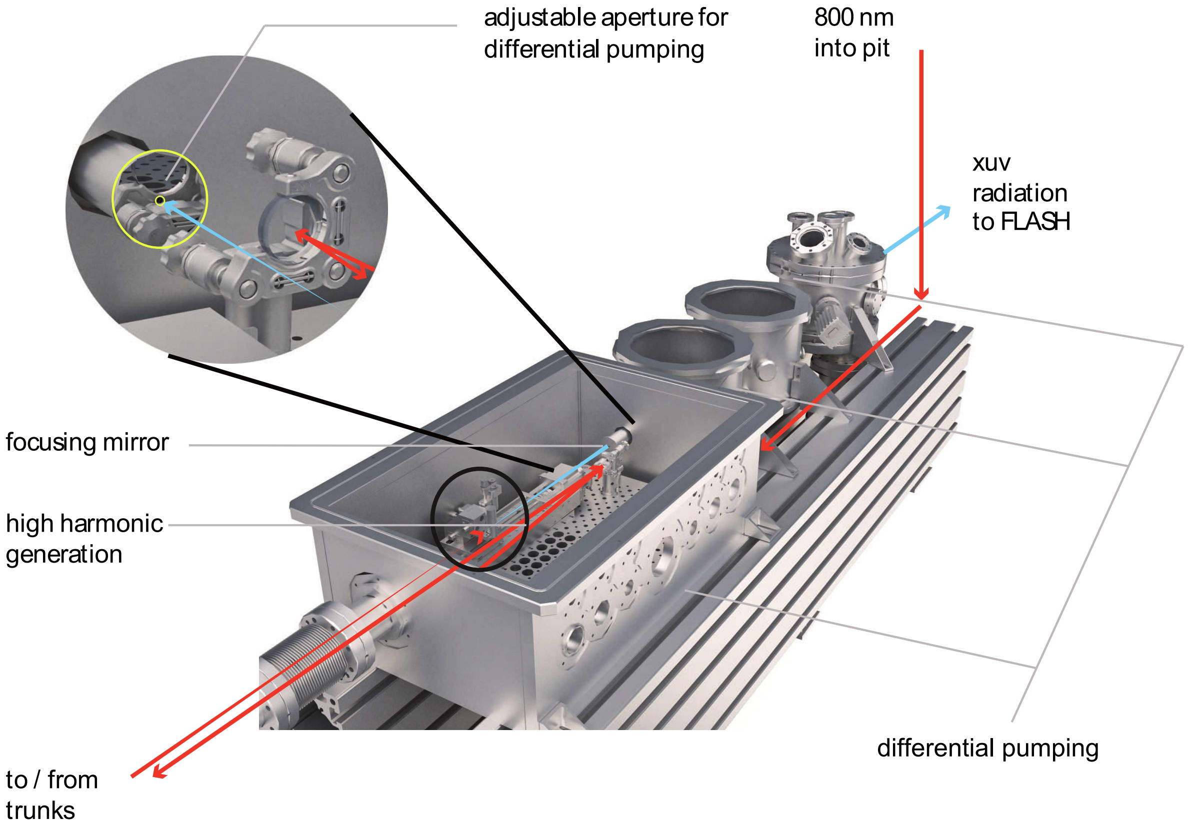

Figure 3.7: Rendered CAD model of the HHG source. The first chamber is the target chamber used for HHG. The second and third chamber (second differential pumping stage) is used for diagnostics, and the last chamber (third differential pumping stage) can be used to steer the XUV radiation to further diagnostics. All differential pumping stages are separated with an adjustable aperture as shown in the upper left corner.

In figure 3.7 a more detailed CAD model of the HHG source is displayed. The first stage is used for the conversion of the driving laser to XUV radiation. The second stage is used for an on-line diagnostic device of the XUV radiation. Within the third stage a movable mirror is set up which can be used to send the XUV radiation either to FLASH or out of the pit and back to the optical table for further diagnostics. The diagnostics of the HHG source will be explained in chapter 3.3. In case the mirror is moved out of the laser beam, the XUV radiation is send to the injection beamline. To ensure the high vacuum conditions of FLASH different valves separate differential pumping stages. Every unexpected vacuum event is detected by the pressure gauges and force the valves to close.

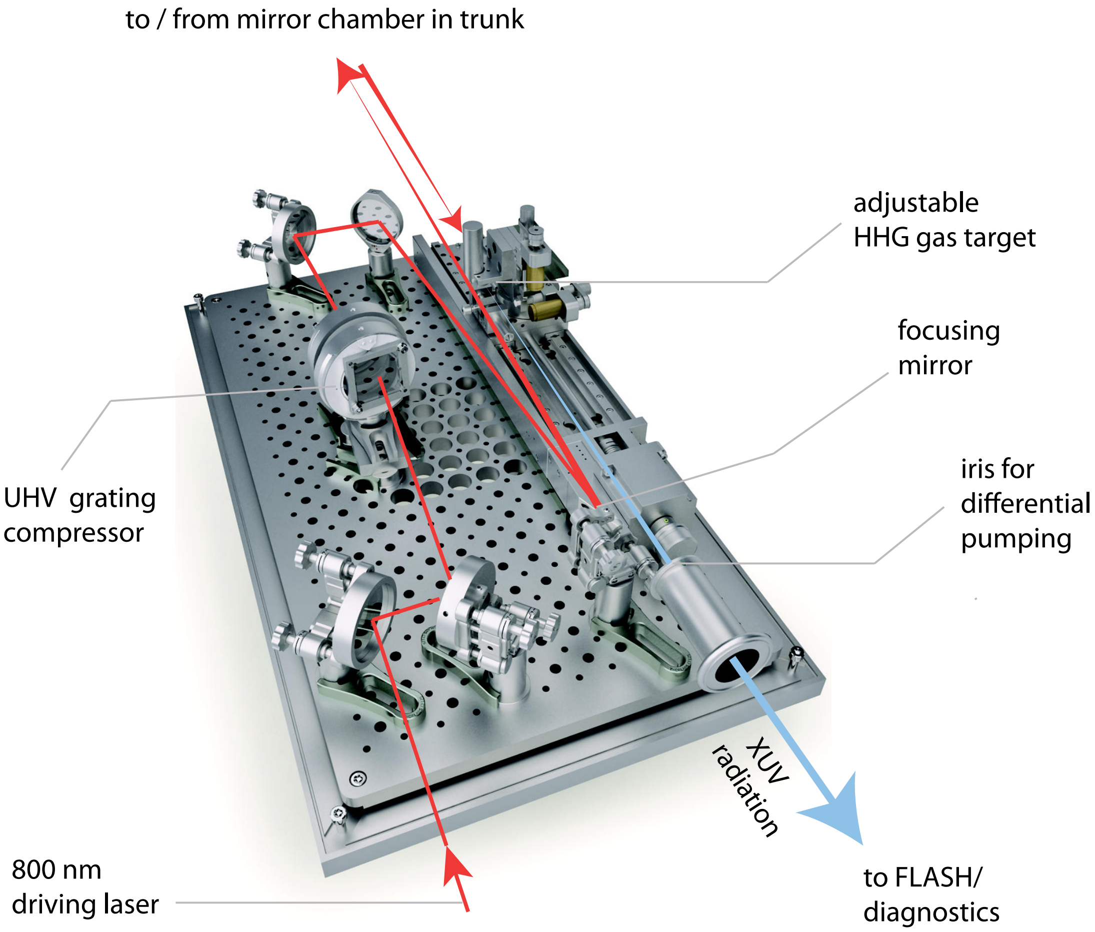

Figure 3.8: Rendered CAD model of the optical setup for HHG in the target chamber: the driving laser enters the vacuum and passes the UHV compressor. Then it is focused into the gas target and high harmonics are generated. At last, the XUV radiation travels to FLASH or to the diagnostics.

Figure 3.8 shows a rendered CAD model of the optical setup in the constructed target chamber. It further shows the beamline of the driving laser: after entering the vacuum chamber the driving laser passes the UHV compressor in order to compress the pulse width down to approximately 33 fs. Then the driver is focused down into the gas target. As mentioned before only a few loose focusing geometries can be set up: the trunks, i.e. the mirror chambers of each trunk have a distance of approximately 1.5, 2.5, and 3.5 meters to the center of the translation stage in figure 3.8. As a consequence only a focusing mirror with a focal length of 1.5, 2.5, or 3.5 meters can be installed in the mirror chamber of the trunk, respectively. For a larger focal length of 3.0, 5.0, or 7.0 meters the focusing optic has to be installed in the target chamber. However, the driving laser hits the optic with a small angle to its normal, thus an astigmatic focus is expected [Hecht and Zajac, 1997; Frank L. Pedrotti, 1987].

High harmonic generation target

During this work different gas targets have been employed. Due to the high vacuum requirements and the low repetition rate of the driving laser (10 Hz) a pulsed gas valve as introduced in [Flettner et al., 2001] was the starting point. In case the gas load exceeds a certain threshold within the last vacuum chamber in front of the injection beamline a fast shutter closes, in order to keep the electron vacuum of FLASH unspoiled. In addition to this free-propagating gas valve different pulsed gas targets have been used to enhance the CE. The interaction length has been increased by means of a longer gas target. The mechanical workshop manufactured channels with a rectangular shape in different widths and lengths, which can be attached to the gas valve. During this work those channels are abbreviated with the following notation "*length x width*", where *width* corresponds to the edge length of the square profile perpendicular to the laser path and where *length* corresponds to the size of the channel in laser direction. During this work a lot of targets have been testet. Only a selection of those targets gained significance and will be presented in chapter 4. Regardless of the specific geometry, the target is mounted on three translation stages plus an additional rotation stage in order to align the target to the laser path. This alignment is crucial for the optimization procedure of HHG and has to be done on a daily basis.

In [Pirri et al., 2008] different geometries have been evaluated. It is shown that the CE can be increased with an array of holes in a gas-filled metal tube and that the effect can be attributed to quasi phase matching (QPM). Within this work the most promising target of [Pirri et al., 2008] has been manufactured and tested. Here the target is abbreviated as *QPM channel*.

At last, a preliminary QPM target developed by Willner et al. has been tested [Willner, 2011]. In figure 3.9 the changed setup is illustrated. It is shown that the beam path of the driving laser has to be changed. On the one hand the focusing optic ($f = 3$ m) has to be placed at a different position in order to remain the focus at the center of the translation stage. In this case the mirror in front of the translation stage was cut in order to let the driving laser pass to the gas target. This different position causes an increased astigmatism of the focus, due to the larger angle of the driving laser relative to the normal of the focusing mirror. On the other hand this assembly leads to an astigmatism free focus in case the focusing mirror is located in a trunk. The focussing optic is then reflected with an angle around zero degree relative to its normal, thus the astigmatism does not occur.

In order to employ two-color HHG a BBO (Beta Barium Borate) crystal is placed close to the focus of the driving laser. Independent of the specific target geometry the

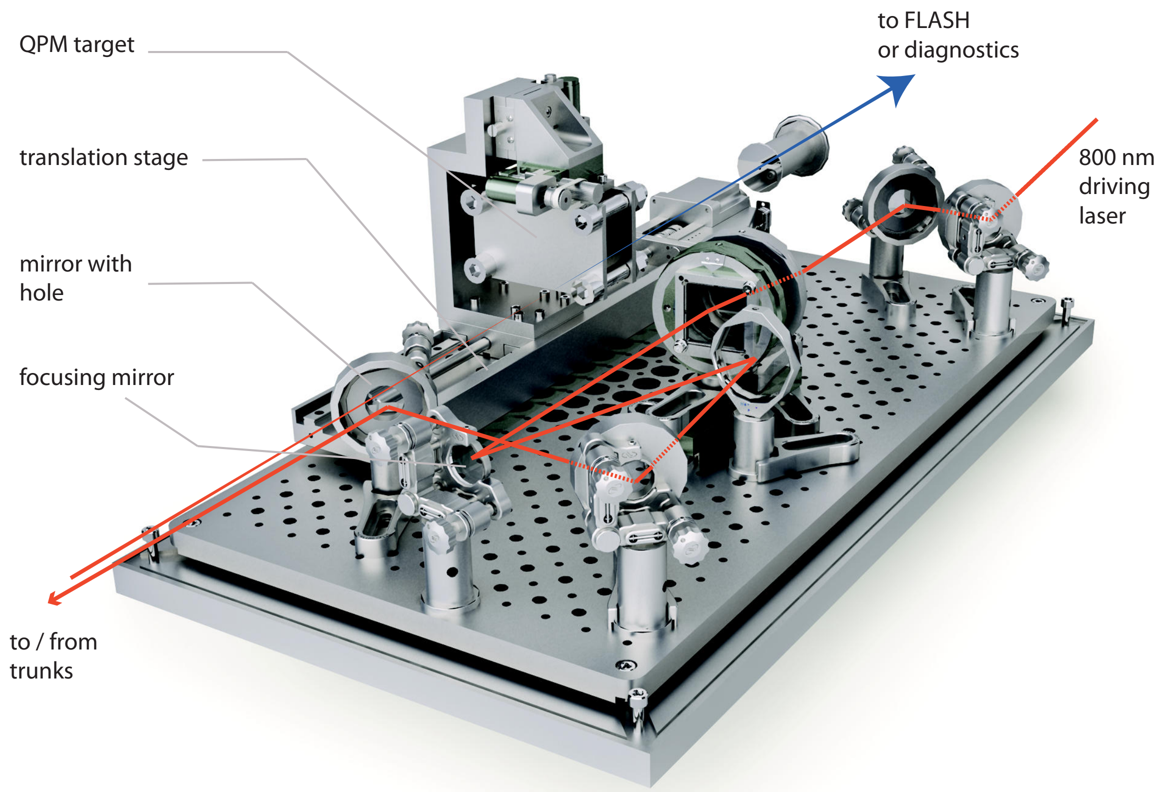

Figure 3.9: Rendered CAD model of the optical setup in the HHG target chamber: in comparison to figure 3.8 the target is exchanged to the QPM target. Additionally the focusing optic is located at a different position and the driving laser is folded several times in order to remain the focus at the center of the translation stage.

possible BBO position is limited. During this work, the BBO has been set up between the "mirror with hole" and the translation stage of figure 3.9. Note that the polarization of the second harmonic is rotated by 90° relative to the fundamental wavelength. This has to be compensated by a wave plate in order to remain the polarization unchanged in the undulator section. During this work only preliminary tests of two-color HHG and QPM HHG have been carried out. The tight schedule of FLASH and the corresponding sFLASH shifts have restricted the developments. It was necessary to ensure a safely operating HHG source during the dedicated seeding shifts, hence a further development of the source in terms of two-color HHG as well as QPM was not possible so far.

3.3 Diagnostics

This chapter is addressed to the diagnostics of the high harmonics and the driving laser. The devices used for the optimization and subsequent characterization are presented.

3.3.1 Characterization of the driving laser

For the optimization and characterization of the driving laser a number of commercially available devices have been employed. The near- and far- field beam profile of the driving laser is measured parasitically after the pre-compressor. In addition, the focus of the driving laser at the gas valve has been optimized by tuning the UHV compressor. Therefore, the gas target has to be removed and a CCD (Charged-Coupled Device) camera has to be placed in to the focus. Thus, the optimization of the focus of the fundamental laser cannot be done parasitically. For the measurement of the wavefront and the aberration errors a commercial Schack-Hartmann sensor has been used at different positions of the beamline. The temporal profile of the laser pulse can be measured with a commercial Grenouille FROG (Frequency-Resolved Optical Gating), as well as a cross correlator, which has been constructed in the framework of a diploma thesis [Schulz, 2010]. At last, a photodiode has been employed in order to measure the timing of the laser relative to the gas valve. Technical details associated to the mentioned devices can be found in appendix C.

3.3.2 XUV optics

For the characterization of the XUV radiation a diagnostic branch has been built up next to the pit and on the optical table of the driving laser. As mentioned before a movable triplet mirror has been implemented within the last chamber in front of the injection beamline, in order to steer the radiation to the diagnostic section. The mirror or rather all mirrors between the generation of XUV radiation and the corresponding diagnostic device have to be chosen explicitly to the wavelength range of the investigated harmonics. During this work the aim of the diagnostic branch is to characterize the 21st harmonic of the 800 nm driving laser, i.e. 38 nm or 32 eV. In order to maximize the transmission the number of mirrors has to be reduced as much as possible and the reflectivity of each mirror has to be as high as possible for the 21st harmonic. In addition, the first XUV mirror is approximately 1.5 m after the focus of the driving laser. Hence, due to loose focusing HHG the material needs to survive high laser intensities. Note that the damage threshold depends on the material and its environment, i.e. the gas and the gas pressure [Nguyen et al., 2011]. However, depending on the angle of the aimed reflection either grazing incidence or multilayer mirrors can be employed [Jaeglé, 2006]. For a reflection of 90 degree we decided to use three consecutive B_4C grazing incidence mirrors. The high reflectivity of the 21st harmonic and the high damage threshold led to this decision.

In figure 3.10 the reflectivity of one B_4C mirror is plotted for a varying photon energy and a varying angle. The measured reflectivity fits to the expected values and is almost constant for photon energies around 32 eV and a fixed angle of incidence ($\vartheta = 15°$),

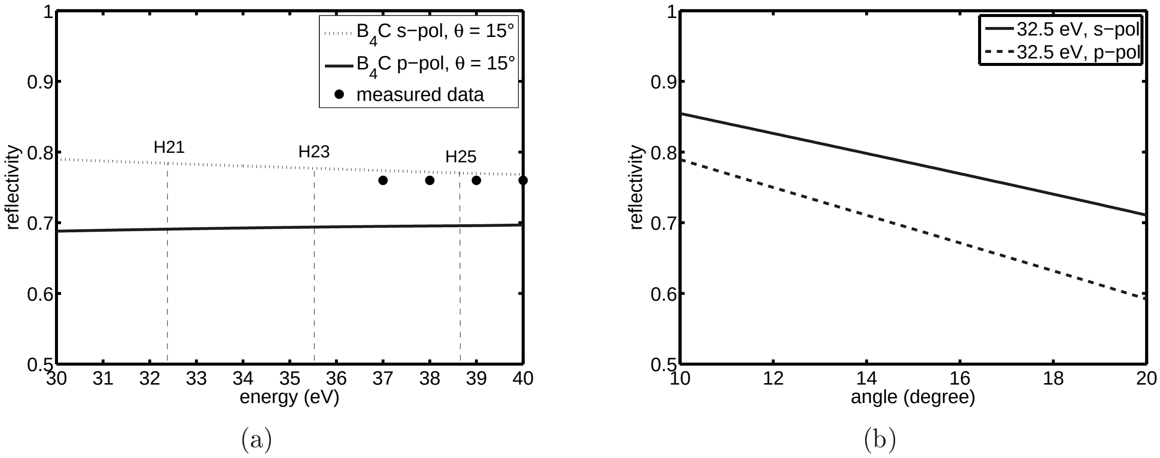

(a)

(b)

Figure 3.10: Reflectivity of B$_4$C for p- and s- polarized light. The dots in figure 3.10(a) correspond to measurements of the PTB [Physikalisch-Technische Bundesanstalt, 2011] with s-polarized light, whereas the remaining data is taken from [Lawrence Berkeley National Laboratory, 2011]. Figure 3.10(a) shows the reflectivity dependent on the photon energy and figure 3.10(b) shows the angle dependent reflectivity.

although the range is limited to values greater than 30 eV. A more comprehensive data set is unfortunately not available. In contrast to the dependence on the photon energy, the reflectivity drops down much faster for a varying angle of incidence as plotted in figure 3.10(b). Therefore, the reflectivity of B$_4$C is assumed to be $(78 \pm 5)\%$ for s-polarized and $(69 \pm 5)\%$ for p-polarized light in case of the 21$^{\text{st}}$ harmonic. Note that in case of s-polarized light the total reflectivity of three consecutive 15° B$_4$C grazing incidence mirrors is 47%. In contrast to 20% for one 45° deflecting B$_4$C mirror [Lawrence Berkeley National Laboratory, 2011].

However, the polarization of the harmonics follows the atomic dipole direction, which is directly related to the driving laser polarization [Lewenstein et al., 1994]. For seeding purposes the polarization of the harmonics within the sFLASH-undulators has to be horizontally oriented. In addition the pre-compressor and the UHV compressor of the driving laser is designed for horizontally polarized light. Thus, the polarization of the driving laser is chosen to be horizontally oriented. A detailed investigation of the injection beamline on the polarization is given in [Bödewadt, 2011].

In figure 3.11 a CAD image of the triplet mirror system is shown. The mirror mount is designed to reflect XUV radiation by 90°, i.e. three times 15° grazing incidence angle in order to achieve the highest possible reflectivity. A further boundary condition for the design of the mirror system is the lack of space in the pit or likewise the lack of space within the corresponding vacuum chamber. On the one hand the mirror system has to be placed and adjusted to the XUV laser profile, it further needs the possibility to be moved out of the laser beam, it needs to be adjustable in order to align the XUV radiation to the diagnostic branch, and it needs to fit into a 250 mm x 200 mm sized vacuum chamber,

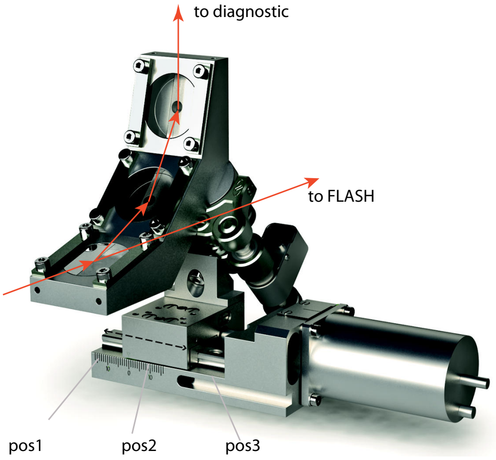

Figure 3.11: Rendered CAD model of the triplet mirror system. The laser radiation is either reflected three times 15° grazing incidence to the diagnostic section or sent to FLASH (position 3). Depending on the desired wavelength two different multilayer coatings are available. Position 1 corresponds to a coating of B_4C and position 2 to Mo for $\lambda_{\text{seed}} = 38$ nm and $\lambda_{\text{seed}} = 13$ nm, respectively.

where 250 mm is the diameter and 200 mm is the height of the chamber. The three mirrors are mechanically adjusted to each other and the whole system can be moved or rotated.

For a reflection of zero degree the highest reflectivity is realized with multilayer mirrors [Jaeglé, 2006]. In figure 3.12 the reflectivity of the used ScSi multilayer is plotted. In contrast to the grazing incidence mirrors, the reflectivity depends strongly on the photon energy: the shape of the curve has a maximum and a steep drop off at approximately 2 eV higher and lower energies. The location of the peak itself depends on the Γ parameter, which corresponds to the thickness ratio between the top layer and the period thickness and is optimized for the 21^{st} harmonic. Unfortunately, the absolute value of the reflectivity varies in different references as shown in figure 3.12: IMD [Windt, 1998] is a software, which calculates the reflectivity depending on the material, angle, photon energy, Γ parameter, and diffusion thickness of the multilayer based on the Henke table. CXRO [Lawrence Berkeley National Laboratory, 2011] provides a web interface also based on the Henke tables to calculate the reflectivity as in IMD. Unfortunately, the absolute reflectivity varies by almost a factor of two. The origin of this uncertainty is unclear. In [Uspenskii et al., 1998] an investigation of ScSi multilayer mirrors is presented. It is shown that for a comparable mirror and wavelength the calculated reflectivity is 71%, in contrast to the measured reflectivity of 40%. Surprisingly those two values match exactly to the values calculated with IMD and CXRO. Nevertheless, the reflectivity of the multilayer is assumed to be $(50 \pm 20)\%$. This uncertainty has a direct impact on the calculation of absolute photon energies and cannot be reduced any further.

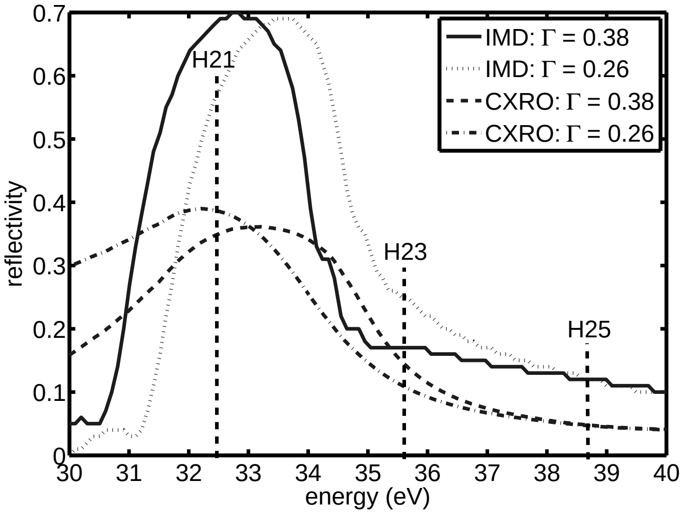

Figure 3.12: Reflectivity of ScSi multilayer calculated with IMD and CXRO

In addition the fundamental laser as well as stray light has to be blocked in order to calculate absolute energies. The following section describes the separation and the resulting uncertainties.

3.3.3 Separation of XUV radiation

Besides the multilayer mirrors, which are a band-pass filter for higher and lower harmonics than H21 as shown in figure 3.12, different metal filters, as well as stray light apertures are employed. In figure 3.13 the transfer beamline to the diagnostic branch including the position of the metal filters and the stray light apertures are illustrated. The stray light apertures have a diameter of 7 mm in order to block stray light of the driving laser. The driving laser has a larger divergence compared to high-order harmonics [He et al., 2009], hence it is possible to spatially block the driving laser as well as low-order harmonics without blocking H21.

The transmission of the employed metal filters is illustrated in figure 3.14. For a photon energy of 15 to 20 eV the transmission through a 200 nm thick aluminum rises from zero to approximately 60%. Then the curve shows a plateau up to 40 eV which corresponds roughly to the 26th harmonic. The transmission of aluminum depends further on the level of oxidation. As shown in figure 3.14(b) the thickness of the Al_2O_3 layer is a crucial parameter. The transmission of H21 is plotted for a variable thickness of the oxide layer. It is shown that for an oxide layer of 10 nm the transmission drops from $\approx$ 60% to $\approx$ 30%. The level of oxidation depends further on the time the filter is exposed to air. Note that some groups [Kim et al., 2005] expect a thickness of $2 \cdot 25$ nm and therefore a lower transmission. In figure 3.14(b) the transmission of 32.5 eV through a 200 nm thick aluminum filter with variable Al_2O_3 thickness is plotted. It is shown that for an overestimation of the oxide layer an error of more than 100% may occur. In [Powell et al., 1990; Campbell et al., 1999; Varjú et al., 2005; Strohmeiner, 1990] investigations

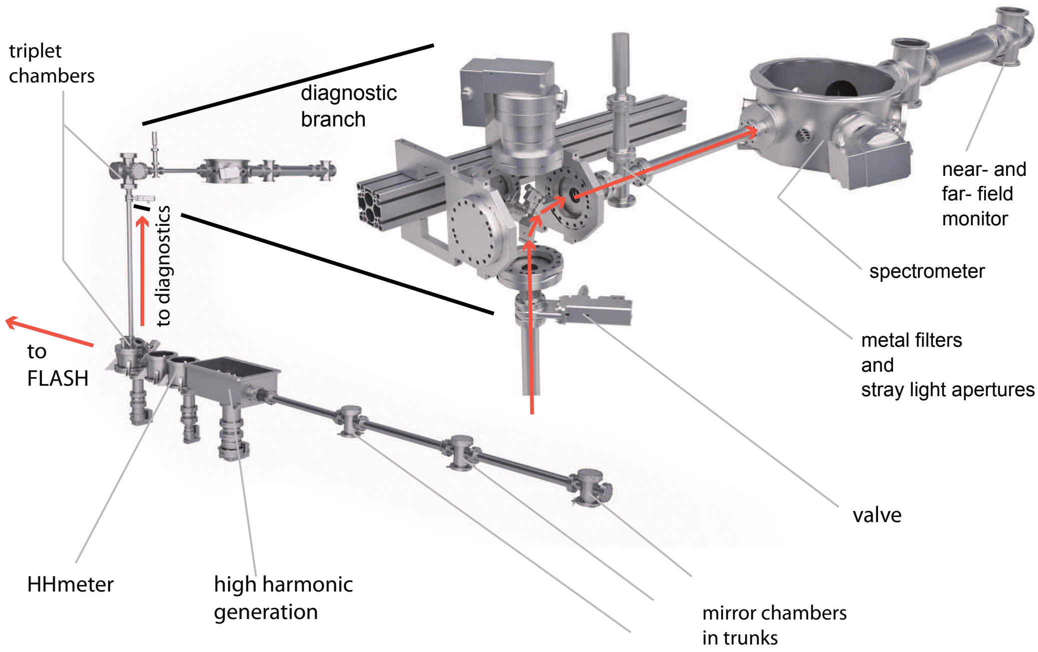

Figure 3.13: Rendered CAD model of the HHG diagnostic. Two triplet mirror systems are employed in order to achieve the highest possible transmission of the XUV radiation.

on aluminum oxide thicknesses have been performed. It turns out that aluminum sets up a passivation layer. Hence, an estimated thickness of $2 \cdot 6$ nm seems to be reasonable and does certainly not overestimate the oxide thickness.

In figure 3.14(a) also the transmission of a 200 nm thick titanium filter is plotted. Titanium has an absorption edge at 32.6 eV [CXRO, 2009], i.e. the 21st harmonic. This fact will be used to calibrate the spectrometer and is presented in chapter 4.2.

3.3.4 Characterization of XUV radiation

This section is addressed to the diagnostics of the HHG setup. To characterize the harmonics a spectrometer, a XUV-CCD, an electron multiplier, and a XUV photodiode have been employed. All devices are being explained within this section.

On-line XUV detector - HHmeter

In order to measure the HHG process quantitatively and parasitically to the seeding experiment an electron multiplier can be used. Directly after the generation of the harmonics a Hamamatsu RS2362 has been set up within the second differential pumping stage (see figure 3.13). As long as high harmonics are generated, the residual gas is ionized and the generated ions are detected. A negative voltage is applied to the anode of the electron multiplier which causes the ions to accelerate. The corresponding signal is then amplified

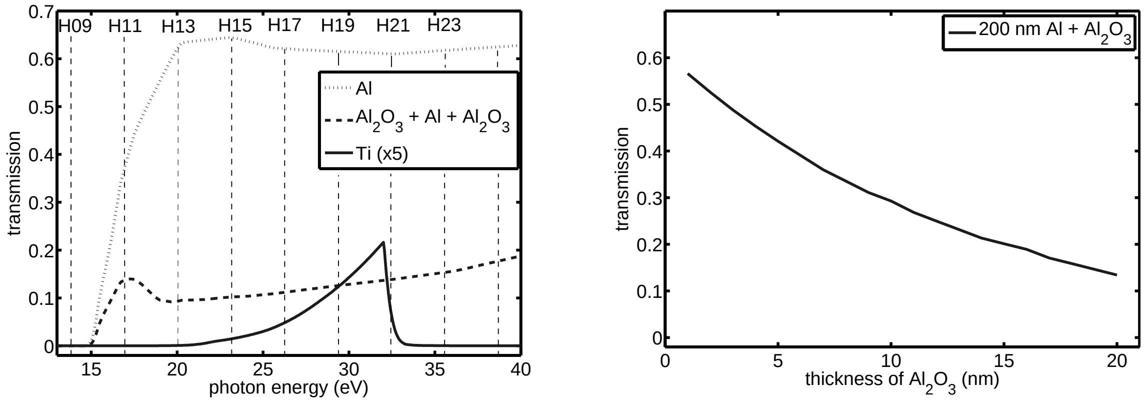

(a) (b)

Figure 3.14: Calculated transmission of the used filters as in [Lawrence Berkeley National Laboratory, 2011]. Figure 3.14(a) shows the total aluminum transmission with and without 10 nm oxidation layer on each side of the filter. The titanium transmission is multiplied with a factor of 5. Figure 3.14(b) shows the transmission of H21 through a 200 nm thick aluminum filter dependent on the thicknesses of the Al_2O_3 layer.

and consists of contributions which can be attributed to ions with various masses. The signal is displayed on a scope and can be used to measure relative changes of the HHG process. On the one hand the signal depends on the amount of generated harmonics. On the other hand the signal depends on the pressure of the residual gas. The pressure of the residual gas itself depends on the gas load and the time the system has been vented the last time. In other words: the signal differs on a daily basis and the device has to be calibrated on a daily basis in order to measure absolute photon numbers. It is further disadvantageous that not only the 21^{st}, but all harmonics with orders ≥ 11 are contributing to the signal. An advantage is that this device can be used parasitically to the seeding experiment. Moreover, no optics are between the generation and the detection of the harmonics, thus the uncertainty of the reflectivity does not contribute to the calculated number of photons. The calculated number depends on the partial cross section and the number of argon atoms. The cross section of argon has been published in [Becker and Shirley, 1996] and is shown in table 3.2, where only the 3p sub-shell of argon is considered to contribute to the ionization process. The details to the deduction of absolute photon numbers will be given in chapter 4.3.2.

XUV diode

In addition to the HHmeter a XUV photodiode (International Radiation Detectors, Inc.) has been installed within the injection beamline. In contrast to the HHmeter this device cannot be used in parallel to the seeding experiment. It is still advantageous that the device can be used without any optics. As in the case of the HHmeter the photodiode

Table 3.2: Partial cross section σ for the 3p sub-shell of argon. The data is taken from [Becker and Shirley, 1996].

harmonic order	σ (Mb)
H11	32.7
H13	35.2
H15	35.8
H17	31.3
H19	22.1
H21	13.9
H23	7.8
H25	4.2
H27	1.9
H29	0.9

is aligned in a direct line of HHG. The position is located eight meters after the gas target (figure 3.4). Three differential pumping stages, i.e. three apertures are between the generation and the detection of the harmonics. To ensure that the driving laser is completely blocked, in addition to the aluminum coating of the diode a 200 nm thick aluminum filter has been installed within the injection beamline [Bödewadt, 2011]. The detected signal is amplified with a PA100 amplifier (International Radiation Detectors, Inc) and visualized on a fast scope. The details to the deduction of absolute photon numbers will be given in chapter 4.3.2.

Spectrometer

A more detailed characterization of the harmonics is due to the lack of space not possible, neither within the pit nor the injection beamline. As shown in figure 3.13 a transfer beamline has been built up to further characterize the harmonics. The diagnostic branch consists of a spectrometer as well as a near- and far- field monitor of the 21st harmonic and is illustrated in figure 3.15. The idea is to investigate either the spectral, or the spatial properties of the harmonic. In case of the far- field monitor an image of the harmonic beam waist can be investigated. On the one hand, the distance between HHG and the focusing optic ($f_{H21} = 1.5$ m) is approximately 5 m. On the other hand, the distance between HHG and the focusing optic ($f = (6.25, 7.00, 8.50)$ m) of the injection beamline is approximately 12 m. Thus, the image in the diagnostic section corresponds to a down-scaled image of the beam waist in the undulator. In case of the near-field monitor the divergence of H21 can be measured.

The spectrometer is constructed on a $\varnothing\ = 400$ mm sized breadboard and consists of a a grazing incidence focusing mirror ($f = 500$ mm, < 1 Å surface roughness, fused silica superpolished), a grating (Au coating, 4° blazing angle, 1200 grooves per mm), a multi-channel plate, a fluorescence screen, and a CCD. The CCD is not included in figure 3.15

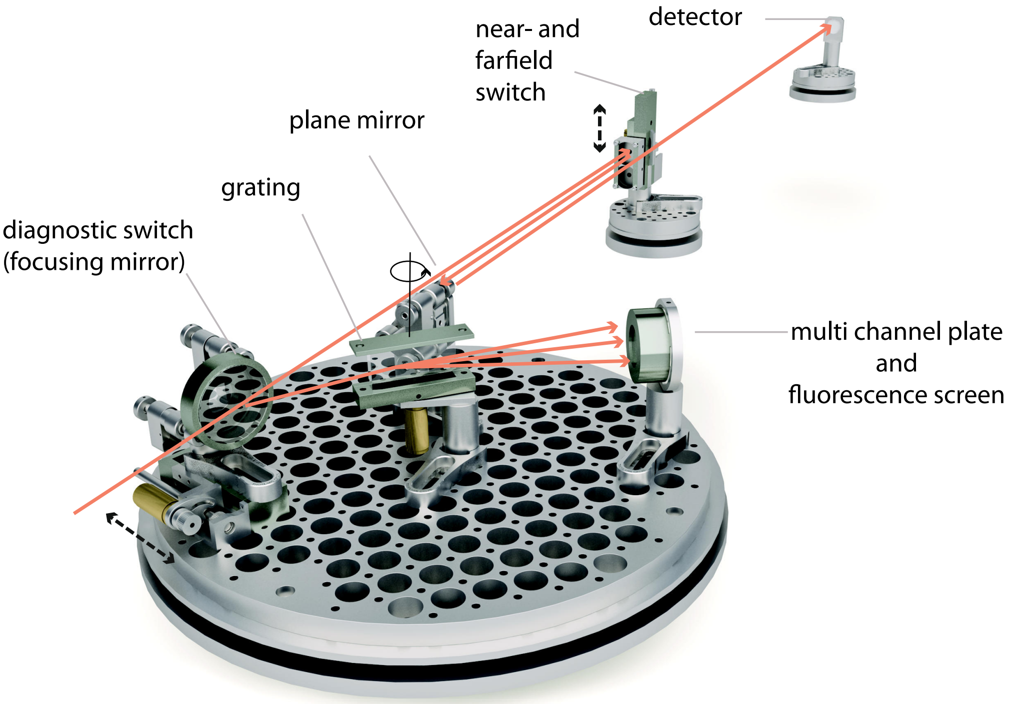

Figure 3.15: Rendered CAD model of the diagnostic branch. The spectrometer consists of a focusing mirror, a grating, a multi-channel plate, and a fluorescence screen. The grating is motorized and is rotatable in order to scan through the different harmonic orders. The focusing mirror is mounted on a translation stage and can be moved out of the beam path to measure the near- or far-field beam profile of H21.

and has been set up in front of the vacuum chamber, in order to image the spectra of the fluorescence screen. The design of the spectrometer is mainly based on [Schroedter, 2009]: the harmonics are focused with a spherical grazing incidence (15°) mirror in order to achieve an astigmatic focus of the harmonic comb. Right after the focusing mirror (115 mm distance) the harmonics pass a grating and get spatially separated, which can be described with the grating equation:

$$n\lambda = d(\sin(\beta) \pm \sin(\beta')), \tag{3.1}$$

where n describes the order, λ the wavelength, $d = 190$ mm the distance between the grating and the MCP, β the angle of incidence, and β' the emergent angle. Due to the large angle (75°) between the normal of the focusing grazing incidence mirror and the harmonics, the position of the focus in x and y direction is separated. In combination with the grating the harmonics appear as line foci at the fluorescence screen and can be recorded with the CCD camera in front of the chamber. More details about grating theory can be found for instance in [Palmer and Loewen, 2005].

The main purpose of the spectrometer is to image the spectrum around 32 eV without any overlapping of the harmonic peaks. The resolution of the spectrometer depends on the focusing optic and d. The larger the distance between the grating and the position where the harmonics are focused in y-direction, the more the harmonics are separated as described by equation 3.1. In addition, the harmonics are focused on the Rowland circle and are blurred before and after that position. In order to have a focused beam within the chamber and a resolution high enough to dissolve all appearing harmonics a ZEMAX simulation has been performed.

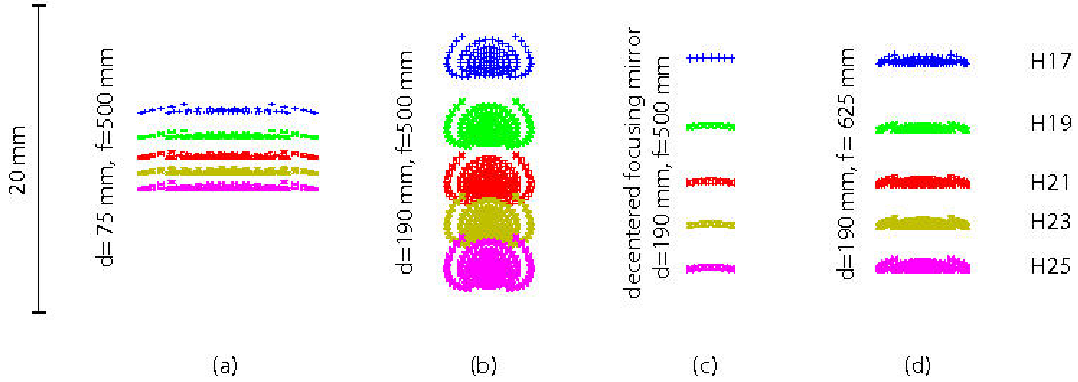

Figure 3.16: Simulation of different spectrometer configurations. (a) corresponds to $d = 75$ mm, where (b)-(d) correspond to $d = 190$ mm.

ZEMAX is a software which can be used for a number of applications as for instance laser beam propagation [ZEMAX LLC, 2011]. In figure 3.16 different configurations of the spectrometer are shown. ZEMAX calculates for a focusing optic of $f = 500$ mm that the optimal position of the MCP is 75 mm after the grating. The harmonics are separated and focused in one direction. Because each harmonic has a certain bandwidth the distance between two consecutive harmonics should be increased in terms of a larger d. In that case, the harmonics are not focused anymore and blurring causes the harmonics to overlap, as shown in figure 3.16(b). To circumvent this overlap the focusing optic has to be decentered (3.16(c)): the mirror is moved off axis and only a fraction of the light passes the mirror. The resulting effect is the same as introducing a slit in front of the mirror.

In figure 3.17 the influence of different slits on the spectrum is shown: the smaller the slit, the narrower becomes the individual harmonic and the more the harmonics become separated from each other. However, the disadvantage of decentering the focusing optic or introducing a slit is that the amount of light is reduced, but the relative position of the harmonics remain the same, though. A better solution would be to exchange the available

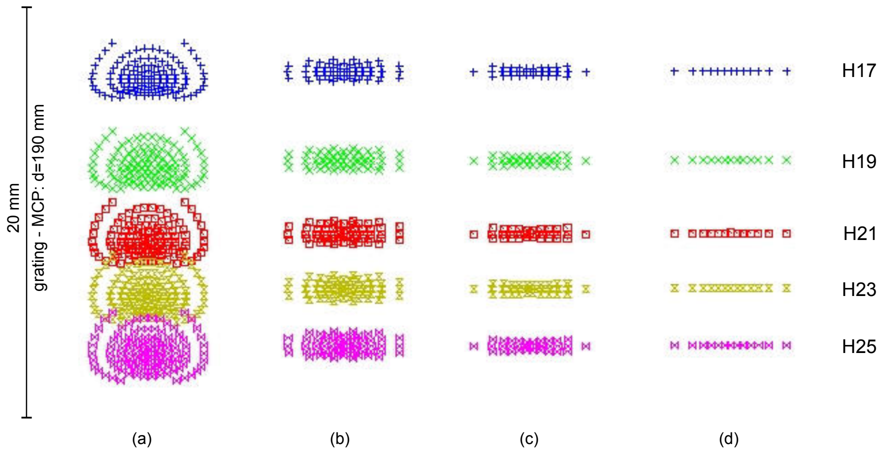

Figure 3.17: Simulation of different slits in front of the spectrometer. (a) corresponds to the case without a slit. (b) corresponds to a 1 mm slit, in contrast to (c) and (d) which correspond to a 0.5 mm and 0.2 mm slit, respectively.

optic to a focal length of $f = 625$ mm (figure 3.16(d)). Then the Rowland circle is located at $d = 190$ and no decentering is needed. So far, the optic has not been exchanged, because the brightness of the harmonics is good enough to evaluate the recorded spectra.

However, regardless of the alignment the spectrum is modulated with the transmission of the beamline, i.e. the wavelength dependent reflectivity of the XUV optics (mirrors and grating) as well as the wavelength dependent transmission through the aluminum filter.

XUV CCD

In addition to the spectrometer a near- and far-field monitor for the 21^{st} harmonic has been set up. Figure 3.15 shows that the focusing mirror of the spectrometer is mounted on a translation stage. After moving this mirror out of the beam the harmonics travel to the near- and far-field switch. Here, either a focusing or a plane mirror can be selected. In order to achieve a focal spot with a minimal degree of astigmatism a multilayer as described in section 3.3.2 is used in combination with an angle of incidence around zero degree. Due to the lack of space the harmonics are then folded and travel to a XUV-CCD, which is mounted on a 400 mm long manipulator (not shown) for focus-scans.

The results shown in chapter 4 are acquired with a back-illuminated CCD (PIXIS-XO:2048B). The CCD chip has a resolution of 2048 pixel × 512 pixel, where the pixel size is 13.5 μm. In order to calculate absolute photon numbers of the source the total transmission of the beamline to the XUV-CCD has to be known. Due to the reduced bandwidth of the multilayers only the 21^{st} harmonic is transmitted to the XUV-CCD.

The estimated transmission factor for H21 is

$$\begin{aligned} T_{tot} &= T^3_{B4C,s-pol} \cdot T^3_{B4C,p-pol} \cdot T^2_{ScSi} \cdot T_{Al} \\ &= 0.014 \pm 0.008, \end{aligned} \tag{3.2}$$

where $T_{B4C,s-pol} = 0.78 \pm 0.05$, $T_{B4C,p-pol} = 0.69 \pm 0.05$, $T_{ScSi} = 0.55 \pm 0.15$, and $T_{Al} = 0.24 \pm 0.06$ ($2 \cdot 6$ nm Al_2O_3). The radiation is reflected by $90°$ at each triplet system and changes the polarization from p- to s-polarized light. In addition two multilayer mirrors reflect at approximately zero degree, hence the reflectivity does not depend on the polarisation. The last factor of the transmission equals the transmission of the aluminum filter. The huge uncertainty is mainly due to the reflectivity of the used multilayer, as well as the transmission through the aluminum filter as explained in section 3.3.2 and 3.3.3.

Experimental results 4

This chapter concerns with the results on HHG, as well as the investigation, and optimization of the driving laser. Afterwards, the calibration of the spectrometer is described followed by a detailed investigation of the high harmonic source. At the end, the seeding experiment sFLASH is described and preliminary results are shown.

4.1 Fundamental laser

The driving laser is the basis of HHG. In order to achieve efficient HHG a thorough optimization of the laser performance has to be established. This section is addressed to the characteristics of the used driving laser.

4.1.1 Laser pulse duration

The pulse length of the driving laser is a crucial parameter for HHG [Zhou et al., 1996]. To ensure a pulse length of specified 35 fs the spectrum of the laser oscillator as well as a FROG (Frequency Resolved Optical Gating) measurement [Trebino and Kane, 1993; Kane and Trebino, 1993a,b] after the UHV grating compressor have been performed. In figure 4.1 the measured oscillator spectrum and the pulse length of the driving laser are shown. The solid lines in figure 4.1 correspond to Gauss fits and the dotted lines to measured data. In figure 4.1(a) the spectrum of the laser oscillator shows a spectral bandwidth of $\sigma_\lambda = (13.8 \pm 0.1)$ nm for a central wavelength of $\lambda_{\text{central}} = (811.3 \pm 0.1)$ nm. Due to the Fourier limit of a Gaussian pulse [Saleh and Teich, 1991] the pulse length of the driving laser is not shorter than

$$\sigma_t \geq \frac{1}{4\pi\sigma_\nu} = (12.7 \pm 0.3)\text{ fs},$$

where σ_ν is the rms value of the frequency bandwidth. In figure 4.1(b) the FROG measurement shows a pulse width of $\sigma_t = (14.0 \pm 0.1)$ fs, which corresponds to

$$t_{\text{FWHM}} = (32.9 \pm 0.2)\text{ fs},$$

that is 10% longer than the Fourier-limited Gaussian pulse. It also shows that the amplification process has a negligible impact on the spectrum and the corresponding pulse length.

4.1.2 Laser beam profile and intensity

HHG depends strongly on the quality of the driving laser. In order to ensure optimal conditions not only the pulse length as described in the previous section, but also the focus

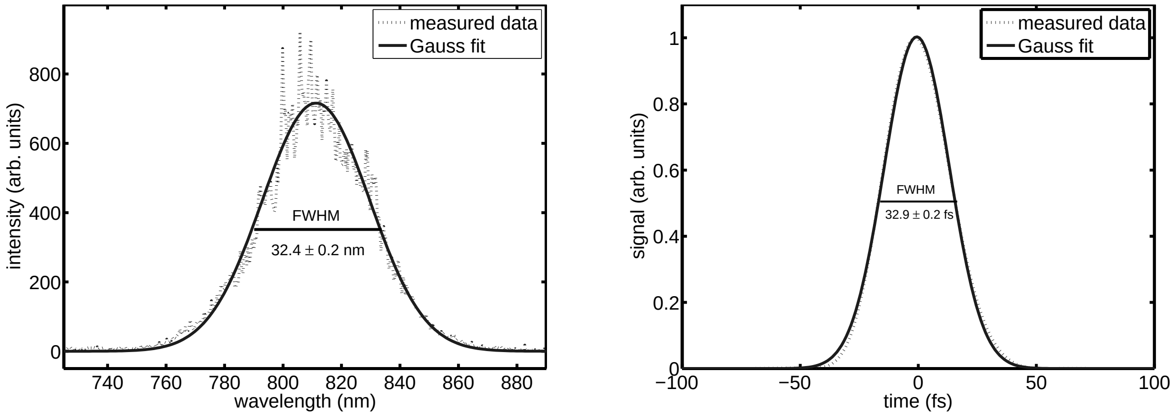

(a) (b)

Figure 4.1: Figure 4.1(a) shows the spectrum of the oscillator with a central wavelength of $\lambda_{central} = (811.3 \pm 0.1)$ nm and a bandwidth of $\sigma_\lambda = (13.8 \pm 0.1)$ nm. Figure 4.1(b) shows the pulse length of the driving laser after the UHV grating compressor.

and the beam quality factor M^2 are investigated. In figure 4.2 focus scans of the driving

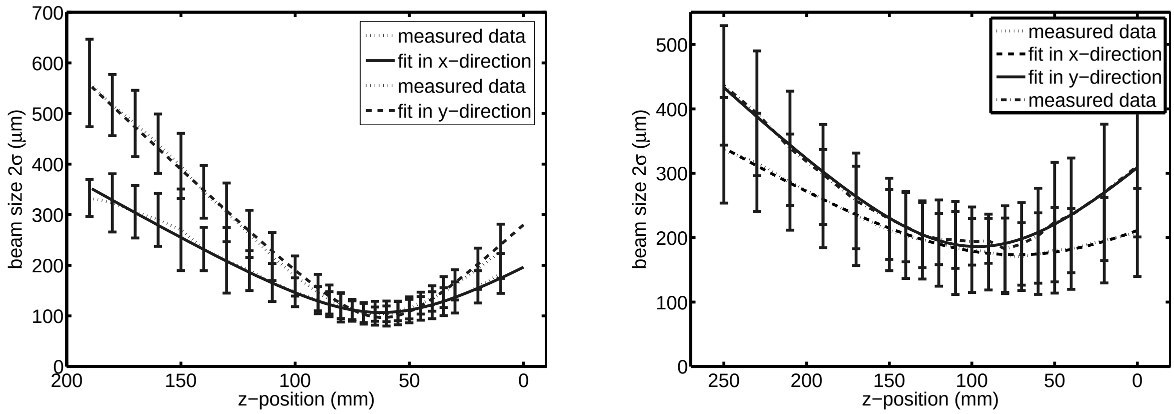

(a) (b)

Figure 4.2: Measured beam profile of the driving laser, where the laser travels from left to right. Figure 4.2(a): $f_{NIR} = 1500$ mm, figure 4.2(b): $f_{NIR} = 3000$ mm

laser with $f_{NIR} = 1500$ mm and $f_{NIR} = 3000$ mm are plotted. The direct comparison shows that a larger focal length leads to a larger beam waist, and a smaller divergence. Furthermore, in case of $f_{NIR} = 1500$ mm no astigmatism is found, where in case of $f_{NIR} = 3000$ mm the beam first focuses in y-direction and 24 millimeters behind in x-direction. In case of $f_{NIR} = 3000$ mm the laser hits the focusing optic with an angle $\alpha \approx 5°$ which causes the astigmatism. For $f_{NIR} = 1500$ mm the angle is approximately $\alpha \approx 0°$ as explained in chapter 3.2.2 and the astigmatism is absent or at least not resolvable. Note that the position of the beam waist is different, but that is due to a slightly different setup.

In order to fit the measured data to equation 2.12 the second moment as described in [Reng and B.Eppich, 1992] with $p = 2 \wedge q = 0$, or $p = 0 \wedge q = 2$ is calculated

$$\begin{aligned} \mu_{pq} &= \frac{\sum_x \sum_y (x-\overline{x})^p (y-\overline{y})^q I(x,y)}{M_{00}}, \\ \text{with} \qquad \overline{x} &= \frac{M_{10}}{M_{00}}, \\ \overline{y} &= \frac{M_{01}}{M_{00}}, \\ \text{and} \qquad M_{ij} &= \sum_x \sum_y x^i y^j I(x,y), \end{aligned}$$

where $I(x,y)$ is the pixel value at (x,y). In addition,

$$W = 2\sigma = 2\sqrt{\mu_{pq}}$$

can be calculated and a beam waist fit can be applied. In case of the $f_{NIR} = 3000$ mm geometry the fit leads to:

$$\begin{aligned} M_x^2 &= 1.12 \pm 0.02 & M_y^2 &= 1.87 \pm 0.05 \\ W_{0,x} &= (173 \pm 2)\ \mu\text{m} & W_{0,y} &= (186 \pm 4)\ \mu\text{m} \\ z_{0,x} &= (73 \pm 2)\ \text{mm} & z_{0,y} &= (97 \pm 2)\ \text{mm}, \end{aligned}$$

where the x-direction corresponds to μ_{20} and the y-direction to μ_{02}. $z_{0,x}$ and $z_{0,y}$ correspond to the focus position in x- and y-direction, respectively. The position $z = 0$ is set to the beginning of the translation stage. In case of the $f_{NIR} = 1500$ mm geometry the fit leads to:

$$\begin{aligned} M_x^2 &= 1.11 \pm 0.05 & M_y^2 &= 1.62 \pm 0.08 \\ W_{0,x} &= (107 \pm 4)\ \mu\text{m} & W_{0,y} &= (97 \pm 6)\ \mu\text{m} \\ z_{0,x} &= (62 \pm 2)\ \text{mm} & z_{0,y} &= (62 \pm 2)\ \text{mm} \end{aligned}$$

Based on those quantities the Rayleigh length can be calculated with equation 2.13:

$$\begin{aligned} z_{R,x}(f = 3000\text{mm}) &= (105 \pm 4)\ \text{mm} \\ z_{R,y}(f = 3000\text{mm}) &= (73 \pm 5)\ \text{mm}, \end{aligned}$$

as well as

$$\begin{aligned} z_{R,x}(f = 1500\text{mm}) &= (41 \pm 5)\ \text{mm} \\ z_{R,y}(f = 1500\text{mm}) &= (23 \pm 4)\ \text{mm}. \end{aligned}$$

For HHG the intensity of the driving laser is a crucial parameter. On the one hand the intensity can be adjusted by simply moving the gas target through the focus of the driving

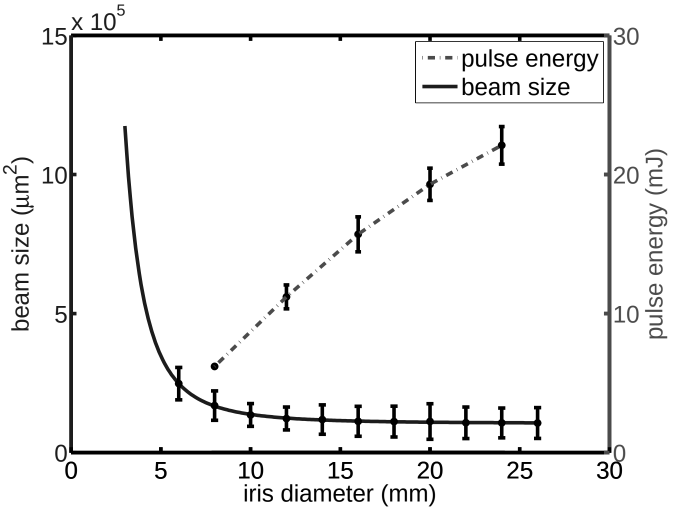

Figure 4.3: Beam size and energy of the driving laser (after the UHV compressor) for $f_{NIR} = 3000$ mm at focus position $z = 100$ mm as shown in figure 4.2(b).

laser. On the other hand the intensity depends on the beam diameter at the focusing optic and can be adjusted by changing the diameter of the iris in front of the focusing mirror. Here the near field beam profile has a beam diameter of $FWHM = 13$ mm. In figure 4.3 the focal spot size and the pulse energy of the driving laser is plotted for $f_{NIR} = 3000$ mm and different diameters of the iris. Here, the spot size decreases for a larger diameter, thus the intensity becomes higher. Additionally, the pulse energy increases for a larger iris which increases the intensity at the focus even more.

For a rectangular pulse the intensity is defined as

$$I = \frac{E}{A \cdot \Delta t} \tag{4.1}$$

where E is the pulse energy, A the spot size, and Δt the pulse width. For $f_{NIR} = 3000$ mm, $z = 100$ mm, and $\Delta t_{FWHM} = (32.9 \pm 0.2)$ fs the achieved intensity depends only on the diameter of the iris and can be approximated with equation 4.1. For a diameter of 10 mm the spatially averaged intensity $\tilde{I}$ becomes

$$\begin{aligned} \tilde{I}(d = 10 \text{ mm}) \quad &= (1.9 \pm 0.4) \cdot 10^{14} \text{ W/cm}^2 \\ &\text{with} \qquad E = (8.7 \pm 0.8) \text{ mJ} \\ &\text{and} \qquad A = (1.4 \pm 0.3) \cdot 10^5\ \mu\text{m}^2, \end{aligned}$$

where the area A is calculated in terms of the W radius. In contrast to a diameter of 24 mm:

$$\begin{aligned} \tilde{I}(d = 24 \text{ mm}) \quad &= (6.1 \pm 2.2) \cdot 10^{14} \text{ W/cm}^2 \\ &\text{with} \qquad E = (22.1 \pm 1.3) \text{ mJ} \\ &\text{and} \qquad A = (1.1 \pm 0.4) \cdot 10^5\ \mu\text{m}^2 \end{aligned}$$

For $f_{NIR} = 1500$ mm the beam waist is approximately 1.8 times smaller. Hence, the maximal intensity is a factor of approximately 3.2 times bigger, i.e. a maximal value of $\approx 2.0 \cdot 10^{15}$ W/cm^2 in case of 24 mm diameter of the iris.

4.1.3 Polarization

For the measurement of the polarization two polarizers and a photodiode have been employed. Polarizer P has a fixed reflectivity of $> 99.8\%$ for the s-polarized light and transmits almost only the p-polarized light. Polarizer A (analyzer) is mounted on a rotatable mount, but its quality is unknown and worse than polarizer $P1$. The degree of the polarization R is defined as the ratio of the intensity of the polarized portion to the total intensity [Born and Wolf, 1980; Collett, 1992]:

$$R = \frac{I_{min}}{I_{max}},$$

where I_{min} is the polarized portion and I_{max} is the total intensity. The analyzer is not a perfect polarizer and transmits independent of its orientation a fraction of the p-polarized light. In order to determine this portion the contrast ratio of the analyzer is measured after the light has passed the first high-quality polarizer and leads to a contrast ratio of

$$\begin{aligned} R_{err} &= (1.00 \pm 0.04) \cdot 10^{-3} \\ &\text{with} \qquad I_{max,err} = (4.7 \pm 0.1) \cdot 10^{-7} \text{mV} \cdot \text{s} \\ &\text{and} \qquad I_{min,err} = (4.7 \pm 0.1) \cdot 10^{-10} \text{mV} \cdot \text{s}. \end{aligned}$$

Note that for a perfect polarizer $I_{min} = 0$ and the corresponding contrast ratio is also zero $(R = 0)$. Finally, the polarization degree of the laser can be determined by removing the high-quality polarizer and measuring the contrast ratio of the analyzer R_A.

$$\begin{aligned} P_{laser} &= R_A - R_{err} \\ &\text{with} \qquad R_A = \frac{I_{min,A}}{I_{max,A}}. \end{aligned}$$

With

$$\begin{aligned} R_A &= (2.7 \pm 0.1) \cdot 10^{-3} \\ I_{max,A} &= (4.7 \pm 0.1) \cdot 10^{-7} \text{mV} \cdot \text{s} \\ I_{min,A} &= (1.23 \pm 0.04) \cdot 10^{-9} \text{mV} \cdot \text{s} \end{aligned}$$

the polarization degree of the driving laser is

$$P_{laser} = (1.6 \pm 0.1) \cdot 10^{-3}.$$

The polarization is a crucial parameter [Dietrich et al., 1994] and may spoil the HHG process or at least reduces the HHG CE. The calculated result corresponds to 99.8% p-polarized light which is a sufficient degree of polarization for HHG.

4.1.4 Wavefront

In order to measure the wavefront of the driving laser a Shack-Hartmann sensor has been employed [Hartmann, 1900; Shack and Platt, 1971]. The measured wavefront can be evolved in Zernicke polynomials which lead directly to the aberrations. M. Schulz investigated the wavefront directly after the laser oscillator [Schulz, 2010]. It turned out, that the fundamental seed is characterized with a defocus, as well as a small astigmatism. The defocus leads to a larger beam waist, as well as a shift of the focus relative to the nominal focus position. The astigmatism causes a spatial separation of the focus in x- and y-direction. As shown in figure 4.2(a) the astigmatism can not be resolved, thus it is neglectable. During this work the measurement has been performed after the laser amplifier. The results are comparable to those published in [Schulz, 2010]. It shows, that the amplifier has a negligible impact on the wavefront aberrations. Details can be found in [Schulz, 2010].

4.2 Calibration of the spectrometer

For the calibration of the spectrometer three different methods have been employed. The fastest and online available method uses an aluminum filter to identify the 11th harmonic. The second approach minimizes the deviation between the expected and the measured spectrum. The last and most accurate method uses the fact that the high harmonic spectrum can be spectrally shifted by changing the pulse length of the driving laser. This spectral shift in combination with a titanium filter allows an absolute calibration of the spectrometer. All three methods will be explained within this chapter.

4.2.1 Online calibration

The transmission of an aluminum filter is shown in figure 3.14(a). The lowest transmitting order is the 11th harmonic, i.e. 17 eV. Thus, the first appearing peak is the 11th harmonic. This method is fast, but not precise. It implies that the 11th harmonic is generated and reflected sufficiently by the grazing incidence triplet mirrors. Furthermore, the spectral position of each harmonic order is expected to be fixed. Any variation of the fundamental frequency cannot be detected with this method.

4.2.2 Quasi online calibration

First, the CCD camera with objective which images the fluorescence screen after the MCP has to be calibrated, i.e. the distance of two given pixels has to be determined and converted in millimeters by imaging a reference object, e.g. millimeter paper. Then, the recorded spectra are binned in direction of the unfocused beam. The distances between one arbitrary and all other appearing peaks are measured. Then, those distances are calculated theoretically with equation 3.1. The resulting distances depend on the wavelength of that arbitrarily chosen peak and the angle between the incoming beam and the grating. Those two free parameters are changed until the differences between the measured and theoretical calculated distances of the peaks reach an absolute minimum. Then the two parameters are set and the calibrated spectrum can be calculated with equation 3.1. The method implies that the central wavelength of the driving laser does not change on a daily basis, which is fulfilled in practice. It also implies that the harmonics are being generated without any spectral shift, which is not necessarily the case. The following section will show the impact of a spectral shift on the wavelength.

4.2.3 Absolute calibration

This method is an extension of the quasi online calibration. In addition to the previously described procedure the transmission through a titanium filter is measured. The transmission itself

$$T(\omega) = \frac{I_{Ti}(\omega)}{I_0(\omega)}$$

depends on the frequency of the radiation, where $I_{Ti}(\omega)$ and $I_0(\omega)$ are the recorded intensities with and without a titanium filter, respectively. In figure 3.14(a) the theoretical transmission curve of a 200 nm thick titanium filter is plotted which has a sharp edge at 32.6 eV [CXRO, 2009].

Because the spectral position of the 21^{st} harmonic (≈ 32.5 eV) depends on the fundamental laser pulse length as shown in [Zhou et al., 1996] it is possible to spectrally shift H21 over the absorption edge of the titanium filter and to sample the transmission curve as shown in figure 4.4.

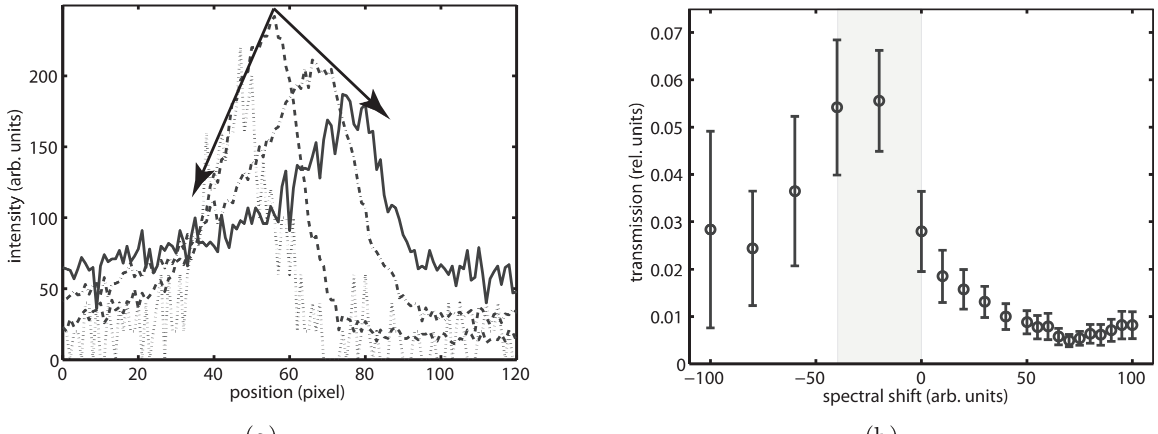

(a) (b)

Figure 4.4: Figure 4.4(a) shows the spectral shift of the 21^{st} harmonic depending on the pulse length of the driving laser without a titanium foil, where the x-axis corresponds to the horizontal CCD position. Figure 4.4(b) shows the transmission of H21 through a titanium foil for different spectral shifts of H21.

The laser pulse duration has been changed by introducing a chirp, i.e. a time dependence of the instantaneous laser frequency. Here the grating of the first pulse compressor is moved, a chirp is introduced, and the pulse length of the driving laser gets longer. In figure 4.4(a) it is shown that for a blueshift of approximately 20 pixel the intensity drops more than 20%. The impact of this statement will be discussed at the end of this section. It is possible to shift the 21^{st} harmonic beyond the absorption edge of the titanium filter and to sample the transmission curve. The measured transmission of the 21^{st} harmonic is plotted in figure 4.4(b) for a 200 nm thick titanium filter. The shown errors depend on the statistical errors of $I_{Ti}(\omega)$ and $I_0(\omega)$ and are calculated in terms of error propagation. It is shown, that the error-bars become bigger for a redshift of H21 compared to a blueshift. This is due to the asymmetric dependence of the H21 signal on the spectral shift as also indicated with the arrows in figure 4.4(a). An explanation will be given a bit later. The plot 4.4(b) shows qualitatively a similar behavior as the theory in figure 3.14(a). The absolute difference is most likely due to stray light. In conclusion, the absorption edge of 32.6 eV has to be between values of 0 and −40 in figure 4.4(b) (shaded area). This region from 0 to −40 for the absorption edge of 32.6 eV can be used as the error of this method. In figure 4.5 two spectra for a spectral position of −20 and −40 are shown. Because the two peaks of the 21st harmonic differ by 7 pixels, 32.6 eV has to match a pixel number of 830 ± 7 pixels in the recorded image.

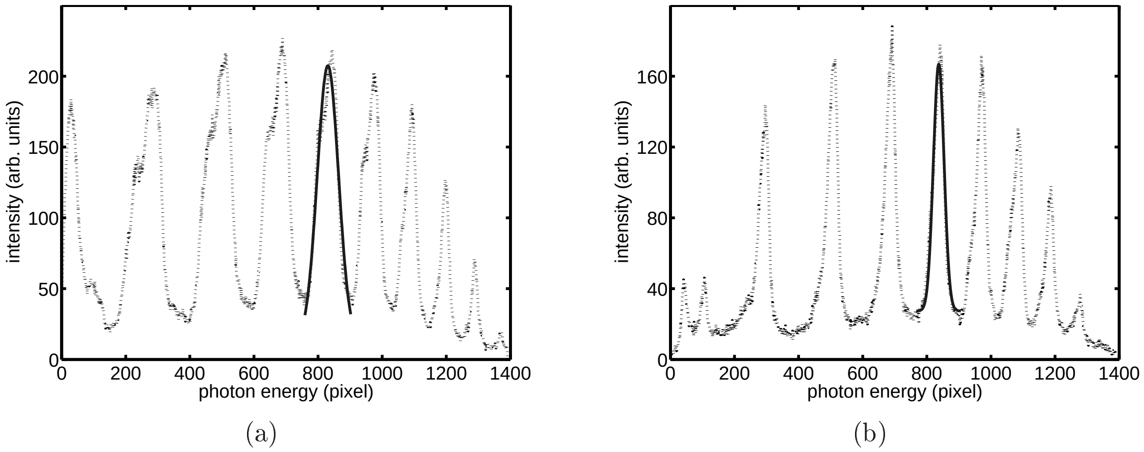

(a)

(b)

Figure 4.5: Spectra for two different spectral positions of the harmonic comb. Figure 4.5(a) corresponds to a spectrum with a spectral shift of (−20) and figure 4.5(b) to a shift of (−40). The solid line corresponds to a Gauss fit with a central position of $x_c = 830$ and $x_c = 837$, respectively.

This boundary condition reduces the optimization procedure described within the quasi online calibration by one degree of freedom and leads to the calibrated spectrum shown in figure 4.6 with a central wavelength of

$$E_{central,H21} = 32.7 \text{ eV} \pm 0.2 \text{ eV}$$

In general it is possible to blueshift the 21^{st} harmonic by 0.5 eV but the associated yield drops down to less than 80%. Smaller changes in the order of +0.3 eV lead to a loss of roughly 10% and would therefore be tolerable. Compared to the width of the Gauss fit

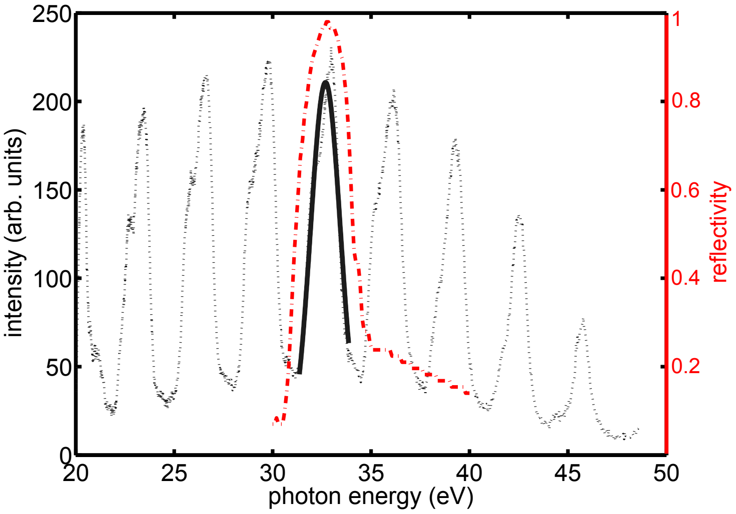

Figure 4.6: Calibrated and optimized spectrum with a central wavelength of the 21st harmonic $E_{central,H21} = (32.7 \pm 0.2)$ eV. The black and continuous line corresponds to a Gauss fit of the 21st harmonic and the red line corresponds to the reflectivity of the used multilayer.

of $\sigma_{H21} = 0.7$ eV (shown in figure 4.6) it is possible to blueshift the 21st harmonic by almost 50% of its width. A redshift of the harmonics is also possible, but the resulting yield is lower. This can be explained with an increase of the total phase mismatch. In contrast, the phase mismatch introduced by a blueshift does compensate the phase mismatch caused by free electrons. Therefore it is not feasible to tune the harmonics to smaller wavelengths. The red curve in figure 4.6 corresponds to the reflectivity of the used multilayer as explained in chapter 3.3.2. Although the exact position of the peak in the reflectivity is not known exactly the plot shows that the bandwidth of the used multilayer is bigger than the bandwidth of the 21st harmonic. The absolute calibration of the spectrometer is restricted to an absolute calibration of the 21st harmonic. For an entire calibration a second reference point, i.e. a second absorption edge for instance has to be used to calibrate the whole spectrum.

4.3 High Harmonic Generation

This section is addressed to the results concerning the HHG source. The properties of the 21st harmonic with regard to the seeding experiment are examined. The first section specifies the beam propagation properties as well as the energy of the 21st harmonic. Then the influence of the driving laser on the spectrum is analyzed. At the end, a summary on wavefront investigations and further techniques like QPM as well as two color HHG is given. In all cases, unless it is stated explicitly, the noble gas of choice is argon.

4.3.1 XUV beam propagation

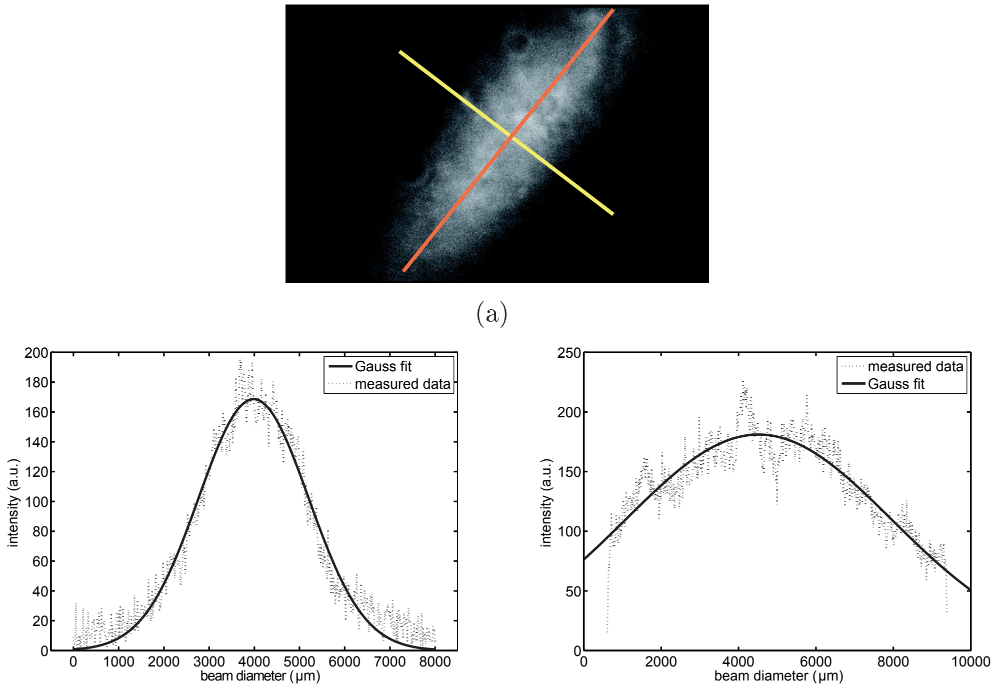

(a)

(b)

(c)

Figure 4.7: H21 near field beam profile for a driving laser with $f_{NIR} = 1500$ mm. The yellow line (narrow direction) represents the data in figure 4.7(b) and the red line represents the data in figure 4.7(c).

In order to determine the divergence of the 21^{st} harmonic two different methods have been employed. First, a geometrical optics (chapter 2.1.1) method is used. In figure 4.7 the near field beam profile of H21 acquired with the XUV CCD, as well as line scans in two orthogonal directions are shown ($f_{NIR} = 1500$ mm). The CCD camera is located at the position labeled as “detector” (see figure 3.15). The captured profile shows an asymmetric behavior and therefore two different divergences. In the following sections those two directions are being abbreviated as the narrow and the wide direction and correspond to the yellow and red line in figure 4.7(a), respectively. Furthermore, in both cases a fit for a Gauss function

$$\Phi(x) = a \cdot exp[-0.5(x - x_0)^2/\sigma^2]$$

has been performed which leads to a beam radius of $\sigma_{narrow} = (1217 \pm 18)\mu\text{m}$ and $\sigma_{wide} = (3437 \pm 71)\mu\text{m}$, respectively. The sharp drop off in 4.7(c) is due to the limited size of the CCD detector. However, to determine the divergence ϑ the distance z between the gas jet for HHG and the detector has to be known:

$$\tan(\vartheta) = \frac{W}{z} = \frac{2\sigma}{z} \approx \vartheta. \tag{4.2}$$

In case of $f_{NIR} = 1500$ mm the distance is $z = (6968 \pm 50)$ mm, thus a divergence of

$$\begin{aligned} \vartheta_{narrow} &= (0.34 \pm 0.01)\ \text{mrad} \\ \vartheta_{wide} &= (0.78 \pm 0.01)\ \text{mrad} \end{aligned}$$

can be calculated, where ϑ is half of the opening angle and the given errors correspond to a 95% confidence bound.

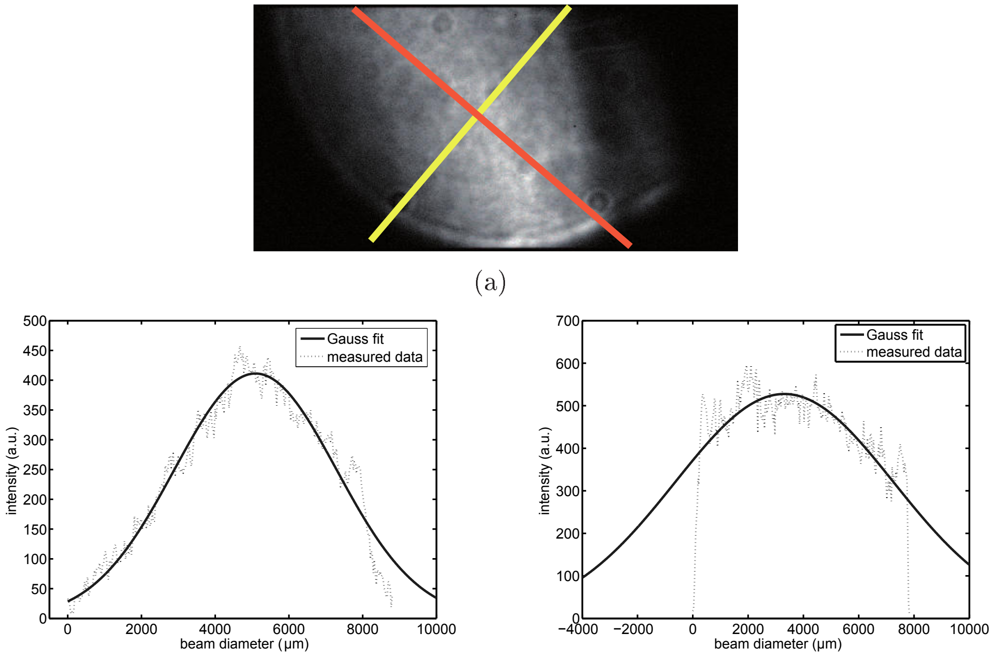

(a)

(b)

(c)

Figure 4.8: H21 near field beam profile for a driving laser with $f_{NIR} = 3000$ mm. The yellow line (narrow direction) represents the data in figure 4.8(b) and the red line (wide direction) represents the data in figure 4.8(c).

In figure 4.8 the H21 profile is shown for a driving laser with a focal length of $f_{NIR} = 3000$ mm. The direct comparison of figure 4.8(a) with figure 4.7(a) shows that for a larger focal length the divergence becomes larger, too. The spot size is that big that the stray light apertures block not only the fundamental laser, but the 21^{st} harmonic as well. Because a larger focal length of the driving laser leads to a smaller divergence of the driving laser this behavior was not expected. However, the applied line scans lead to a beam size of $\sigma_{narrow} = (2203 \pm 39)\mu\text{m}$ and $\sigma_{wide} = (3954 \pm 243)\mu\text{m}$. In the case of $f_{NIR} = 3000$ mm the distances, especially z are slightly different as explained in chapter 3.2.2. For a distance of $z = (7025 \pm 50)$ mm the divergence can be calculated with equation 4.2:

$$\begin{aligned} \vartheta_{narrow} &= (0.56 \pm 0.01)\ \text{mrad} \\ \vartheta_{wide} &= (0.84 \pm 0.03)\ \text{mrad} \end{aligned}$$

Additionally, Gauss optics as explained in chapter 2.1.2 can be used to determine the beam quality factor M^2. Here, the 21^{st} harmonic is assumed to be Gaussian, and a focus scan is applied. In figure 4.9 a focus scan for a focal length of $f_{H21} = 1.5$ m and $f_{NIR} = 3.0$ m is shown for the x and y-direction of the beam. For each position of the scan at least 50 images have been recorded and the second moment in x- and y-direction μ_{20} and μ_{02}, respectively has been calculated as explained in chapter 4.1.2. An image of the beam waist is shown in figure 4.9(b). It can be seen that the dimension is comparable to the resolution of the CCD and the width of the profile corresponds to $2-3$ pixels. For the x-direction the waist of the beam is visible and a beam waist fit as explained in chapter 2.1.2 can be applied. For a wavelength of $\lambda = 38.1$ nm and equation 2.6 the fit does not converge, hence the beam does not behave like a Fourier-limited Gaussian beam. 4.9(a) represents a beam waist fit with the position of the waist $z_0 = (505 \pm 17)$ mm , and the beam waist $W_{0,image} = (18 \pm 1)$ μm for $M^2\lambda = (3.5 \pm 0.2)$ nm, which corresponds to an $M^2 \approx 0.1$ for $\lambda = 38.1$ nm. An $M^2 < 1$ is physically not feasible [Siegman, 1993], thus the paraxial approach is not fulfilled and the Gaussian beam waist fit is not valid. In contrast to [Siegman, 1993] it is shown in [Luo and Wang, 2010] that the beam quality factor can be smaller than one for 86.5% power content ($1/e^2$-radius) of the beam and that the M^2 formalism is no longer suitable.

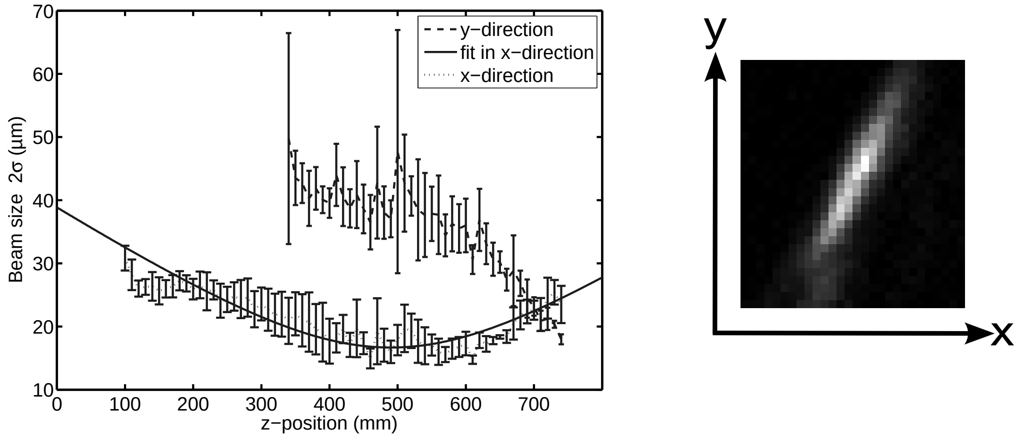

(a) Beam radius in x and y- direction for the 21^{st} harmonic.

(b) Image of the beam profile at position 500 mm.

Figure 4.9: Focus scan of H21 acquired in the diagnostic section of the HHG setup.

However, the triplet mirrors and the diagnostic switch in between the harmonic source and the detector are mounted and adjusted with a screw from its backside. Most likely this causes the beam to defocus. This effect has been studied lately by Drescher at al. and was not expected at the time the mounts were designed and manufactured. Note that this effect has been confirmed for a copy of the used triplet mounts. The used triplet mounts themselves have to be investigated during the next shutdown. In case of the

CCD two triplet mirrors and one diagnostic switch, i.e. seven mirrors are used to steer the beam to the detector. Each of those mirrors introduces (most likely) an additional divergence, thus the calculated divergences are an upper limit. On the one hand an absolute measurement of the divergence is due to the mirror mounts not possible. On the other hand it is possible to detect relative changes of the divergence. In table 4.1 a summary of the measured divergences is given. Errors cannot be estimated, because the actual influence of the mirror mounts differs and could not be determined. It can be seen, that the HHG focus geometry of $f_{NIR} = 1500$ mm leads to a lower divergence compared to the $f_{NIR} = 3000$ mm geometry. In case of $f_{NIR} = 3000$ mm a proper determination of the wide divergence ϑ_{wide} is due to the limited size of the CCD not possible. However, for seeding purposes it is desirable to achieve the highest possible flux of the harmonics. Therefore, the harmonic yield has to be measured, in order to deduce the appropriate focal length (next chapter). An exchange of those mirror mounts is desirable, but very time consuming. So far, sFLASH has been in the commissioning phase and a longer "shut down" of the HHG source and its diagnostics to exchange those mirror mounts was not available.

Table 4.1: Divergence of H21 for $f_{NIR} = 1.5$ m and $f_{NIR} = 3.0$ m

f_{NIR}	divergence
1500 mm	$\vartheta_{narrow} < 0.34$ mrad $\vartheta_{wide} < 0.78$ mrad
3000 mm	$\vartheta_{narrow} < 0.56$ mrad

However, figure 4.9 shows the position and the beam waist itself. Both can only roughly be estimated as

$$\begin{aligned} W_{0,image} &= (18 \pm 0.1)\ \mu\text{m} \\ z_{W_0} &= (505 \pm 17)\ \text{mm} \end{aligned}$$

It is further possible to deduce the size of the source W_{HHG}, i.e. the beam radius at the position of the gas target, the size of the the beam waist W_0, which is usually different than W_{HHG} and known as the virtual source, and the position of the virtual source, i.e. the position of the beam waist z_{W_0}. With a distance from the gas jet to the focusing mirror ($f_{H21} = 1500$ mm) in the diagnostic section of $g_{jet} = (5110 \pm 50)$ mm and a distance of $z_{image} = (2294 \pm 50)$ mm those quantities can be deduced with equation 2.1:

$$\begin{aligned} W_{HHG} &= (40 \pm 2)\ \mu\text{m} \\ W_0 &= (34 \pm 2)\ \mu\text{m} \\ z_{W_0} &= (2211 \pm 179)\ \text{mm} \end{aligned} \tag{4.3}$$

where z_{W_0} corresponds to a position of the waist (in laser propagation direction) behind the position of the gas jet. A calculation of the divergence is not possible, because the approach of a Gaussian beam is not valid and the introduced distortion of the beam profile cannot be estimated. In [Frumker et al., 2011] it is shown that the position of the harmonic beam waist, i.e. the virtual source position depends on the harmonic order and may be located in front and behind the gas jet. The deduced distance of $z_{W_0} = (2211 \pm 179)$ mm is comparably large compared to [Frumker et al., 2011]. This could be explained with the used triplet mirror mounts and the additionally introduced wavefront distortion.

4.3.2 Harmonic energy and conversion efficiency

To optimize the yield of HHG the phase matching conditions have to be optimized. In order to optimize the 21^{st} order, either the spectrometer, the XUV CCD, and the HHmeter can be used. In case of the spectrometer the signal of H21 is integrated and represents the energy of the 21^{st} harmonic in arbitrary units. In case of the CCD camera, the XUV photodiode, and the HHmeter absolute energies can be measured. To ensure an optimized harmonic yield within each of the following investigations all parameters have been optimized iteratively. The main parameters to optimize the yield are the position of the gas target relative to the focus of the driving laser, the backing pressure and timing of the gas nozzle, and the intensity of the fundamental driving laser as described in [Hergott et al., 2002; Kazamias et al., 2003a,b; Kim et al., 2004; Tamaki et al., 2000]. The results will be shown and explained within this chapter.

Target position

In figure 4.10 the H21 energy for different gas target positions relative to the focus of the driving laser is plotted, where the focus of the driving laser corresponds to position zero. The data has been acquired with the XUV CCD for $f_{\text{NIR}} = 3000$ mm of the driving laser. In front and behind the focus the intensity and the spot size of the driving laser is different. The plot shows a steep enhancement of the yield with an absolute maximum at 60 mm in front of the laser focus. Then the yield drops down until a smaller relative maximum of the yield appears 10 mm behind the focus. This behavior is in agreement with [Bellini et al., 2001] and can be explained as follows: the highest laser intensity is located at the focus of the driving laser. At this position ionization becomes dominant and electrons are present as explained in chapter 2.3.1, which leads to a phase mismatch. Furthermore, the Guoy phase changes its algebraic sign and the phase mismatch leads to depletion. Therefore it is expected to achieve a maximum on each side of the fundamental laser focus. For seeding purposes the H21 energy needs to be as high as possible. Therefore, the target is positioned ≈ 60 mm in front of the focus.

Target pressure

Pressure scans are mandatory to optimize the HHG yield and have to be performed for each target geometry. In figure 4.11 pressure scans are presented for a 20 mm long argon

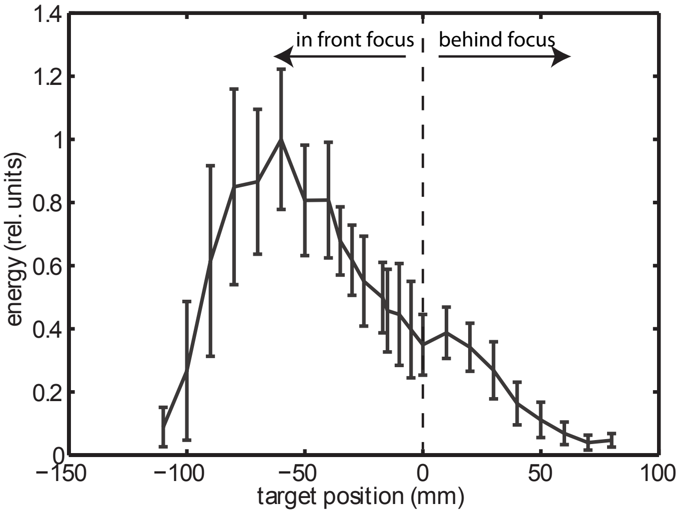

Figure 4.10: H21 yield dependent on the position of the gas target relative to the focus of the driving laser ($f_{NIR} = 3000$ mm). Here, the backing pressure of argon is set to 1800 mbar.

channel ($f_{NIR} = 1500$ mm). The target pressure depends on the backing pressure, the time delay between the gas valve trigger and the fundamental laser, and the opening period of the valve.

In figure 4.11(a) and 4.11(b) the yield of the 21st harmonic is shown for different backing pressures and a constant opening period of nominal 200 µs. The yield has been measured with the spectrometer and the pressure within the target has been set by changing the trigger of the gas valve relative to the driving laser, thus different times in figure 4.11 correspond to different pressures within the target.

For backing pressures between 500 mbar to 960 mbar the yield first increases up to a maximum followed by a drop down within approximately 200 µs, which can be explained as follows: the gas valve opens and the pressure within the target starts to raise until the valve closes again and the pressure decreases, thus the harmonic yield decreases too. For backing pressures larger than 1000 mbar the pressure curve shows two maxima which can be explained as follows: first, the gas valve opens and the pressure within the target starts to raise as in case of lower backing pressures. At a certain time, depending on the backing pressure, the target pressure exceeds its optimal value for the best phase matching conditions, thus the harmonic yield starts to decrease until the valve closes again. Here the phase mismatch is due to free-electrons as explained in chapter 2.3.3. As soon as the valve closes and the pressure decreases the phase matching conditions become better again until the best phase matching conditions are achieved (second maximum). At this second maximum the valve remains closed and the pressure further decreases to zero, thus the harmonic yield drops down to zero, too. In figure 4.11(a) the curves show a different starting point, which is not the case in figure 4.11(b). The explanation is that the gas valve shows fluctuations in time the nozzle is supposed to open. For higher backing pressures these fluctuations disappear.

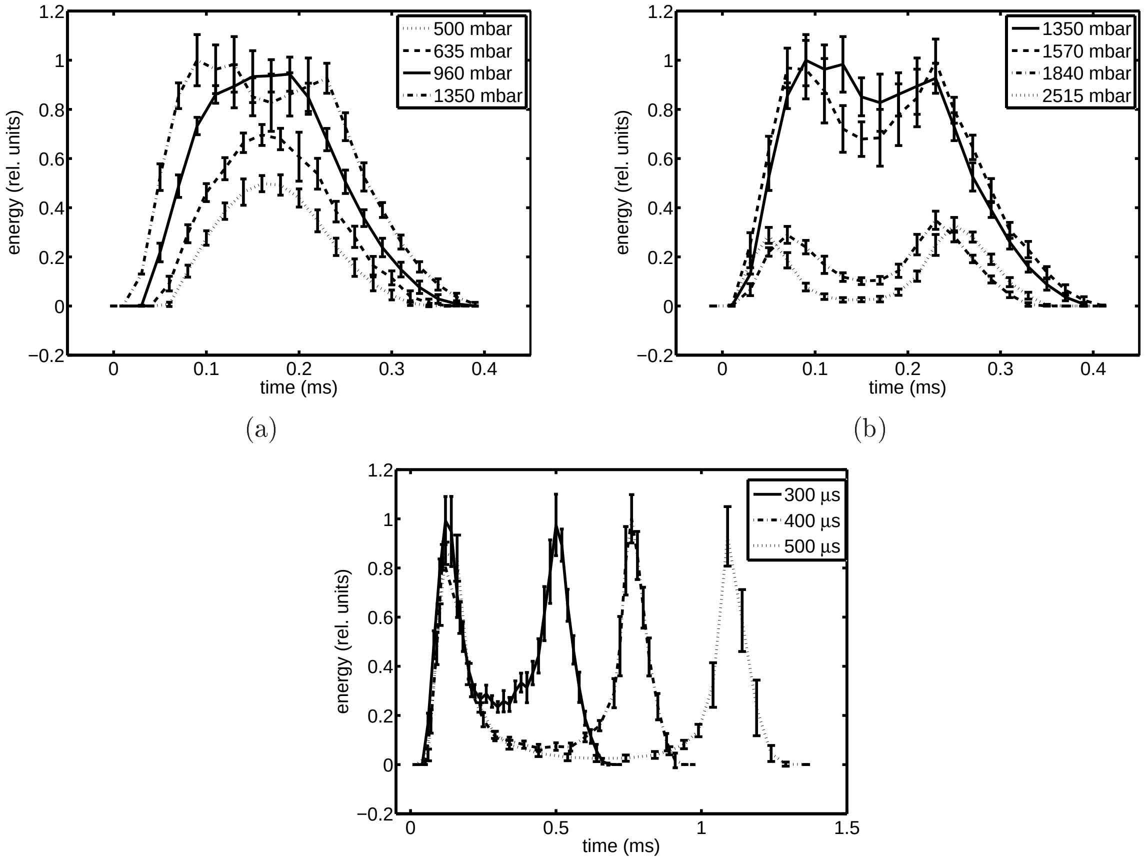

(a)

(b)

(c)

Figure 4.11: Pressure dependent yield of H21 for $f_{NIR} = 1500$ mm. Figure 4.11(a) and 4.11(b) show the time dependence for different backing pressures for an opening period of $t = 200$ µs of the valve, where figure 4.11(c) shows the time dependence for different opening periods and a constant backing pressure $p = 635$ mbar of the gas valve. In all cases the harmonic energy is measured for different time delays between the gas- and the laser-pulse. Each series of measurement is then composed of those individual measurements.

For vacuum technical reasons the gas load must not exceed a certain threshold. The pressure of the last vacuum chamber in the pit has to be below $1 \cdot 10^{-6}$ mbar, otherwise a valve in front of the electron vacuum closes. Therefore the opening period of the gas valve has to be reduced as much as possible. In figure 4.11(c) the H21 yield is shown for different opening times of the gas valve and for a constant backing pressure. The maximal yield is independent of the pulse width of the gas valve. However, the decrease of the yield in between the two occurring peaks becomes stronger for longer gas pulses and the time interval between the two respective peaks becomes larger. The reason is that for longer gas pulses the pressure exceeds the optimal condition further than in case of shorter gas pulses and a longer time is needed to reduce the pressure within the target to the optimal value again. The smallest opening period of the nozzle is 200 µs. A further decrease of the opening period is therefore not possible.

Fundamental laser intensity

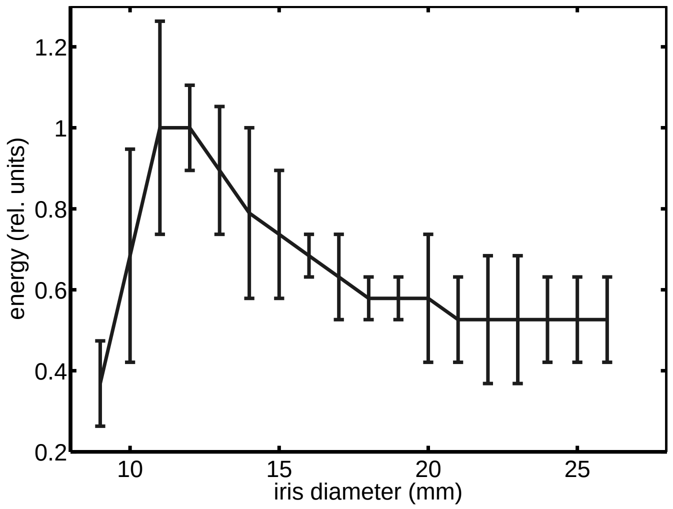

Figure 4.12: H21 yield dependent on the driving laser intensity ($f_{NIR} = 1500$ mm).

Another crucial parameter for the H21 yield is the intensity of the driving laser. The intensity is adjusted by changing the diameter of the iris in front of the focusing mirror. Figure 4.12 shows the H21 yield for different diameters of the used iris, acquired with the XUV CCD. After a steep slope the highest yield is achieved at ≈ 11 mm. Then a decrease of the yield appears until an iris diameter of ≈ 21 mm. Efficient HHG occurs at a certain intensity as explained in chapter 2.3. For higher intensities the phase mismatch becomes larger and the yield drops down. Because the beam diameter is limited by the smallest used optic of 25.4 mm a further increase of the iris diameter is not meaningful. The obtained plateau between 21 mm and 25 mm is due to a fundamental laser diameter of 21 mm.

In contrast to the method described above it is also possible to change the intensity by changing the pulse energy in front of the iris by tuning the amplifier. The higher the pulse energy in front of the iris, the smaller is the optimal diameter of the iris to achieve the same intensity. For seeding purposes it is favorable to have a high photon flux, rather than just a high CE, thus the harmonic energy should be concentrated in a cone as small as possible. In addition a long Rayleigh length of the harmonics is favorable. For a small iris the beam waist of the driving laser becomes larger, the Rayleigh length becomes larger, and the divergence gets smaller compared to a larger iris. Assumed that the properties of the driving laser are to some extent transferred to the harmonics, a smaller iris in combination with a high pulse energy seems to be the optimal operation mode for seeding purposes. A further discussion on the optimal HHG operation mode for seeding purposes can be found in chapter 4.4.

Target length

The target length is another parameter which has an impact on the harmonic yield. During this work different targets, i.e. a free propagating gas jet, as well as gas channels of different lengths and diameters have been investigated to increase the total harmonic yield. In figure 4.13 the yield for different target geometries is plotted (details of the targets can be found in chapter 3.2.2). The free propagating gas jet has the smallest yield. This can be explained in terms of the interaction length. The interaction region is on the one hand defined by the spot size of the laser and on the other hand by the gas profile. In case of the free propagating jet the limiting factor is the gas profile. In collaboration with A. Willner and F. Tavella the gas profile of the free propagating jet has been investigated in terms of an interferometric measurement of the gas density [Benattar et al., 1979; Ditmire and Smith, 1998; Yu et al., 2004]. The result is shown in figure 4.14. It turned out that for a backing pressure of $p(\mathrm{Ar}) = 6$ bar the gas density drops down from $3 \cdot 10^{19}$ cm^{-3} to $1 \cdot 10^{19}$ cm^{-3} within 400 µm axial distance to the exit of the nozzle. Thus, the effective interaction length is too small to achieve a high CE.

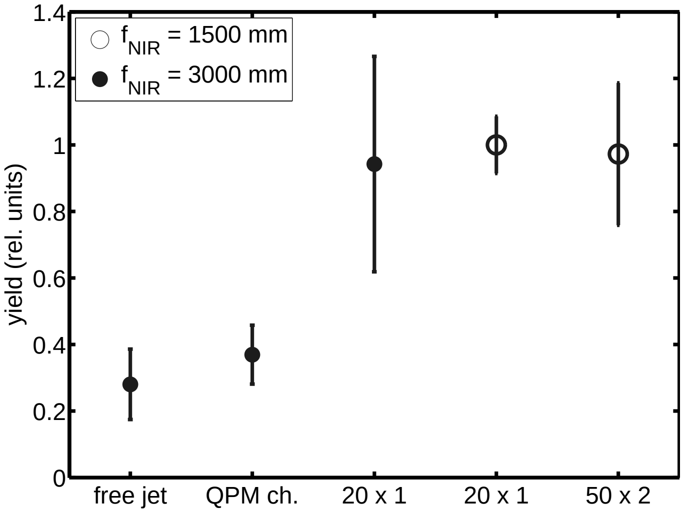

Figure 4.13: Yield of different target geometries and different focal lengths of the driving laser.

Aside from the QPM target, all the different argon channels, independent of the focal length achieve similar pulse energies, although the specific optimal settings for HHG had to be changed. In case of the 20x1 argon channel, the backing pressure was set to approximately 3100 mbar for the $f_{\mathrm{NIR}} = 3000$ mm geometry, whereat for a focus geometry of $f_{\mathrm{NIR}} = 1500$ mm the pressure had to be reduced to approximately 1000 mbar. This can be explained as follows: for a smaller focal length the intensity at the position of the

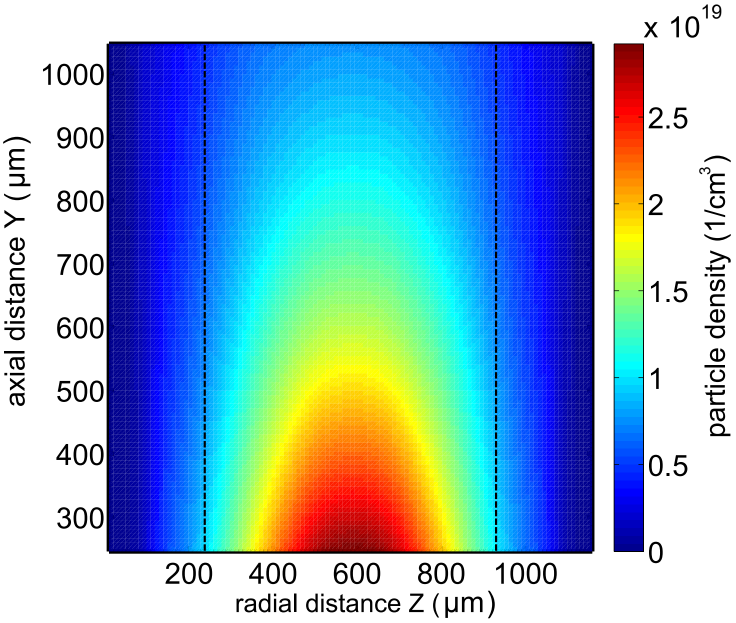

Figure 4.14: Measured target density of the gas valve, where Z corresponds to the radial and Y to the axial distance to the nozzle. The dashed lines correspond to the nominal diameter of the nozzle.

gas valve increases, thus the number of free electrons increases as well. In order to avoid a phase mismatch introduced by free electrons, either the intensity or the target pressure has to be reduced. This explanation can be applied to the case of $f_{NIR} = 1500$ mm and the two argon channels 20x1 and 50x2 as well. A longer target length, i.e. a longer argon channel leads to a higher ionization rate (in case all other parameters are kept constant). To avoid a phase mismatch the intensity has to be reduced again. For the 50x2 geometry, the highest CE was achieved by reducing the diameter of the iris and keeping the gas pressure constant. In [He et al., 2009] the H21 yield as a function of the target length is experimentally investigated. It turned out that for a similar laser system the optimal target length is also 20 mm.

In [Pirri et al., 2008] it is presented that an array of gas jets enhances the yield of specific harmonics. The QPM enhancement depends on the harmonic order and on the periodicity of the gas jets. Based on the presented results a simple array of argon jets has been designed as explained in chapter 3.2.2. Unfortunately, it was not possible to further enhance the CE as shown in figure 4.13 as well.

As explained before, a high CE is desirable, but not sufficient. For seeding purposes a rather high flux is necessary. Thus, the most promising setup is the case of $f = 1500$ mm in combination with the 50x2 target to provide a seed with a small divergence in combination with the highest achieved energy, as well as a low gas load.

XUV-CCD

For the determination of absolute photon numbers a XUV CCD camera is installed in the diagnostic section as explained in chapter 3.3.4. To calculate the absolute photon number at the position of the gas target some assumptions have to be made. Firstly, the reflectivity of the used XUV optics has only been measured for the grazing incidence mirrors. Two triplet systems, i.e. six grazing incidence and two multilayer mirrors are employed to steer the beam to the CCD. Furthermore, the theoretical reflectivity of the multilayer mirrors as published in [Lawrence Berkeley National Laboratory, 2011] is not in agreement with calculations based on IMD [Windt, 1998]. Additionally, the driving laser has damaged the first mirror of the first triplet system, due to the high intensity. In figure 4.15 the damage of the triplet is imaged with the zeroth order in the spectrometer for different triplet positions. [Nguyen et al., 2011; Allison, 2010] reported that the XUV reflectivity decreases in time. It is assumed that this abatement is due to oxide growth or carbon contamination. Secondly, the transmission of the used aluminum filter depends on the aluminum oxide layer which can only be estimated (chapter 3.3.3). At last, the stray light apertures clip a small part of the harmonics. All these effects enlarge the uncertainty of the deduced pulse energy. However, a lower limit can be calculated and an appropriate error can be estimated. A transmission $T = 0.014 \pm 0.008$ of the beamline to the CCD is estimated in chapter 3.3.2. The stray light apertures and the limited size of the CCD chip reduce the energy for $f_{NIR} = 3000$ mm by another estimated 30% as illustrated in figure 4.8(a). Hence, the total transmission is assumed to be

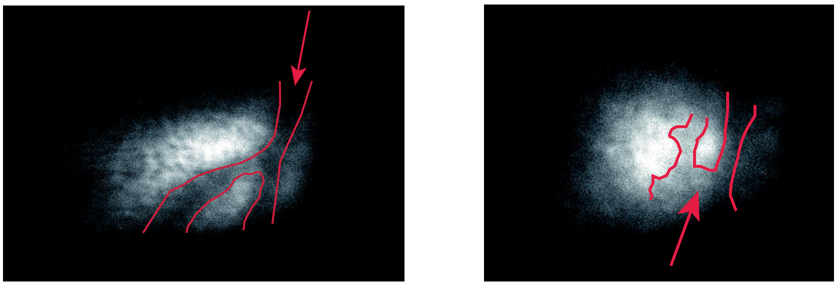
(a) (b)

Figure 4.15: The damage of the triplet is imaged with the zeroth order in the spectrometer for different positions of the first triplet mirror system.

$$T_{tot} = 0.010 \pm 0.005$$

In combination with the quantum efficiency of the CCD chip a lower limit of the generated H21 energy can be calculated. The damage of the triplet is not considered.

$$E_{H21} > (0.23 \pm 0.12)\ \text{nJ}$$

XUV diode

In order to measure absolute photon numbers besides the XUV-CCD camera, a XUV photodiode has been employed (chapter 3.3.4), too. In cooperation with J. Bödewadt the diode has been set up and commissioned. Here the detected signal is amplified and visualized on a fast scope. Details regarding the technical performance and the written software environment can be found in apendix C.

Based on the fact that

$$U_{\mathrm{diode}} = RI_{\mathrm{diode}}$$

the charge Q_{diode} can be calculated. $U_{\mathrm{diode}}(t)$ is the voltage, R the resistance, and $I_{\mathrm{diode}}(t)$ the current.

$$Q_{\mathrm{diode}} = \int I_{\mathrm{diode}}(t)dt = \frac{1}{R}\int U_{\mathrm{diode}}(t)dt = N_e e \tag{4.4}$$

where N_e is the number of electrons obtained at the diode and e the elementary charge. The number of photons at each harmonic order N_q can be calculated with the equation

$$N_e = \sum_q \eta_q t_q N_q, \tag{4.5}$$

where η_q is the quantum efficiency of the diode and t_q the transmission coefficient of the aluminum filter [He et al., 2009]. All harmonic orders smaller than 11 are being suppressed by the aluminum filter (figure 3.14(a)). Additionally, the pulse energy of each harmonic order $q \geq 9$ is assumed to be the same (plateau).

$$E_q = N_q h\nu_q = E = \mathrm{const}, \tag{4.6}$$

where h is Planck's constant and ν_q the harmonic frequency. The average pulse energy of each harmonic order can be calculated with equation 4.4, 4.5, and 4.6:

$$E = \frac{Q_{\mathrm{diode}} h}{e \sum_q \frac{\eta_q t_q}{\nu_q}}.$$

The transmission coefficients t_q of the 200 nm aluminum filter depend on the thickness of the Al_2O_3 layer on both sides and is as in case of the XUV-CCD assumed to be $2 \cdot 6$ nm (chapter 3.3.3). Thus, the corresponding calculated energy leads to a lower lower limit:

$$E_{21} > (1.4 \pm 0.4)\ \mathrm{nJ}.$$

Here, the optimal conditions for maximal H21 energy as explained in the beginning of this chapter have been set up prior to the measurement. The given error corresponds to the statistical error of the measurement and is calculated in terms of error propagation. In chapter 4.3.3 will be shown that the shape of the spectrum is changed by tuning the HHG process to the maximum yield of H21. Therefore, the approach of equation 4.6 is strictly speaking not valid and the pulse energy of H21 is larger than 1.4 nJ.

A different approach to calculate the H21 energy without assuming an energy plateau is assuming a plateau of the generated photon numbers. Here, the signal of each harmonic order consists of the same number of photons. The quantum efficiency of the diode is known for all harmonic orders. In combination with an assumed average transmission of $T_{Al} = t_q = 30\% \pm 15\%$ through the aluminium filter the contribution of the 21^{st} harmonic can be calculated. Employing equation 4.4 and 4.5 the total number of photons, i.e. the energy of H21 is then calculated to

$$E_{H21} > (2.4 \pm 1.2)\text{ nJ}.$$

This result is roughly twice as big as the previous analysis, although the only differences are, that an energy-plateau of the harmonic spectrum is not taken into account as well as an assumed average transmission of all contributing harmonic orders. A detailed analysis of the harmonic spectrum in argon and similarly a justification that the spectrum can be tuned to the 21^{st} harmonic will be performed in chapter 4.3.3. It will be shown that it is possible to change the shape of the spectrum to a maximal yield in the 21^{st} harmonic and smaller yields for higher and lower harmonics. Furthermore, the reflectivity of the B_4C triplet mirrors varies slowly with the wavelength (chapter 3.3.2), thus a deconvolution of the spectrum is not necessary. In addition, the aluminum transmission of 30% is an upper limit, due to the unknown aluminum-oxide layer.

HHmeter

With the HHmeter a third method to determine absolute photon numbers is employed. In principle the harmonics ionize the residual gas and the corresponding ions are measured as explained in chapter 3.3.4. In figure 4.16(a) a typical signal is shown. The peaks correspond to the ionized residual gas and the amplitude depends on the according partial pressure, thus the signal differs from day-to-day. Hence, this method is not applicable on a daily basis. In figure 4.16(b) the arrival time of ions as a function of the mass is plotted. The plot shows that the acquired peaks in figure 4.16(a) correspond to hydrogen, helium, nitrogen/oxygen, and argon. The arrival time t itself depends on the voltage and the distance x of the harmonics to the detector [Jackson, 1999]:

$$\begin{aligned} Q \cdot U &= \frac{1}{2} m \left(\frac{dx}{dt}\right)^2 \\ Q \cdot E &= m \cdot a \\ \text{with} \qquad E &= \frac{U}{d}, \end{aligned}$$

where Q is the charge, U the voltage, m the mass, $\frac{dx}{dt}$ the velocity, E the electric field, a the acceleration, and d the distance. The ratio between a single photon event S_{spe} and the full signal S_{signal} corresponds to the number of events, i.e. the the generated ions in front of the detector. To measure S_{spe}, the intensity of the fundamental laser is reduced to an argon signal which is slightly greater than noise. If the signal of a single photon

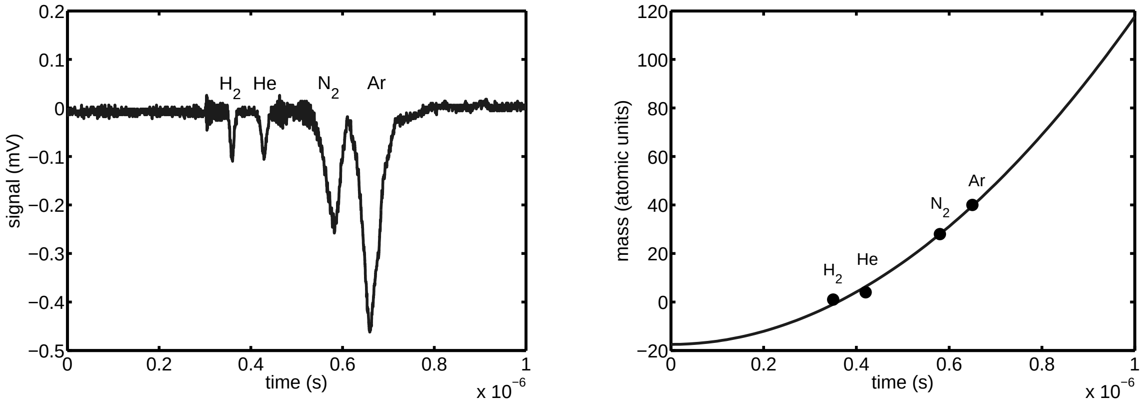

(a) (b)

Figure 4.16: HHG signal detected with the HHmeter. Figure 4.16(a) corresponds to the signal caused by ionized hydrogen, helium, nitrogen/oxygen, and argon. Figure 4.16(b) shows the arrival time of ions as a function of the mass. The black dots correspond to hydrogen, helium, nitrogen, and argon.

event is smaller than noise, it was not possible to confirm the involvement of only one photon. Thus, this method again gives a lower limit of the H21 energy.

$$N_{ions} \geq \frac{\int S_{signal} dt}{\int S_{spe} dt}$$

On the other hand the number of ions is proportional to the number of photons N_{ph}

$$N_{ions} = \zeta_{Ar} \cdot N_{ph}, \tag{4.7}$$

where ζ_{Ar} is the probability of a photon to ionize the residual argon gas. ζ_{Ar} itself depends on the argon cross section σ of the corresponding photon energy and the number of argon atoms N_{Ar} within the interaction volume:

$$\zeta_{Ar} = \frac{A_{Ar}}{A_0} = \frac{N_{Ar} \cdot \sigma}{A_0}, \tag{4.8}$$

where A_0 is the spot size of the harmonics at the HHmeter. The number of argon atoms can be calculated with the ideal gas law [Feynman, 1963]:

$$N_{Ar} = \frac{pV_0}{k_B T} = \frac{plA_0}{k_B T}, \tag{4.9}$$

where p is the pressure, V_0 the interaction volume, l the length of the interaction volume, k_B Boltzmann's constant, and T the temperature. The number of photons can be calculated with equation 4.7, 4.8, and 4.9:

$$N_{ph} = \frac{k_B T}{\sigma p l} \cdot N_{ions}$$

In order to deduce the number of photons within the 21^{st} harmonic out of the total number of harmonic photons an energy-plateau is assumed and can be described with equation 4.6. The total number of photons N_{tot} can further be described as

$$N_{tot} = \sum_q N_q \qquad \text{with } q \in 11, 13, 15 \ldots 29, \tag{4.10}$$

where q is the contributing harmonic order. The approaches 4.6 and 4.10 lead to a total cross section σ_{tot}

$$\begin{aligned} \sigma_{tot} &= \sum_q c_q \sigma_q \qquad \text{with } q \in 11, 13, 15 \ldots 29, \\ \text{with} \quad c_q &= \frac{1}{\sum_i \frac{\lambda_i}{\lambda_q}} \qquad \text{with } i \in 11, 13, 15 \ldots 29 \end{aligned}$$

and σ_q the argon cross section for the q^{th} harmonic order. The number of photons within the 21^{st} harmonic can then be calculated:

$$N_{ph,H21} = c_{21} \frac{k_B T}{\sigma_{tot} p l} \cdot N_{ions} \tag{4.11}$$

The uncertainty of the result depends mainly on the uncertainty of S_{spe}, i.e. the signal of a one photon event. The resulting error of N_{ions} has been determined to be $\Delta N_{ions} \leq 15\% \cdot N_{ions}$ and leads to

$$E_{H_{21}} > (0.51 \pm 0.08) \text{ nJ},$$

where the error is calculated in terms of error propagation. The quoted energy is still a lower limit, because the number of photons within each harmonic is not modulated with the spectrum. As explained in the previous section an energy-plateau of the harmonics has been assumed, although the spectrum is tuned in a way that the 21^{st} harmonic becomes favored (chapter 4.3.3). In order to calculate the number of photons without assuming an energy-plateau, an average argon cross section of the harmonics has to be calculated:

$$\bar{\sigma} = \frac{\sum_q \sigma_q}{10} = 18.6 \text{ Mb} \qquad \text{with } q \in 11, 13, 15, \ldots 29.$$

Equation 4.11 can then be simplified to:

$$N_{ph,H21} = \frac{k_B T}{\bar{\sigma} p l} \cdot N_{ions} \frac{\sigma_{21}}{\sum_q \sigma_q} \qquad \text{with } q \in 11, 13, 15, \ldots 29$$

where σ_q is taken from table 3.2. The corresponding energy of H21 is calculated to:

$$E_{H_{21}} > (14.9 \pm 2.2) \text{ nJ},$$

and is a factor of 30 larger. The difference shows that the assumption of a plateau has a major impact on the calculated energy. The following chapter 4.3.3 will show that the optimization procedure will cause a spectrum without the typical plataeu, thus the equation 4.6 is not valid. Besides, both methods do not employ an aluminum filter in front of the detector, thus also harmonics with $q < 11$ as well as the driving laser might contribute to the ionization process. Unfortunately cross sections for photon energies ≤ 16 eV are not available [Becker and Shirley, 1996]. The use of an aluminum filter in front of the HHmeter is due to the high driving laser intensity and the low damage threshold of the filter not possible.

The electron binding energy of argon in [CXRO, 2009] for the 3p subshell is $E_{3p} \approx 15.8$ eV, whereat the energy of H21 photons is $E_{H_{21}} = 32.5$ eV. In order to investigate the sensitivity on the residual gas, helium with a binding energy of $E_{1s} = 24.6$ eV [CXRO, 2009] has been provided to the vacuum chamber. In figure 4.17 the single-shot correlation between the argon- and helium HHmeter signal is shown for different z-positions of the gas target relative to the laser focus, i.e. different phase matching conditions for different harmonics. It is shown that the signal of argon correlates with the signal of helium, thus the HHmeter signal does not depend on the type of the residual gas.

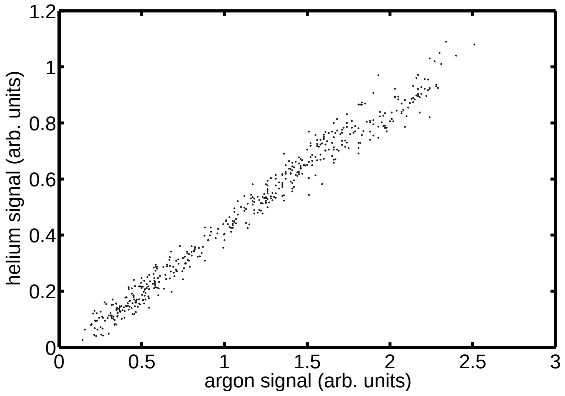

Figure 4.17: Correlation of the harmonic generation signal detected with the HHmeter between argon and helium.

The CCD, the photodiode, and the HHmeter have been employed to measure the energy of the 21st harmonic and are summarized in table 4.2. The employed methods are independent of each other and it has been shown that different reasonable assumptions lead to a huge difference in the resulting H21 energy. Nevertheless, the calculated energy is a lower limit and in the order of a few nanojoules. The used energy of the driving laser corresponds to approximately 10 mJ and a CE of $2 \cdot 10^{-7}$ is calculated for a pulse energy of 2 nJ and a transmission of 30% through the aluminum filter.

4.3.3 Harmonic spectrum - plateau and cutoff

The influence of several parameters on the HHG spectrum will be shown in this chapter. Figure 4.18 shows a typical single shot spectrum of harmonics generated in argon. The horizontally separated vertical lines represent odd multiple of the frequency of the driving

Table 4.2: Energy of H21 determined with different methods and different detectors

detector	method	uncertainty	energy
XUV CCD	H21 selected by multilayer	beamline transm., Al_2O_3 thickness, damage triplet, stray light iris,	$> (0.23 \pm 0.12)$ nJ
XUV diode	energy plateau	Al_2O_3 thickness	$> (1.4 \pm 0.4)$ nJ
XUV diode	without energy plateau	Al_2O_3 thickness	$> (2.4 \pm 1.2)$ nJ
HHmeter	energy plateau	contrib. harmonics	$> (0.5 \pm 0.1)$ nJ
HHmeter	without energy plateau	contrib. harmonics	$> (15 \pm 2)$ nJ

laser. According to section 4.2 a spectrum can be deduced by binning the pixel values in the vertical direction. Note that the harmonics are slightly tilted. As a consequence, binning the pixel values leads to a broadening of the individual harmonics. A proper determination of the harmonic bandwidth is therefore not possible. Although it is not possible to calculate absolute photon numbers the relative magnitude of each harmonic can be determined.

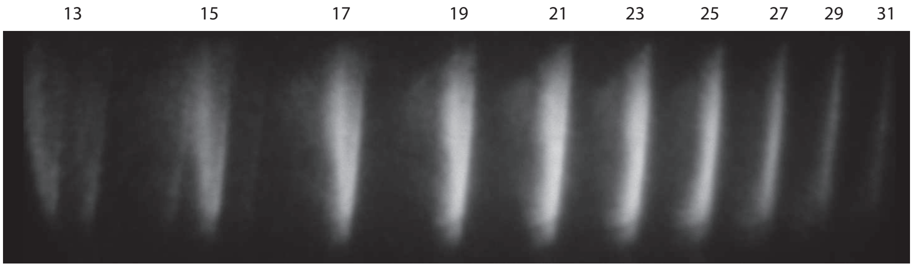

Figure 4.18: Singleshot HHG spectrum (harmonic order marked on top).

A number of parameters have an influence on the phase matching conditions as explained in chapter 2.3.3. Therefore, the harmonic source is set up in a way that the yield of the 21^{st} harmonic is maximized regardless of the other harmonic orders. That is, why all of the following plots show spectra with a maximal yield of the 21^{st} order, i.e. 32.5 eV or 38.1 nm. In addition all spectra are modulated with the transmission of the XUV beamline, i.e. the wavelength dependent reflectivity of the XUV optics between the generation and measurement of the harmonics (chapter 3.3.2). Another modulation of the spectrum is the wavelength dependent reabsorption as explained in chapter 3.3.4, hence the typical plateau of the HHG spectrum is absent in the following spectra.

In figure 4.19 the influence of the NIR focal length on the spectrum is shown. In both cases the harmonics are generated in a free propagating gas jet of argon with a backing pressure of 6.7 bar. However, the recorded spectra show a different shape of the harmonic comb and a different cutoff. According to equation 2.14 the cutoff depends on the driving

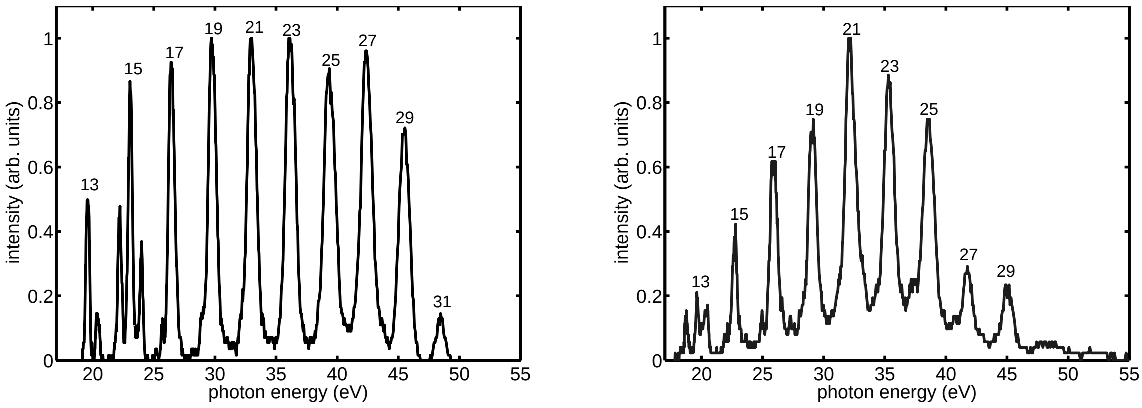

(a) (b)

Figure 4.19: High harmonic generation spectra without an aluminum filter for $f_{NIR} = 750$ mm in figure 4.19(a) and $f_{NIR} = 3000$ mm in figure 4.19(b)

laser intensity at the target position. As the laser intensity increases with a decreasing focal length the cutoff in figure 4.19(b) has to be at lower energies compared to figure 4.19(a).

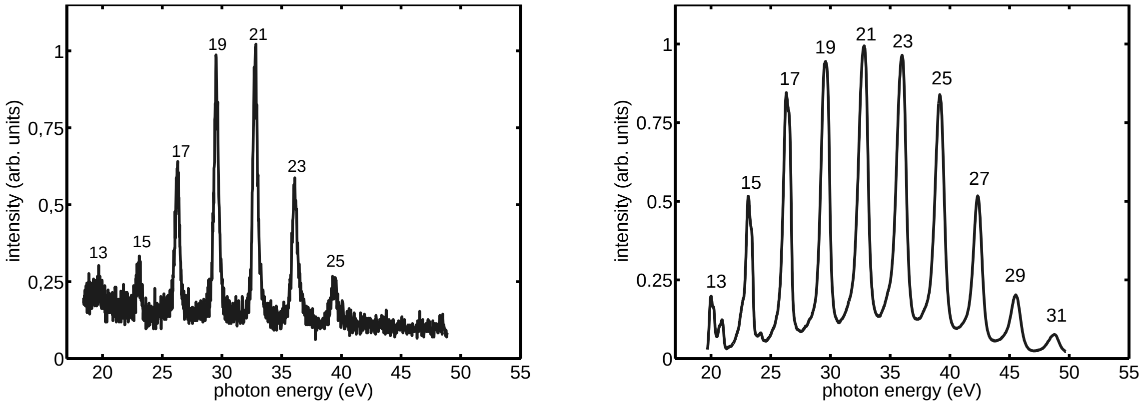

(a) (b)

Figure 4.20: HHG spectra with $f_{NIR} = 3000$ mm and a pulse length of a few hundred femtoseconds in figure 4.20(a) and 35 fs in figure 4.20(b).

Figure 4.20 shows the effect of different NIR pulse lengths with a constant focal length of $f_{NIR} = 3000$ mm and a aluminum filter in front of the spectrometer. On the one hand a shorter pulse length of the driving laser leads to a higher intensity used for HHG, i.e. an extended cutoff behavior of the spectrum. On the other hand the yield, thus the CE can be enhanced with shorter driving laser pulses. Note, both spectra are normalized, but the signal-to-noise ratio is much better in figure 4.20(b).

The bandwidth of each harmonic depends on the intensity of the driving laser as explained for example in [He et al., 2009]. In addition to this spectral broadening the phase matching conditions for the long trajectory of the HHG process become more favorable and interference fringes within one harmonic emerge [Xu et al., 2008; Brunetti et al., 2008; Zaïr et al., 2008]. The double-peak structure observed in H13 and in H15 of figure 4.19(a) can be explained in terms of destructive interference between the long and short quantum path. In figure 4.19(b) those fringes do not occur in H15 and are only slighly pronounced in H13, due to the lower intensity of the driving laser. The short trajectory is predominant at moderate laser intensities [Salières et al., 1998] and leads to harmonics with a lower divergence compared to the long trajectory [He et al., 2009]. On the other hand the yield of the harmonics depends on the laser intensity. In chapter 4.3.2 it is shown that efficient generation of the 21st harmonic is only achieved for a small parameter range, i.e. driving laser intensity, target position, target pressure, and target length.

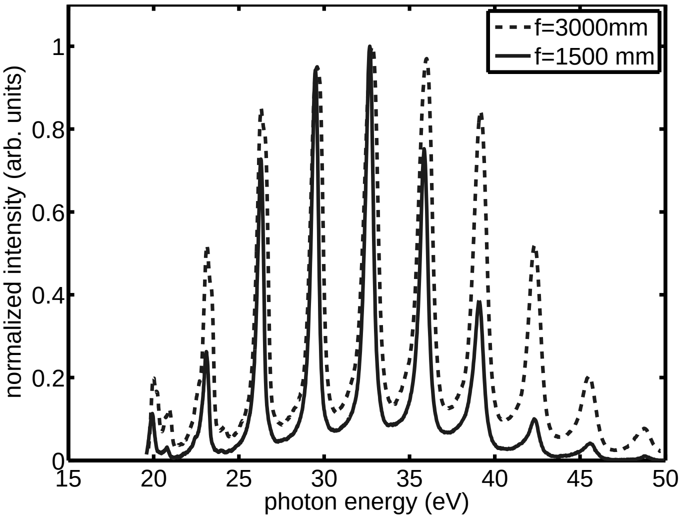

Figure 4.21: Optimized HHG spectrum for $f_{NIR} = 1500$ mm and $f_{NIR} = 3000$ mm. The intensities are normalized to the H21 signal.

The two spectra in figure 4.21 are generated in a 20 mm argon channel and correspond to a focal length of $f_{NIR} = 1500$ mm and $f_{NIR} = 3000$ mm. The driving laser intensity, target position, target pressure, and target length are optimized to the maximal yield of H21. In case of $f_{NIR} = 1500$ mm the iris is reduced to 11 mm diameter, the target is located 33 mm in front of the focus (figure 4.2(a)), and the target backing pressure was set to 1000 mbar. In case of $f_{NIR} = 3000$ mm the iris was completely opened, the target position was located at $z = 150$ mm (figure 4.2(b)) which corresponds to a distance of $\Delta z = 77$ mm to the focus in x- and $\Delta z = 53$ mm in y-direction, and the target backing pressure was set to 3100 mbar. The corresponding intensities are approximately $I_{3000} = 3.4 \cdot 10^{14}$ W/cm^2 and $I_{1500} = 2.4 \cdot 10^{14}$ W/cm^2 for $f = 3000$ mm and $f = 1500$ mm, respectively. This also explains the earlier cutoff in case of $f_{NIR} = 1500$ mm compared to the $f_{NIR} = 3000$ mm focus geometry.

Note that for both focus geometries the target intensity and the nominal f/# number are comparable ($f/\#_{3000} = 143$, $f/\#_{1500} = 136$). Thus, the target conditions for HHG are comparable and it is reasonable that the absolut yield of the 21st is the same in both cases. It is further shown that for a smaller focal length the phase matching conditions cannot be fulfilled as good as for a larger focal length in all orders, simultaneously. However, both spectra show narrow harmonic peaks without a double peak structure, hence the short trajectory is dominant. Thus, this operation mode is optimal for seeding applications.

4.3.4 Wavefront

The wavefront of the 21st harmonic, as well as the impact of the wavefront on seeding has been investigated in [Hipp, 2010]. The wavefront sensor was constructed according to the Hartmann principle [Hartmann, 1900; Shack and Platt, 1971] and was set up in the diagnostic section of the HHG laser lab (chapter 3.3). The images have been acquired using a XUV CCD with an exposure time of 1 s, i.e. the determined wavefront corresponds to an average of ten H21 laser pulses. Note that two multilayer mirrors are employed, thus only the 21st harmonic is transmitted to the wavefront sensor. For the analysis the measured wavefront has been fitted to the fundamental mode of a Gaussian pulse characterized as follows

$$\begin{aligned} W_0 &= 23.3\ \mu\text{m} \\ z_R &= 45\ \text{mm}, \end{aligned}$$

where W_0 is the beam waist of the virtual source and z_R is the Rayleigh length. Based on these results the beam quality factor M^2 as well as the beam size w at the gas target have been calculated. The analysis leads to $11.6 \leq M^2 \leq 30$ and a beam size of $W_x = (849 \pm 80)\ \mu\text{m}$, $W_y = (660 \pm 80)\ \mu\text{m}$ at the position of the gas target. Unfortunately this cannot be true, because the laser has a diameter of less than $300\mu\text{m}$ as described in section 4.1.2. Thus, this work again suffers from the mirror mounts as explained in section 4.3.1.

4.3.5 Stability

The shot-to-shot stability of HHG depends mainly on the stability of the driving laser, due to the nonlinear nature of the HHG process. During this work the stability of the pulse energy has been investigated. It turned out that for a stability of $\sigma_{\text{NIR}} \approx 5\%$ (rms), which is a fairly good value for a 10 Hz laser system, a stability of $\sigma_{\text{H21}} \approx 25\%$ (rms) can be achieved. In case of $\sigma_{\text{NIR}} \geq 8\%$ (rms) the harmonic source cannot be optimized sufficiently, due to the huge shot-to-shot fluctuations of the corresponding signal. Hence, the laser has to be tuned carefully to $\sigma_{\text{NIR}} \leq 5\%$ (rms). On a long term the harmonic source looses approximately 10% output power in the 21st harmonic after 24 operating hours. This is due to laser drifts and can be compensated by readjusting the source.

4.3.6 Quasi phase matching

Due to the tight commissioning schedule of sFLASH further developments of the HHG source lack of time. That is why advanced techniques to increase the CE could not be investigated thoroughly. Nevertheless, QPM is a promising way to increase the CE. It is based on the well known principle in nonlinear optics [Armstrong et al., 1962; Fejer et al., 1992]. In literature different methods of QPM HHG have been proposed [Paul et al., 2003; Zhang et al., 2007; Seres et al., 2007]. In order to develop a HHG source for FLASH II, Arik Willner and Franz Tavella are working on QPM targets. A first design of a QPM target has been realized and was implemented into the target chamber of the sFLASH HHG source. The QPM target consists of alternating gas targets of argon and hydrogen in order to compensate the phase mismatch introduced by only one gas target. The successive sources are tuned in a way that the corresponding harmonics add constructively. A detailed description of the development and a detailed description of the results can be found in [Willner, 2011], a schematic representation, however, is shown in figure 4.22.

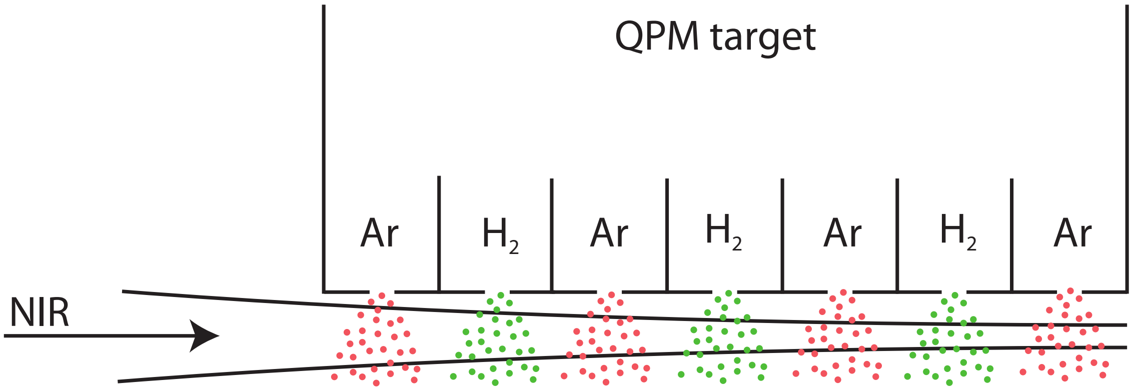

Figure 4.22: Schematic representation of QPM: the target consists of alternating argon and hydrogen gas jets. Hydrogen is employed to reverse the dispersion introduced by argon.

In figure 4.23 the QPM effect of hydrogen on HHG is shown. The plotted data correspond to single-shot harmonic intensities generated with and without hydrogen ($f_{NIR} = 3000$ mm, $p(\text{argon}) = 5400$ mbar, $p(\text{hydrogen}) = 2000$ mbar). It is clearly visible that hydrogen increases the harmonic intensity, although there are many shots where an increase of the harmonic intensity is not realized. The quasi phase matched target has been developed for a kilohertz laser system and was not intended to work in a pulsed mode as used in this work. Thus, the optimal QPM conditions could not be established, but an increase of the CE due to the QPM effect has still been observed for 10% of the series of measurement. In our case the total efficiency yields to an energy of a few picojoule in the 21^{st} harmonic. The highly efficient regime of QPM cannot be realized with the used target, because the needed target pressure in combination with the available driving laser intensity cannot be established. The resulting gas load exceeds

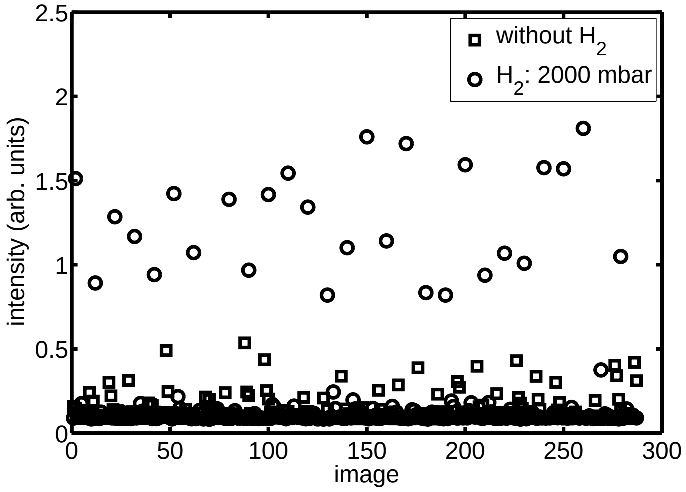

Figure 4.23: Effect of hydrogen on quasi phase matched HHG

the given thresholds for an operation with FLASH as explained in chapter 3.2.2 and the backing pressure had to be reduced in order to keep the vacuum conditions fulfilled.

In conclusion a QPM target seems to be a possible method to further increase the harmonic yield, although the available target does not work for sFLASH. The target has to be developed especially for a 10 Hz laser system in combination with the ultra-high vacuum conditions of FLASH.

4.3.7 Two color high harmonic generation

An alternative approach to QPM HHG is two color HHG. As in case of QPM HHG only a quick experiment has been performed. In figure 4.24 a schematic representation of

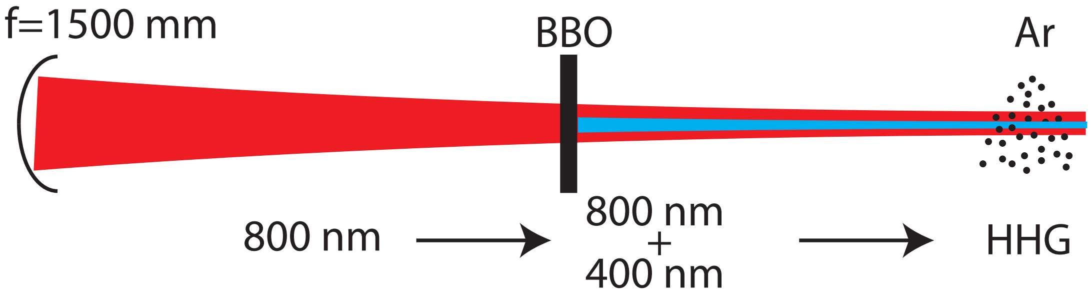

Figure 4.24: Schematic illustration of two color HHG

the realized two color HHG setup is shown. The experiment has been realized with the

$f_{\mathrm{NIR}} = 1500$ mm geometry and the beta barium borate (BBO) crystal was positioned at the z-position $z = 295$ mm in figure 4.2(a). The BBO (type I, 10x10x0.1 mm^3) is used to generate the second harmonic of 800 nm, in order to increase the CE as shown in [Kim et al., 2005; Lambert et al., 2009; G.Lambert et al., 2010].

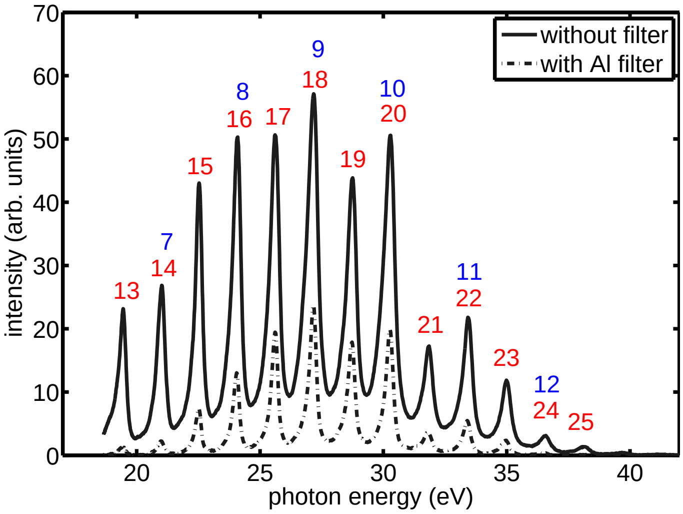

Figure 4.25: Two color HHG spectra where the numbers correspond to the harmonic order of the driving laser. Blue numbers correspond to a 400 nm and red numbers to a 800 nm driving laser. Here, the H21 energy is in the picojoule regime.

In figure 4.25 a recorded spectrum with a driving wavelength of $\lambda_1 = 800$ nm and $\lambda_2 = 400$ nm is shown. The harmonic peaks have a distance of 1.5 eV to each other and correspond to the odd and even harmonics of the 800 nm = 1.5 eV driving laser. The generation of even harmonics is explained with a symmetry break of HHG due to the second color [Lambert et al., 2009]. The early cutoff in the spectrum is due to an insufficient intensity of both driving laser wavelengths. The possible position of the BBO is limited, thus the tunability, i.e. the amount of the second harmonic is limited as well. In order to achieve an enhancement of the 21$^{\mathrm{st}}$ harmonic the possibility to tune the intensity of the second harmonic needs to be available [Popruzhenko et al., 2010; Lan et al., 2010]. Lately the wavelength dependence of HHG has been investigated [Falcao-Filho et al., 2009; Ishikawa et al., 2009; Falcao-Filho et al., 2010]. It turned out that the wavelength of the driving laser has a huge impact on the efficiency. In case of the 21$^{\mathrm{st}}$ harmonic an increase of up to one order of magnitude can be achieved for a driving wavelength of 400 nm instead of 800 nm [Falcao-Filho et al., 2010]. As in case of QPM HHG the boundary conditions of the sFLASH source are too much restricting. Further developments are necessary to achieve an absolute enhancement of the 21$^{\mathrm{st}}$ harmonic in terms of lower driving laser wavelengths or two color HHG.

4.4 Seeding FLASH

This section is addressed to the commissioning of sFLASH and summarizes the interaction of all sFLASH sections. The s-FLASH team has shown that all sections, i.e. the laser system, HHG, XUV beam transport, overlap of the XUV radiation and the electron beam, the sFLASH undulators, and the sFLASH diagnostics work as expected.

For a seeded operation of FLASH the laser system and the harmonic source have to be set up properly. So far, the best configuration of the high harmonic source is the following: the driving laser ($\mathsf{FWHM} = 13$ mm) is focused 33 mm behind the target with $\mathsf{f_{NIR}} = 1.5$ m. In addition the pulse energy of maximal 22.1 mJ is reduced in terms of an iris with 11 mm aperture. The harmonic target is 50 mm long and operated with a backing pressure of approximately 1000 mbar, in order to achieve the highest CE in combination with the lowest gas load. The spectrum shows narrow harmonics without interference fringes, thus the short trajectory with the smallest divergence and the highest spatial and temporal coherence is selected. Moreover, a lower limit of a few nanojoule has been measured for the 21^{st} harmonic.

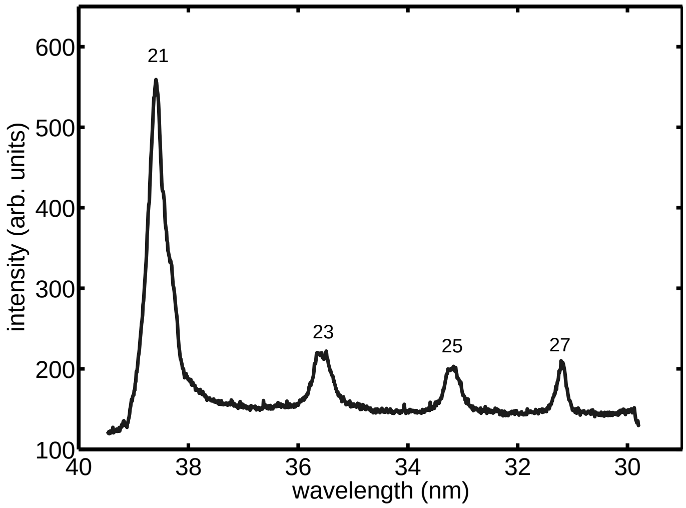

Figure 4.26: HHG spectrum acquired in the FLASH tunnel. Courtesy of F. Curbis, Lund University.

In parallel SASE has to be established with the sFLASH undulators. Furthermore, the central wavelength needs to match to the central wavelength of H21. This is done by adjusting the gaps of the undulators. Here the tunnel spectrometer is employed to ensure the overlap. In figure 4.26 the HHG spectrum acquired in the FLASH tunnel is shown with a peak intenstity at the 21^{st} harmonic. Note that between the generation and the detection of the harmonics four grazing incidence and one multilayer mirror are employed. The multilayer mirror has the highest reflectivity at the 21^{st} harmonic and a much smaller reflectivity for smaller wavelengths as shown in figure 4.6. Thus, a decrease of the intensity is expected for higher harmonic orders than H21. Larger wavelengths cannot be detected with the current configuration of the spectrometer. The spatial and temporal overlap is then adjusted as explained in chapter 3.1.2 and in [Bödewadt, 2011; Tarkeshian, 2011].

The seeded radiation should have a high intensity peak at 38.1 nm and a broader background due to SASE [Miltchev et al., 2008; McNeil et al., 2007a]. This could not be observed so far for the following reasons. On the one hand the generated energy of H21 is transported to the electron vacuum by four grazing incidence and one multilayer mirror. The power content of H21 is therefore reduced. On the other hand only discrete positions within the s-FLASH undulator section are available to measure the harmonic beam diameter, thus a large uncertainty of the Rayleigh length, the position and size of the beam waist is inevitable. The measurements indicate that independent of the focusing optic in the injection beamline only a fraction of H21 is coupled to the electron beam. An absolute measurement of the H21 energy is not available at this position and a realistic simulation of the seeding process is therefore not possible. However, the effective seed energy seems to be too low to initiate the seeding process before SASE develops. In order to reduce the SASE background the gaps of one or two undulators have been opened. Also the position of the opened undulators have been interchanged but the seeding signal could not be observed so far.

[Togashi et al., 2011] reported a low contrast ratio between the seeded FEL radiation and SASE, too. In order to identify the seeding signal Velizar Miltchev developed a software which is based on FEL statistics. This software calculates the distribution of the SASE radiation depending on the individual machine parameters. The measured radiation is then attributed either to SASE or to a seeded FEL mode. In case the radiation is most likely due to a seeded operation of FLASH the harmonics are switched off and the measurement is repeated. If the radiation is then still associated to a seeded FEL mode the machine has drifted. During the last seeding shift a few seeding candidates have been observed, although not reproducible.

In summary, the sFLASH team has successfully commissioned the sFLASH section. Seeding itself could not be observed so far and is still in commissioning. In parallel further developments are scheduled and are presented in chapter 5.

5 Conclusion

Free-electron lasers are light sources with unprecedented brilliance in the XUV and x-ray regime. Usually an FEL is operated in the SASE mode, thus erratic fluctuations in intensity and in the spectrum are inevitable. Moreover, the femtosecond light pulses show arrival time fluctuations, reducing the time-resolution of corresponding pump-probe experiments. Seeding an FEL with an external laser is a feasible method to overcome those limitations.

During this work a HHG source has been constructed, commissioned, and characterized, in order to seed FLASH with XUV laser pulses. The 21^{st} harmonic of a Ti:Sa driving laser which was selected to seed FLASH is characterized with a pulse energy of a few nanojoule. In addition, the divergence of the harmonic can be changed by different focusing geometries of the driving laser. It has been shown that the expansion of the spatial profile can be described with two divergences in x- and y-direction. Depending on the focal length of the driving laser the divergence in x direction can be adjusted to < 0.34 and < 0.56 mrad. The divergence in y direction is < 0.78 mrad in case of $f_{\mathrm{NIR}} = 1500$ mm.

In table 5.1 the specifications of the most efficient harmonic sources are summarized and compared to the harmonic source of this work. The table consists of different columns containing the used laser parameters and the resulting energy of the 21^{st} harmonic, as well as the deduced harmonic source power, the assumed aluminum-oxide thickness and the corresponding citation. The intensity I_{NIR} is either deduced or taken from the quoted citation. The exact intensity at the gas target cannot be deduced, because the position of the HHG source relative to the laser focus is generally not quoted. For the same reason the laser spot size and the high harmonic source size cannot be deduced accurately, too. However, it is shown that independent of the driving laser specifications the H21 energy depends mainly on the aluminum-oxide layer thickness. As described in chapter 3.3.3 the transmission T through the oxide layer scales with:

$$T(\Delta x) \propto \exp(-\eta \Delta z),$$

where Δz is the aluminum-oxide thickness, and η is a constant. In table 5.1 it is further shown that different groups expect a different oxide-layer thicknesses. However, during this work a $2 \cdot 6\,\mathrm{nm} = 12\,\mathrm{nm}$ aluminum-oxide thickness has been assumed, which is a rather conservative value in order to deduce a lower limit of the harmonic energy. Table 5.1 shows that for a larger expected oxide-layer thickness the CE of $2.5 \cdot 10^{-7}$ may increase more than one order of magnitude. For seeding purposes the harmonic power content within the cross section of the electron bunch should be as high as possible. Unfortunately, the size of the harmonic source is usually not known nor published. To this end, the source

Table 5.1: Published specifications of HHG in argon. Numbers labeled with $\dagger$ are deduced, while numbers with $*$ are measured. Both labeled numbers have been added and are not published within the citation. In all cases the aluminum-oxide layer thickness $\Delta\mathcal{L}$ is an assumption of the corresponding author and depends on the number of filters $\mathcal{N}$, as well as the thickness $\mathcal{T}$ on each side of the filter ($\Delta\mathcal{L} = 2 \cdot \mathcal{N} \cdot \mathcal{T}$). § refers to the corresponding chapter of this thesis. The table is sorted in terms of an ascending H21 energy.

E_{NIR} (mJ)	t_{NIR} (fs)	f_{NIR} (mm)	D_{NIR} (mm)	f/#	W_{NIR} (µm)	I_{NIR} ($10^{14}\cdot$ W/cm^2)	E(H21) (nJ)	CE (10^{-7})	P(H21) (nJ/mm^2)	oxide layer thickness (nm)	reference
0.6	35	1000			40	$3.4^\dagger$	1.2	20	$\leq 239^\dagger$		[Falcao-Filho et al., 2010]
6	35	1500	40	$38^\dagger$	$10^\dagger$	1.2	1.7	2.8	$\leq 5414^\dagger$		[Lambert et al., 2009]
10^*	33^*	1500	11^*	$136^\dagger$	§4.1.2	$2.4^\dagger$	2.5	2.5	$\leq 20^\dagger$	2x6=12	this work
22^*	33^*	3000	21^*	$143^\dagger$	§4.1.2	$3.4^\dagger$	2.5	1.1	$\leq 13^\dagger$	2x6=12	this work
10^*	33^*	1500	11^*	$136^\dagger$	§4.1.2	$2.4^\dagger$	5	5	$\leq 40^\dagger$	2x10=20	this work
10^*	33^*	1500	11^*	$136^\dagger$	§4.1.2	$2.4^\dagger$	10	10	$\leq 80^\dagger$	2x15=30	this work
5	60	2000	15	$133^\dagger$	$34^\dagger$	1.4	17.5	35	$\leq 4830^\dagger$		[Hergott et al., 2002]
8.8	40	2000					34	39		3x2x8=48	[Erny et al., 2011]
10^*	33^*	1500	11^*	$136^\dagger$	§4.1.2	$2.4^\dagger$	50	50	$\leq 400^\dagger$	2x25=50	this work
	40	2000	≤ 50	$\geq 40^\dagger$	$\geq 10^\dagger$		160			40	[He et al., 2009]
2.8	27	600				5	150 (E_{tot})			2x2x25=100	[Kim et al., 2005]

size in table 5.1 is approximated with the published focal spot size of the driving laser. On the one hand the harmonic source is smaller than the driving laser. On the other hand, efficient HHG is obtained only in front of the focus. Thus, the driving laser and the harmonic source becomes larger. It is therefore not possible to estimate the actual source size of the published data. Nevertheless, table 5.1 shows that the uncertainty of the oxide layer thickness is also transferred to the harmonic power.

This work also revealed a weak point of the transfer-beamline between the HHG source in the pit and its diagnostic section: the triplet mirror-mounts have been constructed to suit the given boundary conditions. Here, the available space in the vacuum chamber is limited and commercially available mirror-mounts do not fit. Therefore, a mount has been constructed which deflects the radiation by 90° in terms of $3 \cdot 30^\circ$. The mounting of each mirror is performed by screws which most likely introduce an additional divergence to the XUV radiation. So far, this effect has been confirmed for a copy of those mounts. A measurement of the actual used mirror mounts is scheduled. As a consequence the absolute measurement of the divergence is not possible. Only relative changes of the divergence can be detected and an upper limit has been deduced. The focus scan of H21 also lacks on this issue and lead to $M^2 < 1$. An exchange of those mirror-mounts is needed to measure absolute values and is scheduled for the next shut-down.

So far, the sFLASH team has commissioned the different sFLASH sections successfully. Seeding itself could not be observed so far for the following reasons.

- In order to initiate lasing of the FEL with an external laser the seed needs to exceed the shot-noise by a factor of roughly three orders of magnitude. Simulations have shown that a coupled seed energy of 100 pJ leads to saturation [Miltchev et al., 2008]. However, the harmonics are transferred to the sFLASH undulators by employing four grazing incidence mirrors and one focusing XUV multilayer mirror. Thus, the seed power is reduced to approximately 20% due to the lack of high-reflectivity XUV mirrors [Bödewadt, 2011].

- In order to overlap the electron bunch with a seed exceeding the shot-noise the 21^{st} harmonic is focused into the undulator section. Unfortunately, the M^2 value of the seed in combination with its beam waist w_0 is not known absolutely. Here, three different focusing mirrors have been installed. For the focus measurements YAG screens and wire-scanners have been installed at several positions before and after the undulators of the sFLASH section. The uncertainty of the corresponding Gaussian beam waist fits are too huge to predict the exact position, beam waist, and the Rayleigh length of the seed within the undulator. Moreover, the measurements indicate that only a fraction of the harmonic power content is coupled to the electron bunch and that the coupled energy is too low in order to initiate the seeding process. More precise considerations regarding the coupling of the XUV radiation to the electron bunches can be found in [Bödewadt, 2011; Tarkeshian, 2011].

5.1 Outlook

In order to overcome those peculiarities the harmonic power content has to be increased and the injection of the seed has to be modified. The following section will summarize different ideas leading to a seeded operation of FLASH.

5.1.1 Seed power

For the enhancement of the seed power two general options are possible.

- On the one hand a higher CE leads to a higher seed power.
- On the other hand the seed energy may be increased by enhancing the laser power and keeping the CE constant (loose focusing). Therefore, the current two-compressor setup has to be changed.

Note that for a seeded operation of FLASH an increase of the seed energy is not sufficient. Only an increase of the harmonic power content within the cross section of the electron bunch will increase the coupled seed energy. Thus, the most promising option is to increase the CE. The second case that the seed energy is increased while the CE is kept constant would only lead to a seeded operation, if the focusing optic within the injection beamline was exchanged to a telescope or an adaptive optic.

Conversion efficiency

An increase of the CE is generally possible with two-color HHG, QPM HHG, and HHG with lower driving laser wavelengths as explained in chapter 4.3.6 and chapter 4.3.7. First experiments have been performed already. It has been shown that both, a two-color HHG and a QPM HHG target can be implemented into to the HHG setup of sFLASH.

- In case of two-color HHG an increase of the 21^{st} harmonic has not been observed, but a thorough optimization of the experimental conditions could not be performed due to the tight sFLASH commissioning schedule. The ratio between the intensities of 800 and 400 nm seems to be critical and needs to be adjusted in vacuum to achieve an absolute increase of the harmonic power content. Therefore, another translation stage has to be implemented into the vacuum which moves the BBO through the Rayleigh length of the 800 nm driving laser. In addition the BBO needs to be rotatable around its optical axis in order to tune the conversion into the SH. Furthermore, an adjustable wave plate to control the polarizations of the fundamental and the SH is needed and a glass plate in order to change the relative phase of the two laser fields as explained in [Kim et al., 2005]. The available space shown in figure 3.9 is limited. The BBO, the wave plate, the glass plate and its opto-mechanics have to fit between the "mirror with hole" and the gas target.
- The second option to increase the CE is QPM HHG. The results in chapter 4.3.6 lack on the fact that the used QPM target was not designed for a pulsed mode. The

dead volume of the gas supply led to an increase of the gas pressure in the harmonic source which exceeded the thresholds given by the electron vacuum of FLASH. However, a new QPM target will be developed to fulfill the vacuum requirements given by the FLASH facility.

- The third option to increase the CE is HHG with smaller driving laser wavelengths [Falcao-Filho et al., 2010]. This option is automatically given as soon as in case of two-color HHG the amount of the SH is controllable.

Loose focusing

As shown in chapter 4.3.2 the H21 energy could not be increased by enlarging the target length. It has been shown that a longer target length leads to a smaller optimal gas pressure. An increase of the target pressure led to a decrease of the absolute harmonic power due to worse phase-matching conditions and absorption. An increase of the harmonic energy can still be established, if the interaction region is increased in terms of a larger focal spot. The focal spot size W_0 depends on the f-number $\mathsf{f}/\#$:

$$\begin{aligned} W_0 &= \tfrac{\lambda}{\pi} \cdot \mathsf{f}/\# \\ &\text{with} \qquad \mathsf{f}/\# = \tfrac{\mathsf{f}}{\mathsf{D}}, \end{aligned}$$

where D is the aperture (iris) in front of the focusing optic [Paschotta, 2008]. Thus, the target can be enlarged by either increasing the focal length or decreasing the aperture size.

A larger focal length is already prepared. The trunks of the harmonic source give the possibility to increase the focal length to $\mathsf{f} = (2.5, 3.5, 5.0, 7.0)$ m. In case of $\mathsf{f} = (5.0, 7.0)$ m an astigmatism is introduced to the driving laser which is not the case for $\mathsf{f} = (2.5, 3.5)$ m. So far the pulse energy was limiting this option. In order to increase the pulse energy with the same laser system the losses need to be reduced. One option would be to remove the UHV pulse compressor and to set up the reflective pulse compressor in vacuum. This option has not been followed so far, because of the lack of space. Meanwhile, there is a new developed reflective grating compressor which fulfills the requirements of the HHG target chamber [Rehders, 2011].

Finally, the developments of the HHG source lack on the tight sFLASH commissioning schedule. During commissioning the different sFLASH sections needed either the harmonic source or the driving laser, thus a redesign, major changes of the source, or a continuous development was not possible. It would be helpful to built up a copy of the HHG source in a separate building on an optical table. Then, changes of the source could be implemented and tested much faster than in the pit and a continuous operation of the harmonic source in the pit could be guaranteed.

5.1.2 Injection beamline

The second route to achieve a seeded operation mode of FLASH is the optimization of the injection beamline. As explained before the measurements of the harmonic beam expansion indicate a bad coupling to the electron bunches. Ideally, the harmonic beam waist should be located at the beginning of the first undulator. In addition, the Rayleigh length should exceed the gain length of the undulators and the beam waist should be in the order of the electron bunches [Miltchev et al., 2008; McNeil et al., 2007a]. So far, three distinct focusing multilayer mirrors are available. In order to move the beamwaist to the entrance of the first undulator and to change the beamwaist independent of each other a XUV telescope or an adaptive XUV focusing mirror is needed.

For a proper simulation of the seeding process the actual properties of the XUV radiation has to be measured in the tunnel. So far, the available XUV energy in the tunnel can only be estimated. It would be important to implement a XUV photodiode in front of the first sFLASH undulator. Also the wavefront measurements performed in the diagnostic section of the HHG source led to falsified results. As soon as the triplet mirrors have been exchanged, the wavefront and the beamwaist expansion can be measured absolutely. Then, GENISIS simulations could be performed again with the actual properties of the XUV radiation, in order to get a thorough understanding of the seeding process at FLASH.

5.1.3 Alternative seeding

In order to exclude any problems which have not been revealed so far a seeding option of for instance 160 nm would be helpful. On the one hand, a 160 nm seed has orders of magnitude more power than a 38 nm seed [Lambert et al., 2008]. Therefore, the contrast ratio between the seeded FEL radiation and the SASE background is much better as shown in [Togashi et al., 2011; Lambert et al., 2008]. In our case it would be necessary to exchange the HHG gas target to xenon and to replace the XUV mirrors in the injection beamline to CaF_2 mirrors [Lambert et al., 2008]. As in case of a 38 nm seed the position of the waist should be at the beginning of the first undulator and the size should be comparable to the electron bunch size. Thus, a single focusing mirror is not adequate. As in case of a 38 nm seed a telescope or an adaptive mirror would be important to have full control over the beam waist and the focus position.

Unfortunately, it is disadvantageous to operate FLASH at 160 nm, because the machine becomes unstable [Miltchev, 2011]. Thus, this operation mode does not suit for the commissioning of sFLASH. The tradeoff to a 160 nm seeded operation will be at 60 nm. Here, the XUV pulse-energy is expected to be larger than in case of 38 nm and the FLASH operation remains stable.

Abbreviations

A

Table A.1: Abbreviations

abbreviation	meaning
ADC	Analog Digital Converter
BBO	Beta Barium bOrate ($\beta{-}BaB_2O_4$)
CAD	Computer Aided Design
CCD	Charge-Coupled Device
CE	Conversion Efficiency
DESY	Deutsches Elektronen SYnchrontron
EUV	Extreme Ultra-Violet
FEL	Free Electron Laser
FLASH	Free electron LASer Hamburg
FROG	Frequency-Resolved Optical Gating
FWHM	Full Width at Half Maximum
HGHG	High-Gain Harmonic Generation
HHG	High Harmonic Generation
Linac	Linear accelerator
LLRF	Low Level Radio Frequency
MCP	Multi-Channel Plate
NIR	Near Infra Red
QE	Quantum Efficiency
ORS	Optical Replica Synthesizer
QPM	Quasi Phase Matching
rms	root mean square
SAE	Single Active Electron
SASE	Self-Amplified Spontaneous Emission
SFA	Strong field approximation
sFLASH	seeded Free Electron LASer Hamburg
TDSE	Time Dependent Schrödinger Equation
Ti:Sa	titanium-sapphire
UHV	Ultra High Vacuum
XUV	eXtreme Ultra Violet

Table A.2: Physical constants

abbreviation	value	meaning
c	299792458 m/s	speed of light
e	$1.602176487 \cdot 10^{-19}$ C	elementary charge
ϵ_0	$8.854187817 \cdot 10^{-12}$ F·m^{-1}	vacuum permittivity
h	$6.62606896 \cdot 10^{-34}$ Js	Planck's constant
k_B	$1.3806504 \cdot 10^{-23}$ J/K	Boltzmann's constant
m_e	9.10938215 kg	electron's rest mass
π	3.14159265	Pi

B

Propagation of uncertainties

The following section summarizes the principle of error propagation (taken from [Taylor, 1939; Bevington and Robinson, 1969]). Usually a physical quantity y_0 cannot be measured directly, but it can be calculated and depends on other measurable quantities x_i:

$$y_0 = y(x_1, x_2, \dots x_n). \tag{B.1}$$

The measured values of the quantities can be expressed as $x_i = x_{i,0} + \Delta x_i$, where Δx_i is the uncertainty of the measurement. To calculate the uncertainty of the calculated quantity

$$y(x_1 + \Delta x_1, x_2 + \Delta x_2, \dots x_n + \Delta x_n) = y_0 + \Delta y$$

the function has to be evolved in terms of a Taylor series:

$$y_0 + \Delta y = y(x_1, x_2, \dots x_n) + \sum_i \frac{1}{1!}\frac{\partial y(x_i)}{\partial x_i}\Delta x_i + \frac{1}{2!}\frac{\partial^2 y(x_i)}{\partial x_i^2}\Delta x_i^2 \dots$$

For sufficient small Δx_i the equation can be simplified to

$$y_0 + \Delta y = y(x_1, x_2, \dots x_n) + \sum_i \frac{\partial y(x_i)}{\partial x_i}\Delta x_i, \tag{B.2}$$

where $\Delta y = \sum_i \frac{\partial y(x_i)}{\partial x_i}\Delta x_i$ is the uncertainty of y_0. If only the absolute value of the uncertainties $|\Delta x_i|$ was known, equation B.2 can be rewritten as

$$y_0 + \Delta y = y(x_1, x_2, \dots x_n) + \sum_i \left|\frac{\partial y(x_i)}{\partial x_i}\right|\Delta x_i. \tag{B.3}$$

In case the variables x_i are independent averaged quantities with an uncertainty u_i, the quantity $y(x_i)$ and its uncertainty u_y can be calculated

$$y + u_y = y(x_1, x_2, \dots) \pm \sqrt{\sum_i \left(\frac{\partial y}{\partial x_i}u_i\right)^2}. \tag{B.4}$$

C Technical details

This section is addressed to the specific technical details of the HHG source and its diagnostics. A brief description of the developed software and the software environment of FLASH is given.

C.1 Software environment

In order to optimize the harmonic source different software utilities have been developed to measure and evaluate the acquired signal. This section summarizes the most important tools of this thesis. For the control of the hardware the "Distributed Object Oriented Controls System" (DOOCS) has been employed. This control system has three layers: the front-end (device server), a middle layer (name server, automation, DAQ, web server etc.), and the client layer. The used hardware of this thesis matches to the already programmed front-end layer. Thus, only the the middle layer had to be adjusted in order to control the devices in terms of the client layer. For the client layer a Java based interface is available. This *java doocs data display* (jddd) is a program to draw control system panels and to run the created drawings with real data as shown in figure C.1. The upper part of the image shows the main window of the client layer. From there it is possible to navigate through the whole FLASH. The window shows buttons linked to the injector, the accelerating modules, the sFLASH section, etc. The sFLASH section itself is illustrated in the middle part of the image. As in the main window different buttons are linked to the different sFLASH sections. The different devices of the source are shown in the lower part of the image. All translation stages, the mirrors, the gas nozzle, the valves, etc. can be controlled by invoking the corresponding button.

Some of the HHG devices have restrictions in their translation. The transverse adjustment of the gas nozzle, for instance, should not exceed a certain value, otherwise the belt for the gear ratio would loose contact and the vacuum system had to be vented. The limitations of the different motors are as follows:

- motor 1: motorized iris (0 mm. . . 40 mm)
- motor 2: z-axis gas valve (0 mm. . . −298 mm)
- motor 3: vertical axis gas valve (±4 mm)
- motor 5: triplet (0mm out of the beam (FLASH); 15 mm B_4C; 23.5 mm MoB_4C)
- motor 8: XUV nearfield (0.00) - farfield switch 0.83 (max. 0.83 arb units)

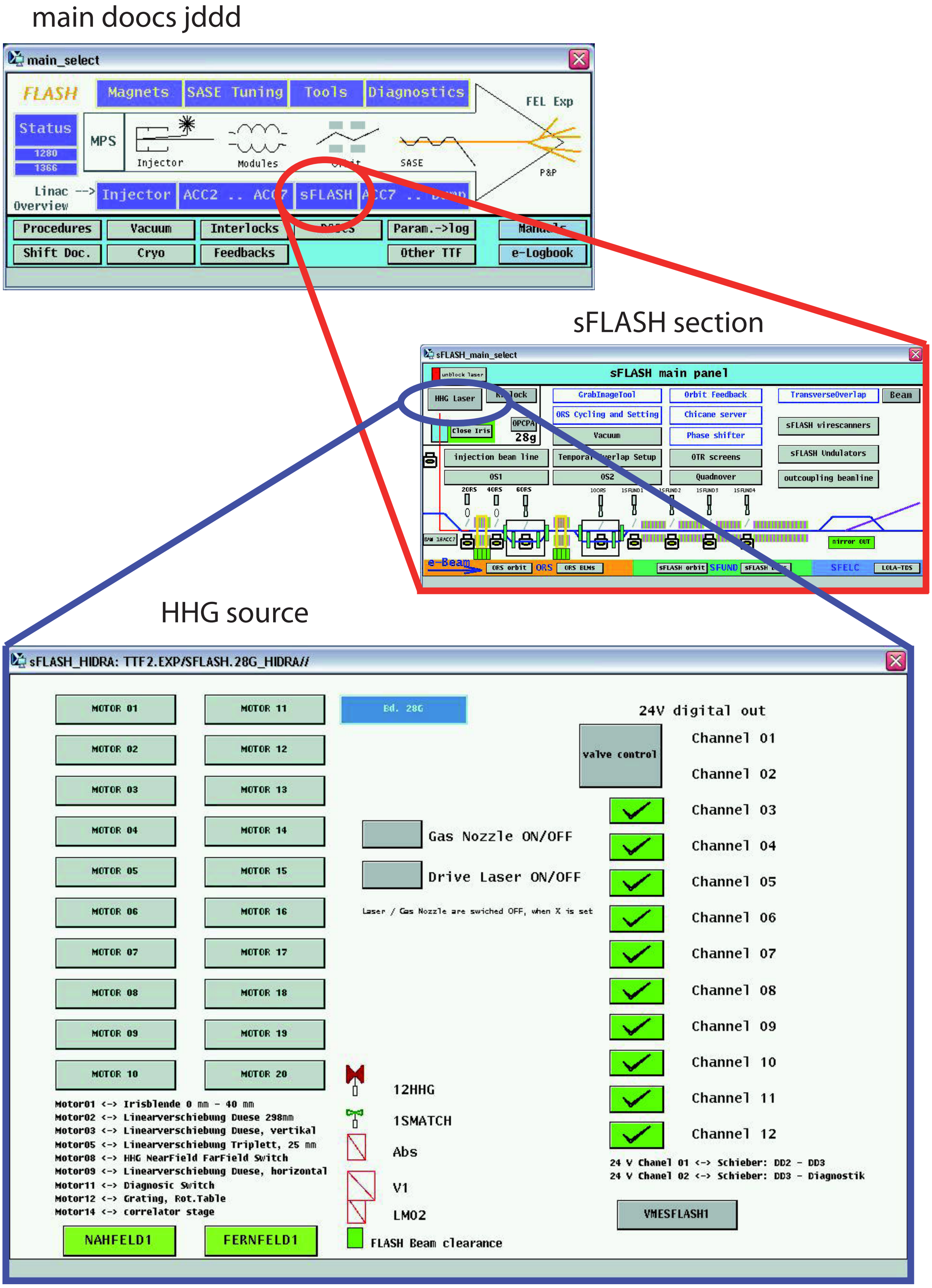

Laser / Gas Nozzle are swiched OFF, when X is set

Motor01 <-> Irisblende 0 mm - 40 mm
Motor02 <-> Linearverschiebung Duese 298mm
Motor03 <-> Linearverschiebung Duese, vertikal
Motor05 <-> Linearverschiebung Triplett, 25 mm
Motor08 <-> HHG NearField FarField Switch
Motor09 <-> Linearverschiebung Duese, horizontal
Motor11 <-> Diagnosic Switch
Motor12 <-> Grating, Rot.Table
Motor14 <-> correlator stage

24 V Chanel 01 <-> Schieber: DD2 - DD3
24 V Chanel 02 <-> Schieber: DD3 - Diagnostik

Figure C.1: Java doocs data display

- motor 9: horizontal axis gas valve (±2 mm)
- motor 11: diagnostic switch (0 mm: MCP; −45 mm XUV-CCD)
- motor 12: diagnostic grating (0: 0^{th}order; −6700: 1^{st} order (arb. units))

The motors are connected to a Beckhoff control unit (Beckhoff Automation GmbH, Verl, Germany) which is further connected to the front-end layer of DOOCS. An exception are the pico motors which are connected to their own Controller (Newport Corporation, CA, USA). This controller is connected to a device server provided by HASYLAB.

However, for the data acquisition and evaluation own software has been developed. The camera data acquisition and online evaluation has been performed with a LabView (National Instruments, Austin, Texas, USA) program. The software is capable to acquire data on a single-shot basis and is able to perform Gauss fits, histograms, second moment calculating, and different filtering. It is further possible to integrate over several light pulses, to select a region of interest, etc. The software is based on a developed software by Drescher et al. and was upgraded to the needs of the harmonic source.

In case of the HHmeter and the photodiode, a LabView script has been developed to readout the 2 GHz scope (Tektronix, Portland, Oregon). The corresponding data is visualized and can be saved in a text file for further evaluation. Post-processing of acquired data has been performed with Matlab (Mathworks, Natick, USA). Here different software has been developed to evaluate the data from the cameras, the HHmeter, or the photodiode as described in chapter 3 and 4.

C.2 Hardware

This section summarizes the hardware used in this thesis. Among the full denotation the most important technical data are given.

Table C.1: Technical data Basler slA1390-17fm, Basler Vision Technologies

property	quantification
resolution	1392x1040
pixel size	(4.65x4.65) μm^2
sensor	CCD

Table C.2: Technical data Beta Barium bOrate, Döhrer Elektrooptik GmbH, Karlsbad

property	quantification
dimension	10x10x0.1 mm^3
typ 1	
angle tolerance	$\Theta = 29.2^\circ \pm 0.5^\circ$
	$\phi = 0^\circ \pm 0.5^\circ$

Table C.3: Technical data CHEVRON, Photonis USA, Inc.

	property	quantification
MCP	diameter	25 mm
	center to center spacing	12 μm
	pore size	10 μm
	bias angle	$12^\circ \pm 1^\circ$
phosphor screen	electron gain at 2000 V	$4 \cdot 10^6$
	dark current	5 $\mathrm{counts/s/cm}^2$

Table C.4: Technical data Grenouille FROG 8-10, Swamp Optics, LLC

property	quantification
pulse length range	$(10 - 100)$ fs
maximal pulse bandwidth	150 nm
spectral resolution	5 nm
spatial chirp accuracy $dx/d\lambda$	1 μm/nm
pulse front tilt accuracy dt/dx	0.05 fs/mm

Table C.5: Technical data Hamamatsu electron multiplier R2362, Hamamatsu Photonics K.K.

property	quantification
input aperture diameter	20 mm
gain	$5 \cdot 10^5$
operating vacuum level	$< 133 \cdot 10^{-4}$ Pa
maximal voltage	4000 V

Table C.6: Technical data PIXIS-XO: 2048B, Princeton Instruments

property	quantification	notes
resolution	2048 x 512 pixel	
pixel size	13.5 µm	
read noise (e^- rms)	16.51	2 MHz readout and Low noise mode (LNM)
	5.21	100 kHz readout, LNM
dark charge (e^-/pixel/sec)	0.0012	(at −70°C) detector temperature
gain 1 (e^-/ADC)	4.00	2 MHz readout, LNM
	4.06	100 kHz readout, LNM
gain 2 (e^-/ADC)	2.80	2 MHz readout, LNM
	2.06	100 kHz readout, LNM
gain 3 (e^-/ADC)	1.10	2 MHz readout, LNM
	1.05	100 kHz readout, LNM
non-linearity	$< 1\%$	
quantum efficiency (e^-/photon)	42%	for 32.5 eV
energy dependent QE (e^-/photon)	4.4	for 32.5 eV

Table C.7: Technical data wavefront sensor ML4010, metrolux optische Messtechnik GmbH

property	quantification
resolution	1392 x 1040
pixel size	(6.45 x 6.45) µm^2
dynamic range	63 dB
frame rate	12 fps
spectral range	(320 – 1100) nm
sensor	CCD

Table C.8: Technical data XUV diffraction grating, Newport Corporation

property	quantification
grooves frequency	1200 per mm
coating	gold
curvature	plane
blaze wavelength	0.1201 µm
blank material	BK7
blaze angle	4.128°
groove length, ruled width	23 mm, 52 mm
blank size	(28.5 x 58 x 10) mm^3

Table C.9: Technical data XUV photodiode, International Radiation Detectors, Inc.

	property	quantification
AXUV-100Al/SiO_2 300/10 nm	quantum efficiency	H01-H09: 0
		H11: 0.06
		H13: 0.6
		H15: 1.0
		H17: 1.1
		H19: 1.8
		H21: 2.0
		H23: 2.3
		H25: 2.7
		H27: 3.0
		H29: 3.5
	chip size	(15.85 x 22.05) mm^2
PA100 amplifier	divisor	1000 (gain: 1)
		5000 (gain: 5)
		10000 (gain: 10)
		100000 (gain: 100)
		⋮

Code of practice D

The following chapter describes the commissioning of the laser system and the HHG source and is meant to be a guideline how to set up the source. It is not a comprehensive manual.

D.1 The laser system

For a proper operation of the harmonic source a thorough adjusted laser system is mandatory. Firstly, the oscillator of the driving laser has to be mode-locked. The oscillator shows a bandwidth between 780 nm - 820 nm if it is not mode-locked and around 750 nm - 850 nm if the modes are locked. In addition the power should exceed 300 mW for a proper operation of the amplifier. In order to maximize the oscillator power, the two resonator mirrors and the z-axis of the Ti:Sa crystal have to be adjusted.

For the chirped pulse amplification a short digital gate (SDG) and a quantum pulse generator is present, where the SDG controls the Pockels cells. In combination with two photodiodes a bandwidth interlock is realized. If for some reason the laser switches to a continuous wave (CW) mode, the diodes realize a change and the Pockels-cells are being switched off, thus no pulses are amplified.

The Nd:YAG laser pumps the regenerative amplifier, as well as the multipass amplifier and the pulses are generated with Pockels cell by means of Q-switching. The pump-pulse produces a population inversion of the Ti:Sa crystal and the Pockels cell 1 couples the seed-pulse into the cavity. Then, the pulse travels 20 times through the regenerative amplifier and get released with an amplification factor of ≈ 100 by Pockels cell 2. Finally, the pulse travels four times through the multipass amplifier and gets amplified by another factor of 7.

In order to set up the pump laser its cooling has to be switched on first (19°C - 23°C). Then, the laser can be switched on. Sometimes, either the Pockels cells have to be reseted or the incoupling of the seed into the amplifier has to be readjusted. For the incoupling two irises are set up in front of the first grating. Note that only an accurate incoupling of the seed leads to amplification. If a proper incoupling is guaranteed the flash lamps of the pump laser can be switched on after the laser shutter has been opened. During the first 15 min of operation the amplified laser pulses are drifting, thus the following steps should be performed after the system is thermally stabilized.

The optimization of the regenerative amplifier and the multipass is much more difficult and needs experience: at the beginning the Pockels cell 1 is enabled, where the second one is disabled. Then, the Amplified Spontaneous Emission (ASE) can be visualized with a scope and optimized. The Potassium Titanium Oxide Phosphate ($KTiOPO_4$) crystal of the pump laser and the incoupling mirror labeled as P1 is used to maximize the pump laser power. Afterwards, Pockels cell 2 is enabled and the seed is adjusted by optimizing the mirrors S1 and S2. It is now important that not the strongest, but the most stable pulse of the build-up-pattern is released and subsequently amplified in the multipass amplifier. The optimization procedure has to be repeated until the pulse-energy stability is better than 5% rms and the laser power is > 40 mJ. Due to the nonlinear nature of the HHG process the driving laser should be as stable as possible and the pulse energy of 40 mJ is required for the saturation of HHG. Otherwise the following optimization procedure of the HHG source cannot be performed sufficiently good.

D.2 High harmonic generation source

For the setup of the HHG source the amplified laser radiation has to be aligned into the vacuum. First the laser passes the reflective grating compressor to pre-compress the laser pulses. A near and farfield monitor of the driving laser guarantees the correct alignment. Then, the laser needs to be aligned into the pit. The most critical mirrors which usually have to be readjusted are the last mirror above the pit and the first mirror in the pit. Here two further irises are set up in the pit to ensure an adequate incoupling and the subsequent final compression of the laser pulse in the vacuum.

Once the laser is optimized and aligned the HHG devices can be set up. Slowly switch on the MCP (1.5 kV), the fluorescence screen (4.5 kV), the HHmeter (3.5 kV, max 4.2 kV), the amplifier (15 V), and the CCD (−30°C detector temperature). Note that a fast increase of the voltage may damage the MCP. Then DOOCS can be employed to move or adjust any device within the vacuum system. Open the valves of the HHG source and ensure the proper position of the first triplet mirror system. Also the first mirror in the diagnostic section (diagnostic switch) should be moved to the position that the spectrometer can be operated to optimize H21.

The last mirror in front of the trunks and the mirror within the trunk has to be used to align the laser through the differential pumping stages. Afterwards, the gas target is aligned to the laser path. Note that the gas load should not exceed the FLASH vacuum conditions.

Now the gas may be switched on and the harmonic signal should appear on the scope of the HHmeter. If not either the backing pressure of the gas target is not set correctly or the timing between the laser pulse and the gas nozzle is out of range. However, for the final optimization of the HHG source, the x,y,z-position of the gas target relative to the laser focus, the diameter of the iris, the backing pressure of the target, and the timing has to be adjusted according to chapter 4.

For the HHG control different hardware and software utilities are available as described in chapter C. For the XUV CCD it is necessary to unplug the pressure sensor of the diagnostic section and to move the aluminum filter into the beam, otherwise the XUV CCD is overexposed or may even be damaged due to the fundamental laser.

Once the harmonic source is optimized the XUV radiation can be send into the tunnel.

Therefore, only the triplet mirror has to be moved out of the laser path. The first diagnostic device in the injection beamline is a YAG screen. It is further necessary to adjust the XUV radiation to a reference point by employing the mirror in the trunk. In case the laser cannot be aligned without hitting a differential pumping iris, also the last mirror in the pit and the target has to be readjusted. Unfortunately, in this situation the optimization procedure of the HHG source has to be repeated.

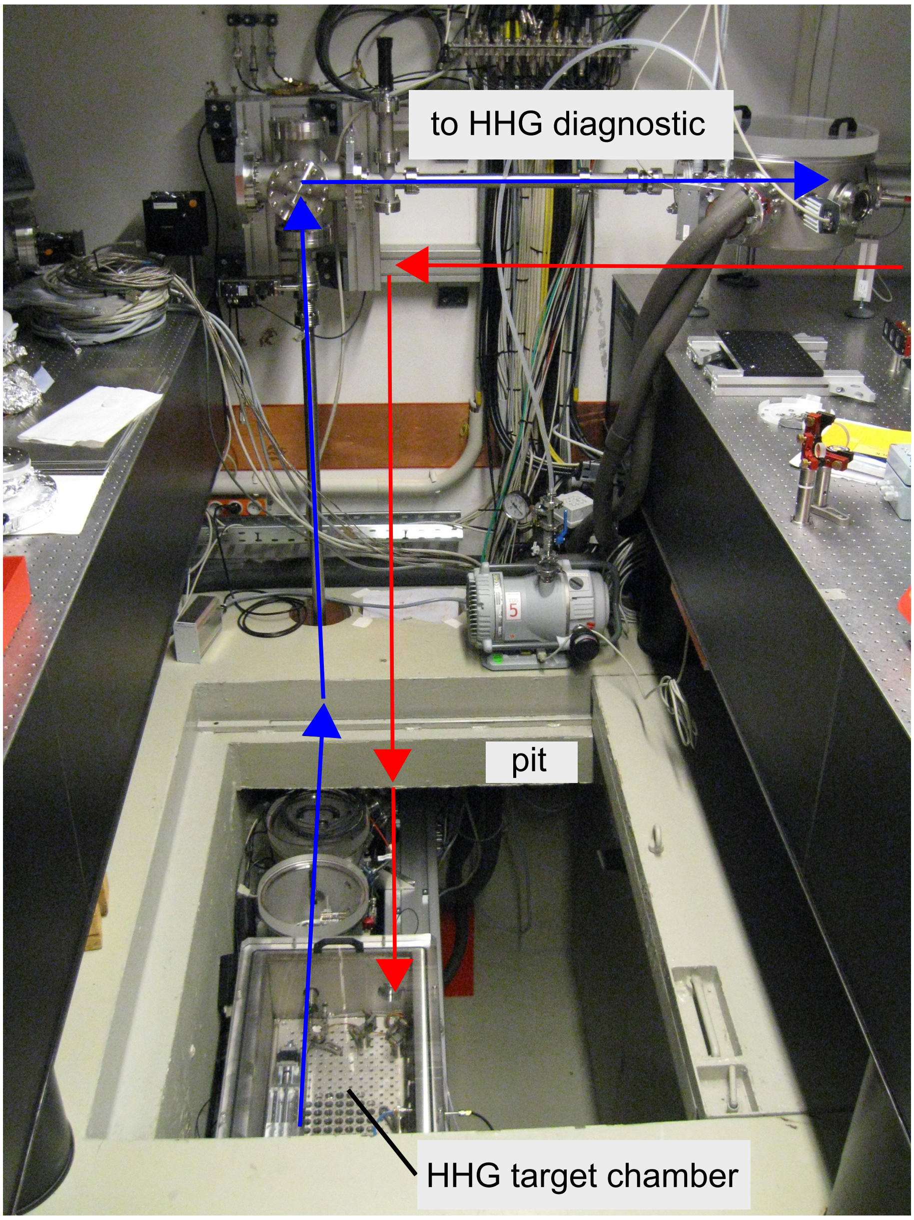

Figure D.1: Picture of the HHG source in the pit.

Bibliography

Ackermann, W., Asova, G., Ayvazyan, V., Azima, A., Baboi, N., Bähr, J., Balandin, V., Beutner, B., Brandt, A., Bolzmann, A., Brinkmann, R., Brovko, O., Castellano, M., Castro, P., Catani, L., Chiadroni, E., Choroba, S., Cianchi, A., Costello, J., Cubaynes, D., Dardis, J., Decking, W., Delsim-Hashemi, H., Delserieys, A., Di Pirro, G., Dohlus, M., Düsterer, S., Eckhardt, A., Edwards, H., Faatz, B., Feldhaus, J., Flöttmann, K., Frisch, J., Fröhlich, L., Garvey, T., Gensch, U., Gerth, C., Görler, M., Golubeva, N., Grabosch, H.-J., Grecki, M., Grimm, O., Hacker, K., Hahn, U., Han, J. H., Honkavaara, K., Hott, T., Hüning, M., Ivanisenko, Y., Jaeschke, E., Jalmuzna, W., Jezynski, T., Kammering, R., Katalev, V., Kavanagh, K., Kennedy, E., Khodyachykh, S., Klose, K., Kocharyan, V., Körfer, M., Kollewe, M., Koprek, W., Korepanov, S., Kostin, D., Krassilnikov, M., Kube, G., Kuhlmann, M., Lewis, C., Lilje, L., Limberg, T., Lipka, D., Löhl, F., Luna, H., Luong, M., Martins, M., Meyer, M., Michelato, P., Miltchev, V., Möller, W., Monaco, L., Müller, W., Napieralski, O., Napoly, O., Nicolosi, P., Nölle, D., Nunez, T., Oppelt, A., Pagani, C., Paparella, R., Pchalek, N., Pedregosa-Gutierrez, J., Petersen, B., Petrosyan, B., Petrosyan, G., Petrosyan, L., Pflüger, J., Plönjes, E., Poletto, L., Pozniak, K., Prat, E., Proch, D., Pucyk, P., Radcliffe, P., Redlin, H., Rehlich, K., Richter, M., Roehrs, M., Roensch, J., Romaniuk, R., Ross, M., Rossbach, J., Rybnikov, V., Sachwitz, M., Saldin, E., Sandner, W., Schlarb, H., Schmidt, B., Schmitz, M., Schmüser, P., Schneider, J., Schneidmiller, E., Schnepp, S., Schreiber, S., Seidel, M., Sertore, D., Shabunov, A., Simon, C., Simrock, S., Sombrowski, E., Sorokin, A., Spanknebel, P., Spesyvtsev, R., Staykov, L., Steffen, B., Stephan, F., Stulle, F., Thom, H., Tiedtke, K., Tischer, M., Toleikis, S., Treusch, R., Trines, D., Tsakov, I., Vogel, E., Weiland, T., Weise, H., Wellhöfer, M., Wendt, M., Will, I., Winter, A., Wittenburg, K., Wurth, W., Yeates, P., Yurkov, M., Zagorodnov, I., and Zapfe, K. (2007). Operation of a free-electron laser from the extreme ultraviolet to the water window. *Nature Photon. 1*, pages 336–342.

Agostini, P. (2004). The physics of attosecond light pulses. *Rep.Prog.Phys*, 67:813–855.

Allaria, Bocchetta, Bulfone, Cargnello, Cocco, Cornacchia, Craievich, Auria, Danailov, Ninno, Mitri, Diviacco, Ferianis, Galimberti, Gambitta, G., Iazzourene, Karantzoulis, Lonza, Mazzolini, Parmigiani, Penco, Rumiz, Spampinati, Stefanutti, Tromba, Trovo, Vascotto, Veronese, Zangrando, Corlett, Doolittle, Fawley, Lidia, Penn, Pogorelov, Qiang, Ratti, Staples, Wilcox, Zholents, Emma, Huang, Wu, Graves, Kaertner, and Wang (2010). FERMI at elettra: a seeded FEL facility for EUV and soft x-rays. In *Proceedings of FEL2010, Malmö.*

Allison, T. K. (2010). *Femtosecond molecular dynamics studied with vacuum ultraviolet pulse pairs.* PhD thesis, University of California at Berkeley.

Altarelli, M., Brinkmann, R., Chergui, M., Decking, W., Dobson, B., Düsterer, S., Grübel, G., Graeff, W., Graafsma, H., Hajdu, J., Marangos, J., Pflüger, J., Redlin, H., Riley, D., Robinson, I., Rossbach, J., Schwarz, A., Tiedtke, K., Tschentscher, T., Vartaniants, I., Wabnitz, H., Weise, H., Wichmann, R., Witte, K., Wolf, A., Wulff, M., and Yurkov, M. (2006). XFEL the european x-ray free-electron laser. In *Technical Design Report, DESY 2006-097*.

Ammosov, M., Delone, N., and Krainov, V. (1986). Tunnel ionization of complex atoms and of atomic ions in an alternating electromagnetic field. *Sov. Phys. JETP*, 64:1191–.

Andruszkow, J., Aune, B., Ayvazyan, V., Baboi, N., Bakker, R., Balakin, V., Barni, D., Bazhan, A., Bernard, M., Bosotti, A., Bourdon, J. C., Brefeld, W., Brinkmann, R., Buhler, S., Carneiro, J.-P., Castellano, M., Castro, P., Catani, L., Chel, S., Cho, Y., Choroba, S., Colby, E. R., Decking, W., Den Hartog, P., Desmons, M., Dohlus, M., Edwards, D., Edwards, H. T., Faatz, B., Feldhaus, J., Ferrario, M., Fitch, M. J., Flöttmann, K., Fouaidy, M., Gamp, A., Garvey, T., Gerth, C., Geitz, M., Gluskin, E., Gretchko, V., Hahn, U., Hartung, W. H., Hubert, D., Hüning, M., Ischebek, R., Jablonka, M., Joly, J. M., Juillard, M., Junquera, T., Jurkiewicz, P., Kabel, A., Kahl, J., Kaiser, H., Kamps, T., Katelev, V. V., Kirchgessner, J. L., Körfer, M., Kravchuk, L., Kreps, G., Krzywinski, J., Lokajczyk, T., Lange, R., Leblond, B., Leenen, M., Lesrel, J., Liepe, M., Liero, A., Limberg, T., Lorenz, R., Hua, L. H., Hai, L. F., Magne, C., Maslov, M., Materlik, G., Matheisen, A., Menzel, J., Michelato, P., Möller, W.-D., Mosnier, A., Müller, U.-C., Napoly, O., Novokhatski, A., Omeich, M., Padamsee, H. S., Pagani, C., Peters, F., Petersen, B., Pierini, P., Pflüger, J., Piot, P., Phung Ngoc, B., Plucinski, L., Proch, D., Rehlich, K., Reiche, S., Reschke, D., Reyzl, I., Rosenzweig, J., Rossbach, J., Roth, S., Saldin, E. L., Sandner, W., Sanok, Z., Schlarb, H., Schmidt, G., Schmüser, P., Schneider, J. R., Schneidmiller, E. A., Schreiber, H.-J., Schreiber, S., Schütt, P., Sekutowicz, J., Serafini, L., Sertore, D., Setzer, S., Simrock, S., Sonntag, B., Sparr, B., Stephan, F., Sytchev, V. A., Tazzari, S., Tazzioli, F., Tigner, M., Timm, M., Tonutti, M., Trakhtenberg, E., Treusch, R., Trines, D., Verzilov, V., Vielitz, T., Vogel, V., Walter, G. v., Wanzenberg, R., Weiland, T., Weise, H., Weisend, J., Wendt, M., Werner, M., White, M. M., Will, I., Wolff, S., Yurkov, M. V., Zapfe, K., Zhogolev, P., and Zhou, F. (2000). First observation of self-amplified spontaneous emission in a free-electron laser at 109 nm wavelength. *Phys. Rev. Lett.*, 85(18):3825–3829.

Antoine, P., L'Huillier, A., and Lewenstein, M. (1996). Attosecond pulse trains using high-order harmonics. *Phys. Rev. Lett.*, 77(7):1234–1237.

Armstrong, J. A., Bloembergen, N., Ducuing, J., and Pershan, P. S. (1962). Interactions between light waves in a nonlinear dielectric. *Phys. Rev.*, 127(6):1918–1939.

Attwood, D. (2000). *Soft X-rays and extreme ultraviolet radiation.* Cambridge University Press.

Ayvazyan, V., Baboi, N., Bohnet, I., Brinkmann, R., Castellano, M., Castro, P., Catani, L., Choroba, S., Cianchi, A., Dohlus, M., Edwards, H. T., Faatz, B., Fateev, A. A., Feldhaus, J., Flöttmann, K., Gamp, A., Garvey, T., Genz, H., Gerth, C., Gretchko, V., Grigoryan, B., Hahn, U., Hessler, C., Honkavaara, K., Hüning, M., Ischebeck, R., Jablonka, M., Kamps, T., Körfer, M., Krassilnikov, M., Krzywinski, J., Liepe, M., Liero, A., Limberg, T., Loos, H., Luong, M., Magne, C., Menzel, J., Michelato, P., Minty, M., Müller, U.-C., Nölle, D., Novokhatski, A., Pagani, C., Peters, F., Pflüger, J., Piot, P., Plucinski, L., Rehlich, K., Reyzl, I., Richter, A., Rossbach, J., Saldin, E. L., Sandner, W., Schlarb, H., Schmidt, G., Schmüser, P., Schneider, J. R., Schneidmiller, E. A., Schreiber, H.-J., Schreiber, S., Sertore, D., Setzer, S., Simrock, S., Sobierajski, R., Sonntag, B., Steeg, B., Stephan, F., Sytchev, K. P., Tiedtke, K., Tonutti, M., Treusch, R., Trines, D., Türke, D., Verzilov, V., Wanzenberg, R., Weiland, T., Weise, H., Wendt, M., Will, I., Wolff, S., Wittenburg, K., Yurkov, M. V., and Zapfe, K. (2002). Generation of gw radiation pulses from a vuv free-electron laser operating in the femtosecond regime. *Phys. Rev. Lett.*, 88(10):104802.

Azima, A., Düsterer, S., Redlin, H., Radcliffe, P., Schlarb, H., Feldhaus, J., and Meyer, M. (2007). Jitter reduced pump-probe experiments. In *Proceedings DIPAC'07, Venice,* 337.

Baboi, N., Castro, P., Hensler, O., Lund-Nielsen, J., Nolle, D., Petrosyan, L., Prat, E., Traber, T., Krasilnikov, M., and Riesch, W. (2007). Beam position monitor calibration at the FLASH linac at DESY. In *Proceedings of PAC'07, Albuquerque, 3937.*

Balcou, P., Dederichs, A. S., Gaarde, M. B., and L'Huillier, A. (1999). Quantum-path analysis and phase matching of high-order harmonic generation and high-order frequency mixing processes in strong laser fields. *Journal of Physics B: Atomic, Molecular and Optical Physics*, 32:2973–2989.

Bartels, R., Paul, A., Green, H., Kapteyn, H., Murane, M., Backus, S., Christov, I., Liu, Y., Attwood, D., and Jacobsen, C. (2002). Generation of spatially coherent light at extreme ultraviolet wavelengths. *Science*, 279:376–378.

Barty, A., Boutet, S., Bogan, M. J., Hau-Riege, S., Marchesini, S., Sokolowski-Tinten, K., Stojanovic, N., Tobey, R., Ehrke, H., Cavalleri, A., Dusterer, S., Frank, M., Bajt, S., Woods, B. W., Seibert, M. M., Hajdu, J., Treusch, R., and Chapman, H. N. (2008). Ultrafast single-shot diffraction imaging of nanoscale dynamics. *Nat. Photon*, 2:415–419.

Becker, U. and Shirley, D. A. (1996). *VUV and soft x-ray photoionization.* Plenum Press, New York.

Bellini, M., Corsi, C., and Gambino, M. C. (2001). Neutral depletion and beam defocusing in harmonic generation from strongly ionized media. *Phys. Rev. A*, 64(2):023411.

Benattar, R., Popovics, C., and Sigel, R. (1979). Polarized light interferometer for laser fusion studies. *Rev. Scient. Instrum.*, 50:5083.

Best, R. E. (2003). *Phase-locked Loops: Design, Simulation and Applications.* McGraw-Hill.

Bevington, P. R. and Robinson, D. K. (1969). *Data reduction and error analysis for the physical sciences.* McGraw-Hill.

Bittner, L., Feldhaus, J., Hahn, U., Hesse, M., Jastrow, U., Kotscharjan, V., Radcliffe, P., Saldin, E., Schneidmiller, E., Tiedtke, K., Timmann, B., Treusch, R., von Bargen, N., M.W., Y., Brovko, O., Kharlamov, D., Lokhmatov, V., Matyushevskiy, E., Shabunov, A., and Syresin, E. (2007). MCP-based photon detector with extended wavelength range for FLASH. In *Proceedings FEL'07 , Novosibirsk.*

Bödewadt, J. (2011). *to be published.* PhD thesis, University of Hamburg.

Bödewadt, J., Azima, A., Curbis, F., Delsim-Hashemi, H., Drescher, M., Hass, E., Hipp, U., Maltezopoulos, T., Miltchev, V., Mittenzwey, M., Rehders, M., Rossbach, J., Rönsch-Schulenburg, J., Tarkeshian, R., Wieland, M., Bajt, S., Düsterer, S., Honkavaara, K., Laarmann, T., Schlarb, H., Khan, S., and Ischebeck, R. (2010). sFLASH - first results of direct seeding at FLASH. In *Proceedings FEL 2010, Malmö.*

Bogan, M. J., Benner, W. H., Boutet, S., Rohner, U., Frank, M., Barty, A., Seibert, M. M., Maia, F., Marchesini, S., Bajt, S., Woods, B., Riot, V., Hau-Riege, S. P., Svenda, M., Marklund, E., Spiller, E., Hajdu, J., and Chapman, H. N. (2008). Single particle x-ray diffractive imaging. *Nano Letters*, 8(1):310–316. PMID: 18095739.

Born, M. and Wolf, E. (1980). *Principles of Optics.* Cambridge University Press Ltd, Oxford.

Boutet, S., Bogan, M., Barty, A., Frank, M., Benner, W., Marchesini, S., Seibert, M., Hajdu, J., and Chapman, H. (2008). Ultrafast soft x-ray scattering and reference-enhanced diffractive imaging of weakly-scattering nanoparticles. *J. Electron Spectrosc. Relat. Phenom.*, 166-167:65–73.

Boutet, S. and Williams, G. J. (2010). The coherent x-ray imaging (cxi) instrument at the linac coherent light source (lcls). *New Journal of Physics*, 12(3):035024.

Brabec, T. (2008). *Strong Field Laser Physics.* Springer Science and Business Media.

Brabec, T. and Krausz, F. (2000). Intense few-cycle laser fields: Frontiers of nonlinear optics. *Rev. Mod. Phys.*, 72(2):545–591.

Brabec, T., Spielmann, C., Curley, P. F., and Krausz, F. (1992). Kerr lens mode locking. *Opt. Lett.*, 17(18):1292.

Brunetti, E., Issac, R., and Jaroszynski, D. A. (2008). Quantum path contribution to high-order harmonic spectra. *Phys. Rev. A*, 77(2):023422.

Budil, K. S., Salières, P., Perry, M. D., and L'Huillier, A. (1993). Influence of ellipticity on harmonic generation. *Phys. Rev. A*, 48(5):R3437–R3440.

Campbell, T., Kalia, R. K., Nakano, A., Vashishta, P., Ogata, S., and Rodgers, S. (1999). Dynamics of oxidation of aluminum nanoclusters using variable charge molecular-dynamics simulations on parallel computers. *Phys. Rev. Lett.*, 82(24):4866–4869.

Chang, Z. and Corkum, P. (2010). Attosecond photon sources: the first decade and beyond. *J. Opt. Soc. Am. B*, 27(11):B9–B17.

Chapman, H. N., Barty, A., Bogan, M. J., Boutet, S., Frank, M., Hau-Riege, S. P., Marchesini, S., Woods, B. W., Bajt, S., Benner, W. H., London, R. A., Plonjes, E., Kuhlmann, M., Treusch, R., Dusterer, S., Tschentscher, T., Schneider, J. R., Spiller, E., Moller, T., Bostedt, C., Hoener, M., Shapiro, D. A., Hodgson, K. O., van der Spoel, D., Burmeister, F., Bergh, M., Caleman, C., Huldt, G., Seibert, M. M., Maia, F. R. N. C., Lee, R. W., Szoke, A., Timneanu, N., and Hajdu, J. (2006). Femtosecond diffractive imaging with a soft x-ray free-electron laser. *Nat. Phys.*, 2:839–843.

Chapman, H. N., Hau-Riege, S. P., Bogan, M. J., Bajt, S., Barty, A., Boutet, S., Marchesini, S., Frank, M., Woods, B. W., Benner, W. H., London, R. A., Rohner, U., Szoke, A., Spiller, E., Moller, T., Bostedt, C., Shapiro, D. A., Kuhlmann, M., Treusch, R., Plonjes, E., Burmeister, F., Bergh, M., Caleman, C., Huldt, G., Seibert, M. M., and Hajdu, J. (2007). Femtosecond time-delay x-ray holography. *Nature*, 448:676–680.

Chen, S. and Wang, J. (1991). Self-starting issues of passive self-focusing mode locking. *Opt. Lett.*, 16(21):1689.

Collett, E. (1992). *Polarized Light.* Marcel Dekker Inc.

Corkum, P. and Krausz, F. (2007). Attosecond science. *Nature*, 3:381–387.

Corkum, P. B. (1993). Plasma perspective on strong field multiphoton ionization. *Phys. Rev. Lett.*, 71(13):1994– –1997.

Curbis, F., Azima, A., Bödewadt, J., Delsim-Hashemi, H., Drescher, M., Hass, E., Hipp, U., Maltezopoulos, T., Miltchev, V., Mittenzwey, M., Rehders, M., Rossbach, J., Rönsch-Schulenburg, J., Tarkeshian, R., Wieland, M., Bajt, S., Düsterer, S., Honkavaara, K., Laarmann, T., Schlarb, H., Khan, S., and Ischebeck, R. (2010). Characterization of seeded FEL pulses at FLASH: status, challenges and opportunities. In *Proceedings FEL 2010, Malmö.*

Curbis, F., Azima, A., Bödewadt, J., Delsim-Hashemi, H., Drescher, M., Hass, E., Hipp, U., Maltezopoulos, T., Miltchev, V., Mittenzwey, M., Rehders, M., Rossbach, J., Rönsch-Schulenburg, J., Tarkeshian, R., Wieland, M., Bajt, S., Düsterer, S., Honkavaara, K., Laarmann, T., Schlarb, H., Khan, S., and Ischebeck, R. (2009). Photon diagnostics for the seeding experiment at FLASH. In *Proceedings FEL'09 , Liverpool.*

CXRO (2009). *x-ray data booklet.* Lawrence Berkeley National Laboratory.

Deacon, D., Elias, L., Madey, J., Ramian, G., and Schwettman, H.A.and Smith, T. (1977). First operation of a free-electron laser. *Phys. Rev. Lett.*, 38(16):892–894.

Delsim-Hashemi, H., Miltchev, V., Rossbach, J., Tischer, M., Schöps, A., Holler, Y., and Vasserman, I. (2009). Status of the sFLASH undulator system. In *Proceedings FEL'09, Liverpool.*

DESY (2010). DESY Jahresbericht.

DESY (2011). `http://www.desy.de/`.

Dietrich, P., Burnett, N. H., Ivanov, M., and Corkum, P. B. (1994). High-harmonic generation and correlated two-electron multiphoton ionization with elliptically polarized light. *Phys. Rev. A*, 50(5):R3585–R3588.

DiMauro, L., Doyuran, A., Graves, W., Heese, R., Johnson, E. D., Krinsky, S., Loos, H., Murphy, J. B., Rakowsky, G., Rose, J., Shaftan, T., Sheehy, B., Skaritka, J., Wang, X. J., and Yu, L. H. (2003). First SASE and seeded FEL lasing of the NSLS DUV FEL at 266 and 400 nm. *Nuclear Instruments and Methods in Physics Research Section A: Accelerators, Spectrometers, Detectors and Associated Equipment*, 507(1-2):15 – 18.

Ditmire, T., Gumbrell, E. T., Smith, R. A., Tisch, J. W. G., Meyerhofer, D. D., and Hutchinson, M. H. R. (1996). Spatial coherence measurement of soft x-ray radiation produced by high order harmonic generation. *Phys. Rev. Lett.*, 77(23):4756–4759.

Ditmire, T. and Smith, R. (1998). Short-pulse laser interferometric measurement of absolute gas densities from a cooled gas jet. *Opt. Letters*, 23:618–620.

Doyuran, A., DiMauro, L., Graves, W., Heese, R., Johnson, E. D., Krinsky, S., Loos, H., Murphy, J. B., Rakowsky, G., Rose, J., Shaftan, T., Sheehy, B., Shen, Y., Skaritka, J., Wang, X., Wu, Z., and Yu, L. H. (2004). Experimental study of a high-gain harmonic-generation free-electron laser in the ultraviolet. *Phys. Rev. ST Accel. Beams*, 7(5):050701.

Drescher, M., Frühling, U., Krikunova, M., Maltezopoulos, T., and Wieland, M. (2010). Time-diagnostics for improved dynamics experiments at xuv fels. *J.Phys.B: At.Mol.Opt.Phys.*, 43:194010–.

Drescher, M., Hentschel, M., Kienberger, R., Tempea, G., Spielmann, C., Reider, G., Corkum, P., and Krausz, F. (2001). X-ray pulses approaching the attosecond frontier. *Nature*, 291.

Drescher, M., Hentschel, M., Kienberger, R., Uiberacker, M., Yakoviev, V., Scrinzi, A., Westerwalbesloh, T., Kleineberg, U., Heinzmann, U., and Krausz, F. (2002). Time-resolved atomic inner-shell spectroscopy. *Nature*, 419.

Duke, P. J. (2000). *Synchrotron Radiation: Production and Properties.* Oxford University Press.

Durfee, C. G., Rundquist, A. R., Backus, S., Herne, C., Murnane, M. M., and Kapteyn, H. C. (1999). Phase matching of high-order harmonics in hollow waveguides. *Phys. Rev. Lett.*, 83:2187–2190.

Elias, L. R., Fairbank, W. M., Madey, J. M. J., Schwettman, H. A., and Smith, T. I. (1976). Observation of stimulated emission of radiation by relativistic electrons in a spatially periodic transverse magnetic field. *Phys. Rev. Lett.*, 36(13):717–720.

Emma, P. (2009). First lasing of the LCLS X-ray FEL at 1.5 a. In *Proc. 23rd Particle Accelerator Conference PAC 09, Vancouver.*

Erny, C., Mansten, E., Gisselbrecht, M., Schwenke, J., Rakowski, R., He, X., Gaarde, M. B., Werin, S., and L'Huillier, A. (2011). Metrology of high-order harmonics for free-electron laser seeding. *New Journal of Physics*, 13(7):073035.

Falcao-Filho, E., Gkortsas, V., Gordon, A., and Kärtner, F. X. (2009). Analytic scaling analysis of high harmonic generation conversion efficiency. *Optics Express*, 17:11217–11229.

Falcao-Filho, E., Lai, C.-J., Hong, K.-H., Gkortsas, V.-M., Huang, S.-W., Chen, L.-J., and Kärtner, F. X. (2010). Scaling of high-order harmonic efficiencies with visible wavelength drivers: A route to efficient extreme ultraviolet sources. *Applied Physics Letters*, 97:061107.

Fawley, W. (2004). A user manual for GINGER. LBNL-49625-Rev.1 `http://www-ssrl.slac.stanford.edu/lcls/lcls_tech_notes.html/LCLS-TN-04-3.pdf`.

Fejer, M., Magel, G., Jundt, D., and Byer, R. (1992). Quasi-phase-matched second harmonic generation: tuning and tolerances. *IEEE Journal of Quantum Electronics*, 28(11):2631 –2654.

Feynman, R. (1963). *The Feynman lectures on physics.* Addison-Wesley publishing company.

Flettner, A., Günther, J., Mason, M. B., Weichmann, U., Düren, R., and Gerber, G. (2001). High harmonic generation at 1 khz repetition rate with a pulsed valve. *Applied Physics B: Lasers and Optics*, 73:129–132.

Frank L. Pedrotti, S.J., L. S. P. (1987). *Introduction to optics.* Prentice-Hall International (UK) Limited, UK, London.

Franken, P. A., Hill, A. E., Peters, C. W., and Weinreich, G. (1961). Generation of optical harmonics. *Phys. Rev. Lett.*, 7(4):118–119.

Fraser, J., Sheffield, R., and Gray, E. (1986). A new high-brightness electron injector for free electron lasers driven by rf linacs. *Nuclear Instruments and Methods in Physics Research Section A: Accelerators, Spectrometers, Detectors and Associated Equipment*, 250(1-2):71 – 76.

Frühling, U., Wieland, M., Gensch, M., Gebert, T., Schütte, B., Krikunova, M., Kalms, R., Budzyn, F., Grimm, O., Rossbach, J., Plonjes, E., and Drescher, M. (2009). Single-shot terahertz-filed-driven x-ray streak camera. *Nat. Photon*, 3:523–528.

Frumker, E., Paulus, G. G., Villeneuve, D. M., and Corkum, P. B. (2011). Order-dependent wavefront structure of high harmonic radiation. In *Quantum Electronics and Laser Science Conference*, page QMC7. Optical Society of America.

Gaarde, M. B., Salin, F., Constant, E., Balcou, P., Schafer, K. J., Kulander, K. C., and L'Huillier, A. (1999). Spatiotemporal separation of high harmonic radiation into two quantum path components. *Phys. Rev. A*, 59(2):1367–1373.

Galayda, J. N., Arthur, J., Ratner, D., and White, E. (2010). X-ray free-electron lasers - present and future capabilities. *J. Opt. Soc. Am. B*, 27:B106–B118.

Gallagher, T. F. (1988). Above-threshold ionization in low-frequency limit. *Phys. Rev. Lett.*, 61(20):2304–2307.

Garvey, T. (2010). Status of the PSI x-ray free-electron laser SWISSFEL. In *Proceedings of FEL2010, Malmö.*

Garzella, D., Hara, T., Carre, B., Salieres, P., Shintake, T., Kitamura, H., and Couprie, M. E. (2004). Using vuv high-order harmonics generated in gas as a seed for single pass FEL]. *Nuclear Instruments and Methods in Physics Research Section A: Accelerators, Spectrometers, Detectors and Associated Equipment*, 528:502–505.

Gavrila, M. (1992). *Atoms in intense laser fields.* Academic Press, Inc.

Giannessi, L., Alesini, D., Biagini, M., Boscolo, M., Bougeard, M., Breger, P., CarrÃľ, B., Castellano, M., Cianchi, A., Ciocci, F., Chiadroni, E., Clozza, A., Couprie, M., Cultrera, L., Dattoli, G., Silvestri, S. D., Pace, A. D., Pirro, G. D., Doria, A., Drago, A., Ferrario, M., Filippetto, D., Frassetto, F., Fusco, V., Gallerano, G., Gallo, A., Garzella, D., Ghigo, A., Germano, M., Giovenale, E., Labat, M., Lambert, G., Mattioli, M., Merdji, H., Monchicourt, P., Migliorati, M., Musumeci, P., Nisoli, M., Orlandi, G., Ottaviani, P., Pace, E., Pagnutti, S., Palumbo, L., Petralia, A., Petrarca, M., Poletto, L., Quattromini, M., Reiche, S., Rosenzweig, J., Ronsivalle, C., SaliÃÍres, P., Sabia, E., Sansone, G., Serafini, L., Spassovsky, I., Spataro, B., Stagira, S., Surrenti, V., Tchebakoff, O., Tomassini, S., Tondello, G., Vaccarezza, C., and Vicario, C. (2008).

Seeding experiments at sparc. *Nuclear Instruments and Methods in Physics Research Section A: Accelerators, Spectrometers, Detectors and Associated Equipment*, 593(1-2):132 – 136.

G.Lambert, F.Tissandier, Gautier, J., Hauri, C., Zeitoun, P., C.Valentin, Marchenko, T., Goddet, J., Ribiere, M., Sardinha, A., Fajardo, M., Hamouda, F., Maynard, G., Rey, G., and Sebban, S. (2010). Aberration-free high-harmonic source generated with a two-colour field. *Europhys. Lett.*, 89:24001.

Gouy, L. G. (1890). Sur une propriete nouvelle des ondes lumineuses. *C. R. Acad. Sci. Paris*, 110:1251.

Gutt, C., Streit-Nierobisch, S., Stadler, L.-M., Pfau, B., Günther, C. M., Könnecke, R., Frömter, R., Kobs, A., Stickler, D., Oepen, H. P., Fäustlin, R. R., Treusch, R., Feldhaus, J., Weckert, E., Vartanyants, I. A., Grunze, M., Rosenhahn, A., Wilhein, T., Eisebitt, S., and Grübel, G. (2010). Single-pulse resonant magnetic scattering using a soft x-ray free-electron laser. *Phys. Rev. B*, 81(10):100401.

Hara, T., Togawa, K., and Tanaka, H. (2010). Beam optics and parameter design of the XFEL/SPRING-8. In *Proceedings of FEL2010, Malmö.*

Hartmann, J. (1900). *Bemerkungen über den Bau und die Justierung von Spektrographen.* Z. Instrumentenkd.

Hass, E., Ackermann, S., Boedewadt, J., and Rossbach, J. (2011). Transverse overlap diagnostics with wire scanners in the XUV-seeding experiment at FLASH. In *Proceedings of FEL2011, Shanghai.*

He, X., Miranda, M., Schwenke, J., Guilbaud, O., Ruchon, T., Heyl, C., Georgadiou, E., Rakowski, R., Persson, A., Gaarde, M. B., and L'Huillier, A. (2009). Spatial and spectral properties of the high-order harmonic emission in argon for seeding applications. *Physical Review A (Atomic, Molecular, and Optical Physics)*, 79(6):063829.

Hecht, E. and Zajac, A. (1997). *Optics.* Addison Wesley Publishing Company.

Hentschel, M., Klenberger, R., Spielmann, C., Reider, G., Milosevic, N., Brabec, T., Corkum, P., Heinzmann, U., Drescher, M., and Krausz, F. (2001). Attosecond metrology. *Nature*, 414:509–513.

Hergott, J.-F., Kovacev, M., Merdji, H., Hubert, C., Mairesse, Y., Jean, E., Breger, P., Agostini, P., Carré, B., and Salières, P. (2002). Extreme-ultraviolet high-order harmonic pulses in the microjoule range. *Phys. Rev. A*, 66(2):021801.

Hipp, U. (2010). Investigations on the wavefront of the seed laser at the xuv seeding experiment at FLASH. diploma thesis, University of Hamburg.

Hofmann, A. (2004). *The Physics of Synchrotron Radiation.* Cambridge University Press.

Honkavaara, K., Brenger, A., Fischer, R., Nolle, D., Rehlich, K., Cacciotti, L., Castellano, M., DiPirro, G., Raparelli, M., Sorchetti, R., Catani, L., and Cianchi, A. (2003). Design of OTR beam profile monitors for the TESLA test facility, phase 2n (TTF2). In *Proceedings of PAC'03, Portland.*

Huang, Z. and Kim, K.-J. (2007). Review of x-ray free-electron laser theory. *Physical Review special topics - accelerators and beams*, 10:034801.

Huillier, Schafer, and Kulander (1991). Theoretical aspects of intense field harmonic generation. *J.Phys B: At. Mol. Opt. Phys*, 24:3315–3341.

Ishikawa, K. L., Takahashi, E. J., and Midorikawa, K. (2009). Wavelength dependence of high-order harmonic generation with independently controlled ionization and ponderomotive energy. *Phys. Rev. A*, 80(1):011807.

Jackson, J. D. (1999). *Classical Electrodynamics.* John Wiley & Sons, Inc.

Jaeglé, P. (2006). *Coherent Sources of XUV Radiation.* Springer Science+Business Media Inc.

Jousten, K. (2006). *Wutz: Handbuch Vakuumtechnik.* Friedr. Vieweg & Sohn Verlag.

Kan, C., Capjack, C. E., Rankin, R., and Burnett, N. H. (1995). Spectral and temporal structure in high harmonic emission from ionizing atomic gases. *Phys. Rev. A*, 52(6):R4336–R4339.

Kane, D. J. and Trebino, R. (1993a). Characterization of arbitrary femtosecond pulses using frequency-resolved optical gating. *IEEE Journal of Quantum Electronics*, 29:571–579.

Kane, D. J. and Trebino, R. (1993b). Single-shot measurement of the intensity and phase of an arbitrary ultrashort pulse by using frequency-resolved optical gating. *Opt. Lett.*, 18:823–825.

Kasparian, J. and Wolf, J.-P. (2008). Physics and applications of atmospheric nonlinear optics and filamentation. *Optics Express*, 16:466–493.

Kazamias, S., D.Douillet, Valentin, C., Lefrou, T., Grillon, G., Mullot, G., Augé, F., Mercère, P., Zeitoun, P., and Balcou, P. (2003a). Optimization of the focused flux of high harmonics. *Eur.Phys.J.D*, 26:47–50.

Kazamias, S., Douillet, D., Weihe, F., Valentin, C., Rousse, A., Sebban, S., Grillon, G., Augé, F., Hulin, D., and Balcou, P. (2003b). Global optimization of high harmonic generation. *Phys. Rev. Lett.*, 90(19):193901.

Keldysh, L. (1665). Ionization in the field of a strong electromagnetic wave. *Sov. Phys. JETP*, 20:1307–.

Khan, S., Bödewadt, J., Winter, A., Angelova, G., Ziemann, V., Salen, P., van der Meulen, P., Hamberg, M., Larsson, M., Schlarb, H., Löhl, F., Saldin, E., Schneidmiller, E., and Yurkov, M. (2008). Results from the optical replica experiments at FLASH. In *Proceedings FEL'08, Gyeongju.*

Kienberger, R., Hentschel, M., Uiberacker, M., Spielmann, C., Kitzler, M., Scrinzi, A., Wieland, M., Westerwalbesloh, T., Kleineberg, U., Heinzmann, U., Drescher, M., and Krausz, F. (2002). Steering attosecond electron wave packets with light. *Science*, 297(5584):1144–1148.

Kim, H. T., Kim, I. J., Lee, D. G., Hong, K.-H., Lee, Y. S., Tosa, V., and Nam, C. H. (2004). Optimization of high-order harmonic brightness in the space and time domains. *Phys. Rev. A*, 69(3):031805.

Kim, I. J., Kim, C. M., Kim, H. T., Lee, G. H., Lee, Y. S., Park, J. Y., Cho, D. J., and Nam, C. H. (2005). Highly efficient high-harmonic generation in an orthogonally polarized two-color laser field. *Physical Review Letters*, 94(24):243901.

Kondratenko, A. and Saldin, E. (1980). Generation of coherent radiation by a relativistic electron beam in an ondulator. *Part.Acc.*, 10(207):207–216.

Koprek, W., Behrens, C., Bock, M., Felber, M., Gessler, P., Hacker, K., Schlarb, H., Schmidt, C., Steffen, B., Wesch, S., Schulz, S., and Szewinski, J. (2010). Intra-train longitudinal feedback for beam stabilization at FLASH. In *Proceedings of FEL2010, Malmö, Sweden.*

Krause, J. L., Schafer, K. J., and Kulander, K. C. (1992). High-order harmonic generation from atoms and ions in the high intensity regime. *Phys. Rev. Lett.*, 68(24):3535–3538.

Krikunova, M., Maltezopoulos, T., Azima, A., Schlie, M., Frühling, U., Redlin, H., Kalms, R., Cunovic, S., Kabachnik, N. M., Wieland, M., and Drescher, M. (2009). Time-resolved ion spectrometry on xenon with the jitter-compensated soft x-ray pulses of a free-electron laser. *New Journal of Physics*, 11(12):123019.

Krikunova, M., Maltezopoulos, T., Wessels, P., Schlie, M., Azima, A., Wieland, M., and Drescher, M. (2011). Ultrafast photofragmentation dynamics of molecular iodine driven with timed xuv and near-infrared light pulses. *J. Chem. Phys.*, 134:024313.

Kroupa, V. F. (2003). *Phase Lock Loops and Frequency Synthesis.* John Wiley & Sons Inc.

Kulander, K. and Rescigno, T. (1991). Effective potentials for time-dependent calculations of multiphoton processes in atoms. *Comp. Phys. Comm*, 63:523.

Kulander, K. C., Schafer, K. J., and Krause, J. L. (1993). NATO Advanced Studies Institute No 316 Series B: Physics, (Plenum, New York). *Super-Intense Laser-Atom Physics.*

Lambert, G., Gautier, J., Hauri, C. P., Zeitoun, P., Valentin, C., Marchenko, T., Tissandier, F., Goddet, J. P., Ribiere, M., Rey, G., Fajardo, M., and Sebban, S. (2009). An optimized khz two-colour high harmonic source for seeding free-electron lasers and plasma-based soft x-ray lasers. *New Journal of Physics*, 11(8):083033 (17pp).

Lambert, G., Hara, T., Garzella, D., Tanikawa, T., Labat, M., Carre, B., Kitamura, H., Shintake, T., Bougeard, M., Inoue, S., Tanaka, Y., Salieres, P., Merdji, H., Chubar, O., Gobert, O., Tahara, K., and Couprie, M.-E. (2008). Injection of harmonics generated in gas in a free-electron laser providing intense and coherent extreme-ultraviolet light. *Nature Phys. 4*, pages 296–300.

Lan, P., Takahashi, E. J., and Midorikawa, K. (2010). Wavelength scaling of efficient high-order harmonic generation by two-color infrared laser fields. *Phys. Rev. A*, 81(6):061802.

Lawrence Berkeley National Laboratory (2011). X-ray transmission of a solid. `http://www.cxro.lbl.gov/`.

L.Bergmann, C.Schaefer, and H.Niedrig (2004). *Optik*. de Gruyter.

L'Huillier, A., Balcou, P., Candel, S., Schafer, K. J., and Kulander, K. C. (1992). Calculations of high-order harmonic-generation processes in xenon at 1064 nm. *Phys. Rev. A*, 46(5):2778–2790.

L'Huillier, A., Lewenstein, M., Salières, P., Balcou, P., Ivanov, M. Y., Larsson, J., and Wahlström, C. G. (1993). High-order harmonic-generation cutoff. *Phys. Rev. A*, 48(5):R3433–R3436.

LCLS (2011). `https://slacportal.slac.stanford.edu/`.

Lewenstein, M., Balcou, P., Ivanov, M. Y., L'Huillier, A., and Corkum, P. B. (1994). Theory of high-harmonic generation by low-frequency laser fields. *Phys. Rev. A*, 49(3):2117–2132.

Lewenstein, M., Salières, P., and L'Huillier, A. (1995). Phase of the atomic polarization in high-order harmonic generation. *Phys. Rev. A*, 52(6):4747–4754.

Lin, S. (2006). *Advances in Multi-photon processes and spectroscopy vol. 17*. World Scientific Publishing Company.

Liu, P., Zeng, Z., Li, Y., Zhao, S., Li, X., Li, R., and Xu, Z. (2009). Quantum path selection and control in high-order harmonic generation using a spatially shaped laser beam. *Physical Review A (Atomic, Molecular, and Optical Physics)*, 79(6):063823.

Löhl, F. (2009). *Optical Synchronization of a Free-Electron Laser with Femtosecond Precision*. PhD thesis, University of Hamburg.

Lowdermilk, W. H. and Murray, J. E. (1980). The multipass amplifier: Theory and numerical analysis. *Journal of Applied Physics*, 51(5):2436–2444.

Luo, X. and Wang, Y. (2010). Power content M^2-values smaller than one. *Appl Phys B*, 98:181–185.

Madey, J. (1971). Stimulated emission of bremsstrahlung in a periodic magnetic field. *J.Appl.Phys.*, 42(5):1906–1913.

Maiman, T. (1960). Stimulated optical radiation in ruby. *Nature*, 187:493–494.

Mainfray, G. and Manus, G. (1991). Multiphoton ionization of atoms. *Reports on Progress in Physics*, 54(10):1333.

Maltezopoulos, T., Cunovic, S., Wieland, M., Beye, M., Azima, A., Redlin, H., Krikunova, M., Kalms, R., Frühling, U., Budzyn, F., Wurth, W., Föhlisch, A., and Drescher, M. (2008). Single-shot timing measurement of extreme-ultraviolet free-electron laser pulses. *New Journal of Physics*, 10(3):033026.

Mancuso, A. P., Gorniak, T., Staier, F., Yefanov, O. M., Barth, R., Christophis, C., Reime, B., Gulden, J., Singer, A., Pettit, M. E., Nisius, T., Wilhein, T., Gutt, C., Grübel, G., Guerassimova, N., Treusch, R., Feldhaus, J., Eisebitt, S., Weckert, E., Grunze, M., Rosenhahn, A., and Vartanyants, I. A. (2010). Coherent imaging of biological samples with femtosecond pulses at the free-electron laser flash. *New Journal of Physics*, 12(3):035003.

Marchesini, S., Boutet, S., Sakdinawat, A. E., Bogan, M. J., Bajt, S., Barty, A., Chapman, H. N., Frank, M., Hau-Riege, S. P., Szoke, A., Cui, C., Shapiro, D. A., Howells, M. R., Spence, J. C. H., Shaevitz, J. W., Lee, J. Y., Hajdu, J., and Seibert, M. M. (2008). Massively parallel x-ray holography. *Nat. Photon*, 2:560–563.

Mauritsson, J., Johnsson, P., Gustafsson, E., L'Huillier, A., Schafer, K. J., and Gaarde, M. B. (2006). Attosecond pulse trains generated using two color laser fields. *Phys. Rev. Lett.*, 97(1):013001.

Mauritsson, J., Johnsson, P., López-Martens, R., Varjú, K., Kornelis, W., Biegert, J., Keller, U., Gaarde, M. B., Schafer, K. J., and L'Huillier, A. (2004). Measurement and control of the frequency chirp rate of high-order harmonic pulses. *Phys. Rev. A*, 70(2):021801.

McNeil, B. W. J., Clarke, J. A., Dunning, D. J., Hirst, G. J., Owen, H. L., Thompson, N. R., Sheehy, B., and Williams, P. H. (2007a). An xuv-fel amplifier seeded using high harmonic generation. *New Journal of Physics*, 9(82):1–31.

McNeil, B. W. J., Thompson, N. R., Dunning, D. J., Karssenberg, J. G., van der Slot, P. J. M., and Boller, K.-J. (2007b). A design for the generation of temporally-coherent radiation pulses in the vuv and beyond by a self-seeding high-gain free electron laser amplifier. *New Journal of Physics*, 9(7):239.

McPherson, A., Gibson, G., Jara, H., Johann, U., Luk, T. S., I. A. McIntyre, K. B., and Rhodes, C. K. (1987). Studies of multiphoton production of vacuum-ultraviolet radiation in the rare gases. *J.Opt.Soc.Am.B*, 4(4):595–601.

Menzel, R. (2001). *Photonics*. Springer-Verlag.

M.Ferray, A.L'Huillier, X.F.Li, L.A.Lompre, G.Mainfray, and C.Manus (1988). Multiple-harmonic conversion of 1064 nm radiation in rare gases. *J.Phys.B*, 21:L31–L35.

Milošević, D. B. and Becker, W. (2002). Role of long quantum orbits in high-order harmonic generation. *Phys. Rev. A*, 66(6):063417.

Miltchev, V. (2011). private communications.

Miltchev, V., Azima, A., Bödewadt, J., Curbis, F., Delsim-Hashemi, H., Drescher, M., , Maltezopoulos, T., Mittenzwey, M., Rossbach, J., Tarkeshian, R., Wieland, M., Düsterer, S., Feldhaus, J., Laarmann, T., Schlarb, H., Khan, S., Meseck, A., and Ischebeck, R. (2009). Technical design of the xuv seeding experiment at FLASH. In *31st International Free Electron Laser Conference BT Convention Centre, Liverpool, UK*.

Miltchev, V., Azima, A., Bödewadt, J., Curbis, F., Delsim-Hashemi, H., Drescher, M., Maltezopoulos, T., Mittenzwey, M., Rossbach, J., Tarkeshian, R., Wieland, M., Bajt, S., Düsterer, S., Feldhaus, J., Laarmann, T., Schlarb, H., Meseck, A., Khan, S., and Ischebeck, R. (2008). Tolerance studies on the high harmonic laser seeding at FLASH, TUPH003. In *Proceedings FEL-2008, Gyeongju, Korea*.

Mitzner, R., Siemer, B., Neeb, M., Noll, T., Siewert, F., Roling, S., Rutkowski, M., Sorokin, A. A., Richter, M., Juranic, P., Tiedtke, K., Feldhaus, J., Eberhardt, W., and Zacharias, H. (2008). Spatio-temporal coherence of free electron laser pulses in the soft x-ray regime. *Opt. Express*, 16(24):19909–19919.

Mitzner, R., Sorokin, A. A., Siemer, B., Roling, S., Rutkowski, M., Zacharias, H., Neeb, M., Noll, T., Siewert, F., Eberhardt, W., Richter, M., Juranic, P., Tiedtke, K., and Feldhaus, J. (2009). Direct autocorrelation of soft-x-ray free-electron-laser pulses by time-resolved two-photon double ionization of He. *Phys. Rev. A*, 80(2):025402.

Miyazaki, K. and Takada, H. (1995). High-order harmonic generation in the tunneling regime. *Phys. Rev. A*, 52(4):3007–3021.

Murray, J. E. and Lowdermilk, W. H. (1980). Nd : Yag regenerative amplifier. *Journal of Applied Physics*, 51(7):3548–3556.

New, G. H. C. and Ward, J. F. (1967). Optical third-harmonic generation in gases. *Phys. Rev. Lett.*, 19(10):556–559.

Nguyen, D. N., Emmert, L. A., Schwoebel, P., Patel, D., Menoni, C. S., Shinn, M., and Rudolph, W. (2011). Femtosecond pulse damage thresholds of dielectric coatings in vacuum. *Opt. Express*, 19(6):5690–5697.

Norin, J., Mauritsson, J., Johansson, A., Raarup, M. K., Buil, S., Persson, A., Dühr, O., Gaarde, M. B., Schafer, K. J., Keller, U., Wahlström, C.-G., and L'Huillier, A. (2002). Time-frequency characterization of femtosecond extreme ultraviolet pulses. *Phys. Rev. Lett.*, 88(19):193901.

Palmer, C. and Loewen, E. (2005). *Diffraction grating handbook*. Newport Corporation.

Papadogiannis, N. A., Witzel, B., Kalpouzos, C., and Charalambidis, D. (1999). Observation of attosecond light localization in higher order harmonic generation. *Phys. Rev. Lett.*, 83(21):4289–4292.

Paschotta, R. (2008). *Encyclopedia of Laser Physics and Technology*. Wiley-VCH.

Patterson, B. D., Abela, R., Braun, H.-H., Flechsig, U., Ganter, R., Kim, Y., Kirk, E., Oppelt, A., Pedrozzi, M., Reiche, S., Rivkin, L., Schmidt, T., Schmitt, B., Strocov, V. N., Tsujino, S., and Wrulich, A. F. (2010). Coherent science at the swissfel x-ray laser. *New Journal of Physics*, 12(3):035012.

Paul, A., Bartels, R. A., R. Tobey, H. G., Weiman, S., I. P. Christov, M. M. Murnane, H. C. K., and Backus, S. (2003). Quasi-phase-matched generation of coherent extreme-ultraviolet light. *Nature*, 421:51–54.

Paul, P. M., Toma, E. S., Breger, P., Mullot, G., Auge, F., Balcou, P., Muller, H. G., and Agostini, P. (2001). Observation of a Train of Attosecond Pulses from High Harmonic Generation. *Science*, 292(5522):1689–1692.

Physikalisch-Technische Bundesanstalt (2011). `http://www.ptb.de/`.

Pirri, A., Corsi, C., and Bellini, M. (2008). Enhancing the yield of high-order harmonics with an array of gas jets. *Phys. Rev. A*, 78(1):011801.

Popruzhenko, S. V., Zaretsky, D. F., and Becker, W. (2010). High-order harmonic generation by an intense infrared laser pulse in the presence of a weak uv pulse. *Phys. Rev. A*, 81(6):063417.

Powell, F. R., Vedder, P. W., Lindblom, J. F., and Powell, S. F. (1990). Thin film filter performance for extreme ultraviolet and x-ray applications. *Opt. Eng.*, 29.

Radcliffe, P., Düsterer, S., Azima, A., Redlin, H., Feldhaus, J., Dardis, J., Kavanagh, K., Luna, H., Gutierrez, J. P., Yeates, P., Kennedy, E. T., Costello, J. T., Delserieys, A., Lewis, C. L. S., Taïeb, R., Maquet, A., Cubaynes, D., and Meyer, M. (2007). Single-shot characterization of independent femtosecond extreme ultraviolet free electron and infrared laser pulses. *Applied Physics Letters*, 90(13):131108.

Rae, S. C. and Burnett, K. (1993a). Calculations of high-order-harmonic generation in the strongly ionizing regime. *Phys. Rev. A*, 48(3):2490–2493.

Rae, S. C. and Burnett, K. (1993b). Harmonic generation and phase matching in the tunnelling limit. *Journal of Physics B: Atomic, Molecular and Optical Physics*, 26(8):1509.

Rae, S. C., Burnett, K., and Cooper, J. (1994). Generation and propagation of high-order harmonics in a rapidly ionizing medium. *Phys. Rev. A*, 50(4):3438–3446.

Ravasio, A., Gauthier, D., Maia, F. R. N. C., Billon, M., Caumes, J.-P., Garzella, D., Géléoc, M., Gobert, O., Hergott, J.-F., Pena, A.-M., Perez, H., Carré, B., Bourhis, E., Gierak, J., Madouri, A., Mailly, D., Schiedt, B., Fajardo, M., Gautier, J., Zeitoun, P., Bucksbaum, P. H., Hajdu, J., and Merdji, H. (2009). Single-shot diffractive imaging with a table-top femtosecond soft x-ray laser-harmonics source. *Physical Review Letters*, 103(2):028104.

Rehders, M. (2011). Hochstabilisierter fs-Pulstransport für zwei-farben Pump-Probe Experimente am geseedeten Freie Elektronen Laser FLASH. diploma thesis, University of Hamburg.

Reiche, S. (1999). Genisis 1.3: a fully 3D time-dependent FEL simulation code. *Nuclear Instruments and Methods in Physics Research A*, 429:243 – 248.

Reng, N. and B.Eppich (1992). Definition and measurements of high-power laser beam parameters. *Optical and Quantum Electronics*, 24:S973–S992.

Robinson, I., Gruebel, G., and Mochrie, S. (2010). X-ray beams with high coherence. *New J. Phys.*, 12:035002–035008.

Rosenhahn, A., Staier, F., Nisius, T., Schäfer, D., Barth, R., Christophis, C., Stadler, L.-M., Streit-Nierobisch, S., Gutt, C., Mancuso, A., Schropp, A., Gulden, J., Reime, B., Feldhaus, J., Weckert, E., Pfau, B., Günther, C. M., Könnecke, R., Eisebitt, S., Martins, M., Faatz, B., Guerassimova, N., Honkavaara, K., Treusch, R., Saldin, E., Schreiber, S., Schneidmiller, E. A., Yurkov, M. V., Vartanyants, I., Grübel, G., Grunze, M., and Wilhein, T. (2009). Digital in-line holography with femtosecond VUV radiation provided by the free-electron laser FLASH. *Opt. Express*, 17(10):8220–8228.

Rulliere, C. (1998). *Femtosecond Laser Pulses*. Springer.

Saldin, E., Schneidmiller, E., and Yurkov, M. (1998). Statistical properties of radiation from vuv and x-ray free electron laser. *Optics Communications*, 148(4-6):383 – 403.

Saldin, E., Schneidmiller, E., and Yurkov, M. (1999a). FAST: a three-dimensional time-dependent FEL simulation code. *Nuclear Instruments and Methods in Physics Research A*, 429:233 – 237.

Saldin, E., Schneidmiller, E., and Yurkov, M. (1999b). *The Physics of Free Electron Lasers*. Berlin: Springer.

Saldin, E., Schneidmiller, E., and Yurkov, M. (2008a). Coherence properties of the radiation from x-ray free-electron laser. *Opt. Commun.*, 281:1179–1188.

Saldin, E., Schneidmiller, E., and Yurkov, M. (2008b). Output power and degree of transverse coherence of x-ray free electron lasers. *Opt. Commun.*, 281:4727–4734.

Saldin, E., Schneidmiller, E., and Yurkov, M. (2010). Statistical and coherence properties of radiation from x-ray free-electron lasers. *New J. Phys.*, 12:03510–.

Saleh, B. E. A. and Teich, M. C. (1991). *Fundamentals of Photonics*. John Wiley & Sons, Inc.

Salières, P., Antoine, P., de Bohan, A., and Lewenstein, M. (1998). Temporal and spectral tailoring of high-order harmonics. *Phys. Rev. Lett.*, 81(25):5544–5547.

Salieres, P., Carre, B., Le Deroff, L., Grasbon, F., Paulus, G. G., Walther, H., Kopold, R., Becker, W., Milosevic, D. B., Sanpera, A., and Lewenstein, M. (2001). Feynman's Path-Integral Approach for Intense-Laser-Atom Interactions. *Science*, 292(5518):902–905.

Salières, P., L'Huillier, A., and Lewenstein, M. (1995). Coherence control of high-order harmonics. *Phys. Rev. Lett.*, 74(19):3776–3779.

Sandberg, R. L., Paul, A., Raymondson, D. A., Hadrich, S., Gaudiosi, D. M., Holtsnider, J., Tobey, R. I., Cohen, O., Murnane, M. M., Kapteyn, H., Song, C., Miao, J., Liu, Y., and Salmassi, F. (2007). Lensless diffractive imaging using tabletop coherent high-harmonic soft-x-ray beams. *Phys. Rev. Lett.*, 99. JILA Pub. 8029.

Schlotter, W., Sorgenfrei, F., Beeck, T., Beye, M., Gieschen, S., Meyer, H., Nagasono, M., Föhlisch, A., and Wurth, W. (2010). Longitudinal coherence measurements of an extreme-ultraviolet free-electron laser. *Opt. Lett.*, 35:372–.

Schmüser, P., Dohlus, M., and Rossbach, J. (2008). *Ultraviolet and Soft X-Ray Free-Elektron Lasers*. Springer-Verlag Berlin Heidelberg.

Schneider, J. R. (2010). FLASH - from accelerator test facility to the first single-pass soft x-ray free-electron laser. *J.Phys.B: At.Mol.Opt.Phys.*, 43:194001–.

Schneidmiller, E. and Yurkov, M. (2010). Expected properties of the radiation from the european XFEL operating at the energy of 14 GeV. In *Proceedings of FEL2010, Malmö*.

Schreiber, S. (2010). Soft and hard x-ray SASE free electron lasers. *Reviews of Accelerator Science and Technology*, 3:93–120.

Schreiber, S. (2011a). Machine advisory committee.

Schreiber, S. (2011b). private communications.

Schreiber, S., Faatz, B., Feldhaus, J., Honkavaara, K., Treusch, R., and Vogt, M. (2011). Status of the FEL user facility FLASH. In *Proceedings of FEL2011, Shanghai.*

Schreiber, S., Faatz, B., Feldhaus, J., Honkavaara, K., Treusch, R., Vogt, M., and Rossbach, J. (2010). FLASH upgrade and first results. In *Proceedings of FEL2010, Malmö, Sweden.*

Schroedter, L. (2009). Design, simulation and operation of two spectrometers for the analysis of high harmonic and fluorescence radiation in the extreme ultraviolet spectral range. diploma thesis, University of Hamburg.

Schulz, M. (2010). Charakterisierung und Optimierung ultrakurzer Laserpulse für das Seeden von FLASH. diploma thesis, University of Hamburg.

Schulz, S. (2011). *to be published.* PhD thesis, University of Hamburg.

Schulz, S., Schmüser, P., Zemella, J., Arsov, V., Felber, M., Löhl, F., Lorbeer, B., Ludwig, F., Matthiesen, K.-H., Schlarb, H., Schmidt, B., Winter, A., and Steffen, B. (2008). An optical cross-correlation scheme to synchronize distributed laser systems at FLASH. In *Proceedings of EPAC 2008, Genua, Italy.*

Schulze, D., Dörr, M., Sommerer, G., Ludwig, J., Nickles, P. V., Schlegel, T., Sandner, W., Drescher, M., Kleineberg, U., and Heinzmann, U. (1998). Polarization of the 61st harmonic from 1053-nm laser radiation in neon. *Phys. Rev. A*, 57(4):3003–3007.

Seres, J., Yakovlev, V., Seres, E., Streli, C., Wobrauschek, P., Spielmann, C., and Krausz, F. (2007). Coherent superposition of laser-driven soft-x-ray harmonics from successive sources. *Nature*, 3:878–883.

Shack, R. V. and Platt, B. C. (1971). Abstract. production and use of a lenticular hartmann screen. *J. Opt. Soc. Am.*, 61:656–660.

Shaftan, T., Doyuran, A., Johnson, E., Krinsky, S., Loos, H., Murphy, J., Rakowsky, G., Rose, J., Sheehy, B., Skaritka, J., Wang, X., Wu, Z., and Yu, L. (2004). Seeded harmonic generation schemes. In *Proceedings of APAC.*

Shen, Y. (1984). *The Principles of Nonlinear Optics.* John Wiley & Sons, Toronto, Canada.

Shintake, T. (2010). XFEL/SPRING-8 constuction and SCSS operation status. In *Proceedings of FEL2010, Malmö.*

Siegman, A. (1993). Defining, measuring, and optimizing laser beam quality. In *Proc. SPIE 1868.*

Siegman, A. E. (1986). *Lasers.* University Science Books, Sausalito.

Spielmann, C., Curley, P. F., Brabec, T., and Krausz, F. (1994). Ultrabroadband femtosecond lasers. *QE*, 30:1100–.

Stephan, F., Boulware, C. H., Krasilnikov, M., Bähr, J., Asova, G., Donat, A., Gensch, U., Grabosch, H. J., Hänel, M., Hakobyan, L., Henschel, H., Ivanisenko, Y., Jachmann, L., Khodyachykh, S., Khojoyan, M., Köhler, W., Korepanov, S., Koss, G., Kretzschmann, A., Leich, H., Lüdecke, H., Meissner, A., Oppelt, A., Petrosyan, B., Pohl, M., Riemann, S., Rimjaem, S., Sachwitz, M., Schöneich, B., Scholz, T., Schulze, H., Schultze, J., Schwendicke, U., Shapovalov, A., Spesyvtsev, R., Staykov, L., Tonisch, F., Walter, T., Weisse, S., Wenndorff, R., Winde, M., Vu, L. v., Dürr, H., Kamps, T., Richter, D., Sperling, M., Ovsyannikov, R., Vollmer, A., Knobloch, J., Jaeschke, E., Boster, J., Brinkmann, R., Choroba, S., Flechsenhar, K., Flöttmann, K., Gerdau, W., Katalev, V., Koprek, W., Lederer, S., Martens, C., Pucyk, P., Schreiber, S., Simrock, S., Vogel, E., Vogel, V., Rosbach, K., Bonev, I., Tsakov, I., Michelato, P., Monaco, L., Pagani, C., Sertore, D., Garvey, T., Will, I., Templin, I., Sandner, W., Ackermann, W., Arévalo, E., Gjonaj, E., Müller, W. F. O., Schnepp, S., Weiland, T., Wolfheimer, F., Rönsch, J., and Rossbach, J. (2010). Detailed characterization of electron sources yielding first demonstration of european x-ray free-electron laser beam quality. *Phys. Rev. ST Accel. Beams*, 13(2):020704.

Strickland, D. and Mourou, G. (1985). Compression of amplified chirped optical pulses. *Optics Communications*, 56:219–221.

Strohmeiner, B. (1990). An ESCA method for determining the oxide thickness on aluminum alloys. *Surface and Interface analysis*, 15:51–56.

Stupakov, G. (2010). Echo-enabled harmonic generation. In *Proceedings of IPAC'10, Kyoto, Japan.*

Svelto, O. (1982). *Principles of Lasers.* Plenum Press, New York and London.

Tamaki, Y., Itatani, J., Obara, M., and Midorikawa, K. (2000). Optimization of conversion efficiency and spatial quality of high-order harmonic generation. *Phys. Rev. A*, 62(6):063802.

Tarkeshian, R. (2011). *to be published.* PhD thesis, University of Hamburg.

Tarkeshian, R., Azima, A., Bödewadt, J., Curbis, F., Delsim-Hashemi, H., Drescher, M., Maltezopoulos, T., Miltchev, V., Mittenzwey, M., Rönsch-Schulenburg, J., Rossbach, J., Wieland, M., Honkavaara, K., Laarmann, T., Schlarb, H., Schreiber, S., and Ischebeck, R. (2010). Femtosecond resolved determination of electron beam and xuv seed pulse temporal overlap in sFLASH. In *Proceedings PAC'11, New York.*

Taylor, J. R. (1939). *An Introduction To Error Analysis - the study of uncertainties in physical measurements.* University Science Books.

Tcherbakoff, O., Labat, M., Lambert, G., Garzella, D., Bougeard, M., Breger, P., Monchicourt, P., Merdji, H., Salieres, P., Carre, B., Couprie, M., Doria, A., and Gianessi, L. (2006). Seeding SPARC facility with harmonic generation in gases: preliminary tests of the harmonic generation in gas chamber. In *Proc. of EPAC 2006, Edinburgh.*

Thorin, S., Brandin, M., Werin, S., Goldammer, K., and Bahrdt, J. (2007). Start-to-end simulations for a seeded harmonic generation free electron laser. *Phys. Rev. ST Accel. Beams*, 10(11):110701.

Tiedtke, K., Azima, A., von Bargen, N., Bittner, L., Bonfigt, S., Düsterer, S., Faatz, B., Frühling, U., Gensch, M., Gerth, C., Guerassimova, N., Hahn, U., Hans, T., Hesse, M., Honkavaar, K., Jastrow, U., Juranic, P., Kapitzki, S., Keitel, B., Kracht, T., Kuhlmann, M., Li, W. B., Martins, M., Nunez, T., Plönjes, E., Redlin, H., Saldin, E. L., Schneidmiller, E. A., Schneider, J. R., Schreiber, S., Stojanovic, N., Tavella, F., Toleikis, S., Treusch, R., Weigelt, H., Wellhöfer, M., Wabnitz, H., Yurkov, M. V., and Feldhaus, J. (2009). The soft x-ray free-electron laser FLASH at DESY: beamlines, diagnostics and end-stations. *New Journal of Physics*, 11(2):023029.

Tischer, M., Englisch, U., Muller, T., Schops, A., Vagin, P., Delsim-Hashemi, H., Rossbach, J., and Vasserman, I. (2010). Undulators of the sFLASH experiment. In *Proceedings IPAC'10, Kyoto, 3114.*

Togashi, T., Takahashi, E. J., Midorikawa, K., Aoyama, M., Yamakawa, K., Sato, T., Iwasaki, A., Owada, S., Okino, T., Yamanouchi, K., Kannari, F., Yagishita, A., Nakano, H., Couprie, M. E., Fukami, K., Hatsui, T., Hara, T., Kameshima, T., Kitamura, H., Kumagai, N., Matsubara, S., Nagasono, M., Ohashi, H., Ohshima, T., Otake, Y., Shintake, T., Tamasaku, K., Tanaka, H., Tanaka, T., Togawa, K., Tomizawa, H., Watanabe, T., Yabashi, M., and Ishikawa, T. (2011). Extreme ultraviolet free electron laser seeded with high-order harmonic of ti:sapphire laser. *Opt. Express*, 19(1):317–324.

T.Pfeifer (2006). Femtosecond x-ray science. *Rep.Prog.Phys*, 69:443–505.

Trebino, R. and Kane, D. J. (1993). Using phase retrieval to measure the intensity and phase of ultrashort pulses: frequency-resolved optical gating. *J. Opt. Soc. Am. A*, 10:1101–1111.

Treusch, R. and Feldhaus, J. (2010). FLASH: new opportunities for (time-resolved) coherent imaging of nanostructures. *New J. Phys.*, 12:035015–.

Uphues, T., Schultze, M., Kling, M. F., Uiberacker, M., Hendel, S., Heinzmann, U., Kabachnik, N. M., and Drescher, M. (2008). Ion-charge-state chronoscopy of cascaded atomic auger decay. *New Journal of Physics*, 10(2):025009.

Uspenskii, Y., Levashov, V. E., Vinogradov, A. V., Fedorenko, A. I., Kondratenko, V. V., Pershin, Y., Zubarev, E. N., and Fedotov, V. Y. (1998). High-reflectivity multilayer mirrors for a vacuum-ultraviolet interval of 35-50nm. *Opt. Lett.*, 23(10):771–773.

Varjú, K., P.Johnsson, R.López-Martens, T.Remetter, Gustafsson, E., J.Mauritsson, M.B.Gaarde, K.J.Schafer, Ch.Erny, I.Sola, A.Zaïr, E.Constant, E.Cormier, E.Mével, and L'Huillier (2005). Experimental studies of attosecond pulse trains. *Laser Physics*, 15(6):888–898.

Čutić, N., Lindau, F., Thorin, S., Werin, S., Bahrdt, J., Eberhardt, W., Holldack, K., Erny, C., L'Huillier, A., and Mansten, E. (2011). Vacuum ultraviolet circularly polarized coherent femtosecond pulses from laser seeded relativistic electrons. *Phys. Rev. ST Accel. Beams*, 14(3):030706.

Čutić, N., Lindau, F., Thorin, S., Werin, S., Erny, C., L'Huillier, A., Mansten, E., Bahrdt, J., and Holldack, K. (2010). First results of coherent harmonic generation at the MAX-LAB TEST FEL. In *Proceedings of FEL 2010, Malmö, Sweden.*

Wahlström, C.-G., Larsson, J., Persson, A., Starczewski, T., Svanberg, S., Salières, P., Balcou, P., and L'Huillier, A. (1993). High-order harmonic generation in rare gases with an intense short-pulse laser. *Phys. Rev. A*, 48(6):4709–4720.

Wang, X., Shen, Y., Watanabe, T., Murphy, J., Rose, J., and Tsang, T. (2006). The first lasing of 193 nm sase, 4th harmonic HGHG and ESASE at the NSLS SDL. In *Proceedings of FEL 2006, BESSY, Berlin, Germany.*

Ward, J. F. and New, G. H. C. (1969). Optical third harmonic generation in gases by a focused laser beam. *Phys. Rev.*, 185(1):57–72.

W.F.Drake (2006). *Springer Handbook of Atomic, Molecular, and Optical Physics.* Springer-Verlag Berlin Heidelberg.

Wiedemann, H. (2007). *Particle accelerator physics.* Springer, Berlin.

Willner, A. (2011). *to be published.* PhD thesis, University of Hamburg.

Windt, D. (1998). IMD - software for modeling the optical properties of multilayer films. *Computer in physics*, 12:360.

Winterfeldt, C., Spielmann, C., and Gerber, G. (2008). Colloquium: Optimal control of high-harmonics generation. *Reviews of Modern Physics*, 80:117–140.

Xiang, D., Colby, E., Dunning, M., Gilevich, S., Hast, C., Jobe, K., McCormick, D., Nelson, J., Raubenheimer, T. O., Soong, K., Stupakov, G., Szalata, Z., Walz, D., Weathersby, S., Woodley, M., and Pernet, P.-L. (2010). Demonstration of the echo-enabled harmonic generation technique for short-wavelength seeded free electron lasers. *Phys. Rev. Lett.*, 105(11):114801.

Xu, H., Xiong, H., Zeng, Z., Fu, Y., Yao, J., Li, R., Cheng, Y., and Xu, Z. (2008). Fine interference fringes formed in high-order harmonic spectra generated by infrared driving laser pulses. *Phys. Rev. A*, 78(3):033841.

Yu, L.-H., Babzien, M., Ben-Zvi, I., DiMauro, L. F., Doyuran, A., Graves, W., Johnson, E., Krinsky, S., Malone, R., Pogorelsky, I., Skaritka, J., Rakowsky, G., Solomon, L., Wang, X. J., Woodle, M., Yakimenko, V., Biedron, S. G., Galayda, J. N., Gluskin, E., Jagger, J., Sajaev, V., and Vasserman, I. (2000). High-gain harmonic-generation free-elektron laser. *Science*, 289:932–934.

Yu, L. H., DiMauro, L., Doyuran, A., Graves, W. S., Johnson, E. D., Heese, R., Krinsky, S., Loos, H., Murphy, J. B., Rakowsky, G., Rose, J., Shaftan, T., Sheehy, B., Skaritka, J., Wang, X. J., and Wu, Z. (2003). First ultraviolet high-gain harmonic-generation free-electron laser. *Phys. Rev. Lett.*, 91(7):074801.

Yu, Q.-Z., Li, T.-T., Zhang, J., Zheng, J., Li, H.-M., Peng, X.-Y., and Li, K. (2004). Characterization of density profile of cylindrical pulsed gas jets. *Chin. Phys. Lett.*, 21:874–876.

Zaïr, A., Holler, M., Guandalini, A., Schapper, F., Biegert, J., Gallmann, L., Keller, U., Wyatt, A. S., Monmayrant, A., Walmsley, I. A., Cormier, E., Auguste, T., Caumes, J. P., and Salières, P. (2008). Quantum path interferences in high-order harmonic generation. *Phys. Rev. Lett.*, 100(14):143902.

ZEMAX LLC, R. (2011). `http://www.zemax.com`.

Zhang, X., Lytle, A. L., Popmintchev, T., Zhou, X., Kapteyn, H. C., Murnane, M. M., and Cohen, O. (2007). Quasi-phase-matching and quantum-path control of high-harmonic generation using counterpropagating light. *Nature*, 3:270–175.

Zhou, J., Peatross, J., Murnane, M. M., Kapteyn, H. C., and Christov, I. P. (1996). Enhanced high-harmonic generation using 25 fs laser pulses. *Phys. Rev. Lett.*, 76(5):752–755.

Acknowledgement

Zum Schluss möchte ich mich noch bei allen bedanken, die mir geholfen haben die Arbeit zu Ende zu bringen. Als erstes möchte ich mich bei Markus Drescher für die hervorragende Arbeitsatmosphäre, das spannende Thema und die Unterstützung bei vielen physikalischen Problemen bedanken. Theophilos Maltezopoulos gilt mein besonderer Dank für die tägliche Arbeit. Hier ist sind nicht nur die vielen Nachtschichten, Gespräche und die schweißtreibenden Arbeiten in "DER GRUBE" zu nennen, sondern insbesondere auch der Aufbau meiner eigenen Motivation. Jörg Roßbach danke ich für die professionelle Koordination des Projektes, aber auch der äußerst kritischen Beurteilung aller Arbeiten, durch die ich viel gelernt habe. Armin Azima und Marek Wieland gilt großer Dank für die unzähligen Gespräche. Insbesondere durch die außerordentlichen Fachkenntnisse in ihren jeweiligen Spezialgebieten konnte ich viel zielorientieter arbeiten. Velizar Miltchev danke ich für vertiefende Diskussionen im Bereich der FEL-Physik.

Viel Spaß hatte ich mit den Postdocs, Mitdoktoranden und Diplomanden. Bei den Technikern, Ingenieuren und den Werkstätten der Universität Hamburg und des DESY möchte ich vielmals bedanken. Namentlich hervorheben möchte ich Oliver Becker, der selbst Stunden nach Feierabend noch an der Werkbank stand, um mir kurzfristig Teile zu bearbeiten oder zu fertigen.

Mein herzlicher Dank gilt Benjamin Ehrhard für Tipps im Bereich der Modellierung, Booka M. Weser für hervorragende Tipps zum Zusammenschreiben und meinem engsten Freundeskreis für die exzellente *work-life-balance*.

Und schließlich und ganz besonders danke ich meiner Familie.